



UNIVERSIDAD DE CHILE
FACULTAD DE CIENCIAS FÍSICAS Y MATEMÁTICAS
DEPARTAMENTO DE FÍSICA

DYNAMICS OF PARTICLE-LIKE SOLUTIONS IN NON-LOCAL SYSTEMS

TESIS PARA OPTAR AL GRADO DE
MAGÍSTER EN CIENCIAS MENCIÓN FÍSICA

MARTIN LUKAS BATAILLE GONZALEZ

PROFESOR GUÍA:
MARCEL CLERC GAVILAN

MIEMBROS DE LA COMISIÓN:
MARCEL CLERC
KARIN ALFARO
OLEH OMEL'CHENKO
IGNACIO BORDEU
MUSTAPHA TLIDI

SANTIAGO DE CHILE
2024

Resumen

Lorem ipsum dolor sit amet, consectetuer adipiscing elit. Ut purus elit, vestibulum ut, placeat ac, adipiscing vitae, felis. Curabitur dictum gravida mauris. Nam arcu libero, nonummy eget, consectetuer id, vulputate a, magna. Donec vehicula augue eu neque. Pellentesque habitant morbi tristique senectus et netus et malesuada fames ac turpis egestas. Mauris ut leo. Cras viverra metus rhoncus sem. Nulla et lectus vestibulum urna fringilla ultrices. Phasellus eu tellus sit amet tortor gravida placerat. Integer sapien est, iaculis in, pretium quis, viverra ac, nunc. Praesent eget sem vel leo ultrices bibendum. Aenean faucibus. Morbi dolor nulla, malesuada eu, pulvinar at, mollis ac, nulla. Curabitur auctor semper nulla. Donec varius orci eget risus. Duis nibh mi, congue eu, accumsan eleifend, sagittis quis, diam. Duis eget orci sit amet orci dignissim rutrum.

Nam dui ligula, fringilla a, euismod sodales, sollicitudin vel, wisi. Morbi auctor lorem non justo. Nam lacus libero, pretium at, lobortis vitae, ultricies et, tellus. Donec aliquet, tortor sed accumsan bibendum, erat ligula aliquet magna, vitae ornare odio metus a mi. Morbi ac orci et nisl hendrerit mollis. Suspendisse ut massa. Cras nec ante. Pellentesque a nulla. Cum sociis natoque penatibus et magnis dis parturient montes, nascetur ridiculus mus. Aliquam tincidunt urna. Nulla ullamcorper vestibulum turpis. Pellentesque cursus luctus mauris.

Nulla malesuada porttitor diam. Donec felis erat, congue non, volutpat at, tincidunt tristique, libero. Vivamus viverra fermentum felis. Donec nonummy pellentesque ante. Phasellus adipiscing semper elit. Proin fermentum massa ac quam. Sed diam turpis, molestie vitae, placerat a, molestie nec, leo. Maecenas lacinia. Nam ipsum ligula, eleifend at, accumsan nec, suscipit a, ipsum. Morbi blandit ligula feugiat magna. Nunc eleifend consequat lorem. Sed lacinia nulla vitae enim. Pellentesque tincidunt purus vel magna. Integer non enim. Praesent euismod nunc eu purus. Donec bibendum quam in tellus. Nullam cursus pulvinar lectus. Donec et mi. Nam vulputate metus eu enim. Vestibulum pellentesque felis eu massa.

Quisque ullamcorper placerat ipsum. Cras nibh. Morbi vel justo vitae lacus tincidunt ultrices. Lorem ipsum dolor sit amet, consectetuer adipiscing elit. In hac habitasse platea dictumst. Integer tempus convallis augue. Etiam facilisis. Nunc elementum fermentum wisi. Aenean placerat. Ut imperdiet, enim sed gravida sollicitudin, felis odio placerat quam, ac pulvinar elit purus eget enim. Nunc vitae tortor. Proin tempus nibh sit amet nisl. Vivamus quis tortor vitae risus porta vehicula.

Abstract

Lorem ipsum dolor sit amet, consectetuer adipiscing elit. Ut purus elit, vestibulum ut, placerat ac, adipiscing vitae, felis. Curabitur dictum gravida mauris. Nam arcu libero, nonummy eget, consectetuer id, vulputate a, magna. Donec vehicula augue eu neque. Pellentesque habitant morbi tristique senectus et netus et malesuada fames ac turpis egestas. Mauris ut leo. Cras viverra metus rhoncus sem. Nulla et lectus vestibulum urna fringilla ultrices. Phasellus eu tellus sit amet tortor gravida placerat. Integer sapien est, iaculis in, pretium quis, viverra ac, nunc. Praesent eget sem vel leo ultrices bibendum. Aenean faucibus. Morbi dolor nulla, malesuada eu, pulvinar at, mollis ac, nulla. Curabitur auctor semper nulla. Donec varius orci eget risus. Duis nibh mi, congue eu, accumsan eleifend, sagittis quis, diam. Duis eget orci sit amet orci dignissim rutrum.

Nam dui ligula, fringilla a, euismod sodales, sollicitudin vel, wisi. Morbi auctor lorem non justo. Nam lacus libero, pretium at, lobortis vitae, ultricies et, tellus. Donec aliquet, tortor sed accumsan bibendum, erat ligula aliquet magna, vitae ornare odio metus a mi. Morbi ac orci et nisl hendrerit mollis. Suspendisse ut massa. Cras nec ante. Pellentesque a nulla. Cum sociis natoque penatibus et magnis dis parturient montes, nascetur ridiculus mus. Aliquam tincidunt urna. Nulla ullamcorper vestibulum turpis. Pellentesque cursus luctus mauris.

Nulla malesuada porttitor diam. Donec felis erat, congue non, volutpat at, tincidunt tristique, libero. Vivamus viverra fermentum felis. Donec nonummy pellentesque ante. Phasellus adipiscing semper elit. Proin fermentum massa ac quam. Sed diam turpis, molestie vitae, placerat a, molestie nec, leo. Maecenas lacinia. Nam ipsum ligula, eleifend at, accumsan nec, suscipit a, ipsum. Morbi blandit ligula feugiat magna. Nunc eleifend consequat lorem. Sed lacinia nulla vitae enim. Pellentesque tincidunt purus vel magna. Integer non enim. Praesent euismod nunc eu purus. Donec bibendum quam in tellus. Nullam cursus pulvinar lectus. Donec et mi. Nam vulputate metus eu enim. Vestibulum pellentesque felis eu massa.

Quisque ullamcorper placerat ipsum. Cras nibh. Morbi vel justo vitae lacus tincidunt ultrices. Lorem ipsum dolor sit amet, consectetuer adipiscing elit. In hac habitasse platea dictumst. Integer tempus convallis augue. Etiam facilisis. Nunc elementum fermentum wisi. Aenean placerat. Ut imperdiet, enim sed gravida sollicitudin, felis odio placerat quam, ac pulvinar elit purus eget enim. Nunc vitae tortor. Proin tempus nibh sit amet nisl. Vivamus quis tortor vitae risus porta vehicula.

My biggest enemy is me ever since day one.
- Stefani Germanotta.

Acknowledgments

Lorem ipsum dolor sit amet, consectetuer adipiscing elit. Ut purus elit, vestibulum ut, placeat ac, adipiscing vitae, felis. Curabitur dictum gravida mauris. Nam arcu libero, nonummy eget, consectetuer id, vulputate a, magna. Donec vehicula augue eu neque. Pellentesque habitant morbi tristique senectus et netus et malesuada fames ac turpis egestas. Mauris ut leo. Cras viverra metus rhoncus sem. Nulla et lectus vestibulum urna fringilla ultrices. Phasellus eu tellus sit amet tortor gravida placerat. Integer sapien est, iaculis in, pretium quis, viverra ac, nunc. Praesent eget sem vel leo ultrices bibendum. Aenean faucibus. Morbi dolor nulla, malesuada eu, pulvinar at, mollis ac, nulla. Curabitur auctor semper nulla. Donec varius orci eget risus. Duis nibh mi, congue eu, accumsan eleifend, sagittis quis, diam. Duis eget orci sit amet orci dignissim rutrum.

Nam dui ligula, fringilla a, euismod sodales, sollicitudin vel, wisi. Morbi auctor lorem non justo. Nam lacus libero, pretium at, lobortis vitae, ultricies et, tellus. Donec aliquet, tortor sed accumsan bibendum, erat ligula aliquet magna, vitae ornare odio metus a mi. Morbi ac orci et nisl hendrerit mollis. Suspendisse ut massa. Cras nec ante. Pellentesque a nulla. Cum sociis natoque penatibus et magnis dis parturient montes, nascetur ridiculus mus. Aliquam tincidunt urna. Nulla ullamcorper vestibulum turpis. Pellentesque cursus luctus mauris.

Contents

1	Introduction	1
2	Preliminary concepts	3
2.1	Dynamical Systems	3
2.2	Bifurcations	4
2.2.1	Saddle-Node bifurcation	4
2.2.2	Pitchfork bifurcation	5
2.2.3	Hopf bifurcation	6
2.3	Localized Structures	6
2.4	Chimera states	6
2.4.1	Kuramoto model	6
2.4.2	Spiral wave chimeras	6
3	Numerical Continuation	7
3.1	Natural parameter continuation	7
3.2	Pseudo-arc length continuation	9
3.3	Continuation of traveling states	11
3.4	Continuation for periodic orbits	13
4	Isolas of localized structures and Raman–Kerr frequency combs in micro-structured resonators (Chaos, Solitons & Fractals 174, 113808)	15
5	Moving spiral wave chimeras (Physical Review E, 104(2), L022203)	25

6	Traveling spiral wave chimeras in coupled oscillator systems: emergence, dynamics, and transitions (New Journal of Physics 25, 103023)	32
7	Conclusions	57
	Bibliography	59

Chapter 1

Introduction

Las partículas o corpúsculos han sido un concepto fundamental y transversal en la física. Clásicamente se describen como un punto material con una masa y posición bien definida. Sin embargo, con el desarrollo de la mecánica cuántica, hemos aprendido que las partículas microscópicas son soluciones localizadas de un campo correspondiente a la amplitud de la probabilidad. Por otro lado, en sistemas macroscópicos fuera del equilibrio, producto del balance entre la inyección y disipación de energía, estos sistemas pueden exhibir soluciones localizadas que, en analogía con el caso anterior, usualmente se denominan soluciones tipo partícula [?]. Estas estructuras localizadas han sido observadas en diversos sistemas de dinámica de fluidos, óptica, química e incluso ecología [?, ?]. Dependiendo del contexto físico en que se observan también reciben el nombre de solitones disipativos, patrones localizados, quimeras, entre otros.

Tradicionalmente, la descripción matemática de las estructuras localizadas se ha realizado usando modelos de reacción difusión [?, ?, ?]. Como el nombre sugiere el acoplamiento espacial ocurre mediante un término de difusión y, por lo tanto, es puramente local. No obstante, diversos sistemas ópticos, neuronales e incluso en vegetación presentan un acoplamiento más complejo y de largo alcance, usualmente llamado acoplamiento no local [?, ?, ?]. En estos casos se ha encontrado que el término no local es responsable de la estabilización de las soluciones tipo partícula [?, ?] y por tanto es fundamental en el entendimiento de estas soluciones.

En esta tesis nos enfocaremos en la dinámica de las estructuras localizadas en sistemas no locales. En particular, buscaremos entender los mecanismos que permiten la propagación de estas soluciones tipo partícula. Para lograrlo, estudiaremos dos sistemas diferentes: solitones disipativos en una cavidad de cristal de fibra fotónico [?], y quimeras espirales en redes bidimensionales de osciladores de fase heterogéneos.

En el primer caso, estudiaremos solitones brillantes y oscuros en resonadores de cavidad de cristal de fibra óptica. Los solitones disipativos temporales han recibido una enorme atención estas últimas décadas por su capacidad de generar *frequency combs* o peines de frecuencia que han revolucionado diversas áreas de la ciencia y tecnología, en particular la espectroscopía de alta precisión y metrología [?, ?]. La mayor parte de estos esfuerzos científicos se han centrado en la generación de solitones mediante un balance entre la nolinearidad Kerr del

material y el acoplamiento local temporal por ejemplo debido a la dispersión [?]. No obstante, en materiales amorfos como lo son los cristales de fibra óptica emerge un acoplamiento no local temporal debido a una respuesta retardada del material a la excitación electromagnética que se conoce como scattering estimulado de Raman [?, ?]. Gracias al efecto Raman es posible la estabilización de estas estructuras localizadas [?]. En este trabajo, buscaremos estudiar cómo son afectadas las estructuras localizadas debido al efecto Raman y la nolinearidad Kerr, y en particular caracterizar precisamente cómo se auto-organizan estas soluciones en función de los parámetros del sistema.

Recientemente hemos podido reducir el modelo paradigmático de Lugiato-Lefever en torno a la emergencia de la biestabilidad encontrando así la ecuación de Swift-Hohenberg. De forma preliminar, hemos encontrado solitones brillantes y oscuros en la ecuación de Swift-Hohenberg con efecto Raman, en la región de coexistencia del estado homogéneo y el estado patrón. Además, debido al acoplamiento no local por efecto Raman, la simetría del sistema se rompe, lo que nos permite encontrar una propagación de las estructuras localizadas y una desconexión de las ramas de solución dando origen a una cadena de isolas, ver figura.

En el segundo caso, analizaremos estados ligados de dos quimeras espirales en redes de osciladores acoplados espacialmente de forma no local. Las quimeras espirales se caracterizan por tener un núcleo incoherente donde los osciladores están desincronizados, rodeado por una estructura coherente en forma de espiral donde los osciladores están sincronizados. Estas soluciones fueron reportadas por primera vez por Kuramoto y Shima hace dos décadas al acoplar osciladores de forma no local [?]. Durante estas últimas dos décadas han sido ampliamente estudiadas en diversos sistemas neuronales, eléctricos e incluso en ecología [?, ?, ?], además de ser observadas experimentalmente en redes de osciladores químicos [?, ?]. Sin embargo, la mayor parte de estos estudios se han centrado en quimeras estacionarias y poco se conoce sobre las quimeras propagativas [?, ?]. En trabajos preliminares, encontramos un nuevo tipo de quimera espiral: un estado ligado de dos espirales propagativas que pueden moverse en una línea recta o siguiendo una trayectoria más compleja.

Mediante simulaciones preliminares hemos logrado encontrar 3 clases de quimeras espirales propagativas: simétricas, asimétricas y cicloidales, junto con su región de estabilidad correspondiente, ver figura ???. Las quimeras simétricas poseen simetría de reflexión y se propagan en la dirección de su eje de simetría mientras que en las quimeras asimétricas, una espiral se vuelve más grande que la otra y se propagan en una dirección inclinada. Por último las espirales cicloidales presentan, además de un movimiento de traslación, una oscilación de sus núcleos que también suele llamarse *meandering* [?].

Chapter 2

Preliminary concepts

2.1 Dynamical Systems

[introducir bien el tema].

The general form for a dynamical system will be the following.

$$\frac{d\mathbf{u}}{dt} = \mathbf{f}(\mathbf{u}, \eta), \quad \mathbf{f} : \mathbb{R}^N \times \mathbb{R}^{n_\eta} \rightarrow \mathbb{R}^N \quad (2.1)$$

Here, \mathbf{u} represents the state vector of the system, it might correspond to the concentrations of different chemicals, the population of certain species or the amplitude of an electric field. The temporal evolution of the state of system is thus determined by the vector function \mathbf{f} . This function may in turn depend on one or several control parameters η relevant to the modeled experiment such as [Aregar parametros]

In this thesis, we will consider different dynamical systems represented by Eq. (2.1) where the function \mathbf{f} will be *nonlinear*. Although one might argue that, at a fundamental level, the physical laws that describe the evolution of a system (Schrödinger equation for example) are linear, when one looks at meso- or macroscopical systems, nonlinear terms naturally arise due to the coarse-graining of the microscopical degrees of freedom [ref Karadr].

In the case of a nonlinear dynamical system, it becomes extremely difficult, and often impossible, to find general explicit solutions of Eq. (2.1). But it turns out that in most cases an in depth description of the model can be provided by studying only the steady states ($\mathbf{f}(\mathbf{u}, \eta) = 0$) and their qualitative changes as parameters are varied. In other words, the problem can be reduced as to find the *equilibria* and *bifurcations* of the system. In the following section, we shall describe the simplest bifurcations a system can experience.

2.2 Bifurcations

Qualitative changes of equilibria as parameters are varied.

2.2.1 Saddle-Node bifurcation

Saddle-node or *fold* bifurcations provide the simplest mechanism for which a pair of stable and unstable equilibria can be created (or destroyed) as the control parameter is changed. Although they arise in a huge variety of systems [insert ref], close to the bifurcation point the dynamics can always be reduced to the following minimal or *normal form*.

$$\frac{du}{dt} = \eta - u^2 \quad (2.2)$$

Following the notation of Eq. (2.1), u represents the state variable and η the control parameter. For $\eta > 0$, the system presents two equilibria $u_{\pm} = \pm\sqrt{\eta}$, where u_+ is stable and u_- unstable. An interesting case occurs when $\eta = 0$, at which point $u = 0$ is half-stable (stable for positive perturbations and unstable for negative perturbations). Lastly, for $\eta < 0$ there are no equilibria. Figure (2.1) provides a visual representation of the previous analysis.

In short, as the bifurcation parameter η is decreased (increased) starting from positive (negative) values, the two equilibria attract (repel) each other and suddenly annihilate (appear).

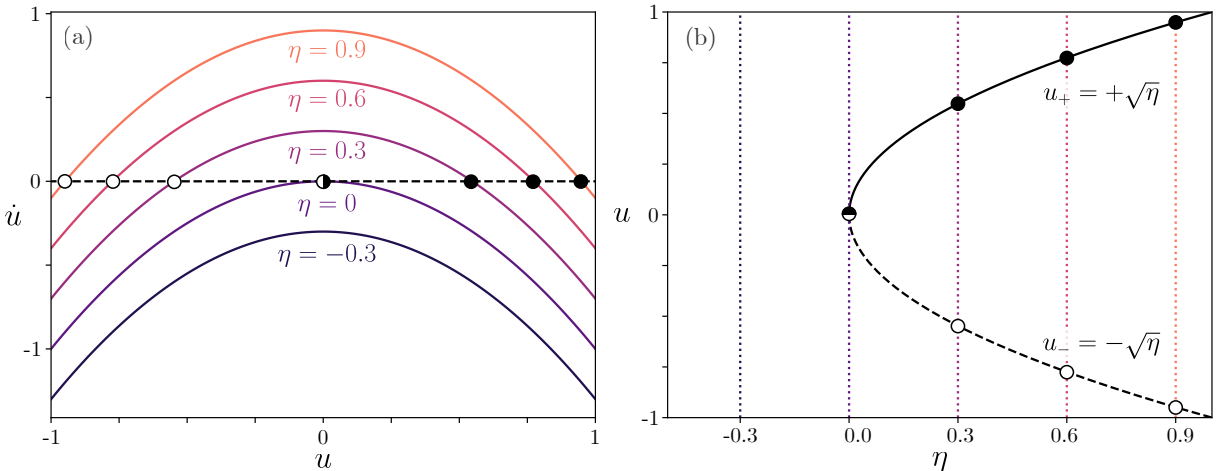


Figure 2.1: Prototypical scenario for a saddle-node bifurcation. (a) Phase space showing both stable and unstable fixed points for different values of η . Black (white) circles represent stable (unstable) fixed points. (b) Bifurcation diagram showing the creation of a stable-unstable pair of fixed points. Solid (dashed) line represents stable (unstable) branch.

Example 2.2.1. For centuries, the mystery of synchronization between fireflies has captivated many people. Although many open questions remain on this topic [ref], we will aim

to shed *light* on this topic only with the knowledge of saddle-node bifurcations and a simple model proposed by Ermentrout and ...[ref].

Consider the problem of a firefly flashing under the presence of a periodically flashing light. We will model the flashing of the firefly with an angular variable θ such that $\theta = 0$ represents the firefly's flash. The firefly has its own inherent frequency ω , i.e. in the absence of stimuli $\dot{\theta} = \omega$. On the other hand, the periodic stimulus will be represented by a phase ϕ that satisfies $\dot{\phi} = \Omega$, where Ω is of course the stimuli period. In order to synchronize with the stimuli, the firefly will either want to speed up if it is lagging behind or slow down if it is going too fast. The simplest non-linear model that fulfills these assumptions is the following,

$$\begin{aligned}\dot{\phi} &= \Omega \\ \dot{\theta} &= \omega + A \sin(\phi - \theta)\end{aligned}$$

Subtracting both equations and defining $\varphi = \dot{\phi} - \dot{\theta}$ yields

$$\dot{\varphi} = \Omega - \omega - A \sin \varphi$$

which can be adimensionalized by rescaling $t \rightarrow At$ and introducing the non dimensional parameter $\mu = (\Omega - \omega)/A$,

$$\dot{\varphi} = \mu - \sin \varphi \tag{2.3}$$

For $\mu = 0$ where the forcing and intrinsic frequencies are the same, there is a stable fixed point at $\varphi = 0$ and an unstable fixed point at $\varphi = \pi$. As μ increases, both equilibria approach each other until they collide for $\mu = \mu_c = 1$ at $\varphi = \pi/2$ and then disappear for $\mu > 1$. We can clearly recognize that the pair of fixed points appear (or disappear) through a saddle-node bifurcation.

Moreover, close to the bifurcation point where $\mu_c = 1$ and $\varphi_c = \pi/2$, we can do a Taylor expansion: $\mu = 1 + \eta$ and $\varphi = \pi/2 + u$ where $\eta, u \ll 1$. Using the identity $\sin \varphi = \sin(\pi/2 + u) = \cos u$ and inserting the previous ansatz into Eq. (2.3) yields the following

$$\begin{aligned}\dot{\varphi} &= \dot{u} = 1 + \eta - \cos u \\ &\approx 1 + \eta - \left(1 - \frac{1}{2}u^2\right) \\ &= \eta - \frac{1}{2}u^2\end{aligned}$$

Which after an adequate rescaling corresponds exactly with the saddle-node normal form.

2.2.2 Pitchfork bifurcation

A *pitchfork* bifurcation constitutes the simplest symmetry breaking bifurcation. More specifically, the

2.2.3 Hopf bifurcation

[insert example]

2.3 Localized Structures

2.4 Chimera states

Phase oscillators

2.4.1 Kuramoto model

2.4.2 Spiral wave chimeras

Chapter 3

Numerical Continuation

In the previous chapter, we mentioned the importance of finding and following the solution branches as they experience several bifurcations. There, we considered simple models where this information could be obtained analytically. However, in the problems considered in this dissertation, and in general, it is not usually possible to do so. Therefore, we must resort to numerical methods, more specifically, *numerical continuation* algorithms. This type of methods aim to solve a nonlinear equation or, more generally, a system of nonlinear equations to find the desired steady states of a dynamical system as parameters are changed. This task corresponds to finding the roots (zeros) of a vector function \mathbf{F} , as in Eq. (3.1).

$$0 = \mathbf{F}(\mathbf{u}, \eta) \quad (3.1)$$

Although there are several methods for finding the roots of a vector function, in this thesis we will only use Newton's method because of its fast (quadratic) convergence and simplicity. This method corresponds to an iterative algorithm that, given an initial guess \mathbf{u}_0 , will perform successive iterations until a certain accuracy or tolerance is reached. Each iteration is computed using Eqs (3.2-3.3), where $\mathbf{J}(\mathbf{u}_i, \eta)$ is the Jacobian of \mathbf{F} . Moreover, since the Jacobian is computed at every point, the stability of the solution and the location of bifurcation points can be determined by tracking the sign of the determinant of the Jacobian.

$$\mathbf{J}(\mathbf{u}_i, \eta) \Delta \mathbf{u}_{i+1} = -\mathbf{F}(\mathbf{u}_i, \eta) \quad (3.2)$$

$$\mathbf{u}_{i+1} = \mathbf{u}_i + \Delta \mathbf{u}_{i+1} \quad (3.3)$$

3.1 Natural parameter continuation

The simplest way to perform numerical continuation is to fix the value of the parameter, in this case η , and solve the equation (or system of equations) by means of Newton's method. Then, one can increase the parameter by a small step $\eta = \eta_0 + \Delta\eta$ and find the new solution using the previous solution \mathbf{u}_0 as initial guess for Newton's method. The process is repeated

until the whole solution branch has been computed. This method is usually called *Natural Parameter Continuation* [2].

Example 3.1.1. To illustrate the method, consider the normal form of the *imperfect pitchfork bifurcation*. Depending on the context, this model could describe magnetization under an external electric field or even optical bistability [refs]. We will keep $\varepsilon > 0$ fixed and find both the stable and unstable solution branches as η is varied.

$$\dot{u} = \eta + \varepsilon u - u^3 \quad (3.4)$$

This task corresponds to finding the roots of a cubic polynomial: $F(u, \eta) = \eta + \varepsilon u - u^3 = 0$. The derivative can be determined easily: $J(u, \eta) = \varepsilon - 3u^2$. Starting the algorithm at $\eta = -0.02$ with the initial guess $u_0 = -0.4$ and moving forward (increasing η) yields the orange triangles shown in Fig. 3.1. Similarly, repeating the process backward (decreasing η) gives the green triangles shown in the same figure.

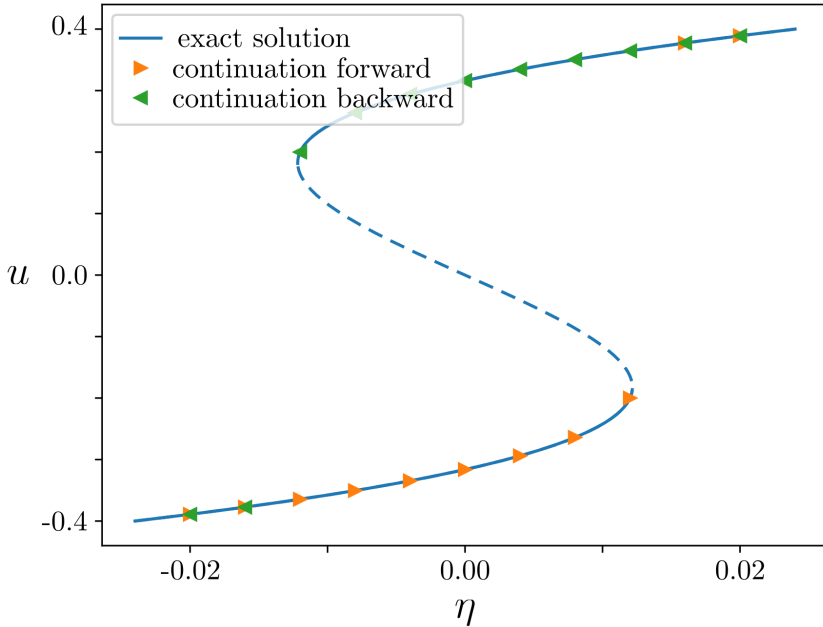


Figure 3.1: Solution of Eq. (3.4) as a function of the parameter η obtained through natural continuation (orange and green triangles) compared to the exact solution (blue curve) with $\varepsilon = 0.1$.

Note that in the example, the natural continuation succeeds at finding the lower and upper solution branches. However, it could not follow the branch past the fold (or saddle-node) bifurcation. The only way to access the middle branch using this algorithm would be to use an adequate initial guess close to the middle branch. Although in this case, it is not difficult to find a good guess, for a higher-dimensional system where the bifurcation scenario is more complicated, this quickly becomes impractical. To overcome this limitation, one can implement a more robust continuation scheme: the *pseudo-arclength continuation*.

3.2 Pseudo-arclength continuation

As shown in the previous example, η is not necessarily a good parameter to describe the solution curve, as it does not follow the branch through folds. A different approach can be taken where the solution branch is parametrized by a different variable: s , which is somewhat similar to the arc-length. Therefore, our goal is to obtain a set of points $\mathbf{y}(s) = (\mathbf{u}(s), \eta(s))$. The *pseudo-arclength* algorithm [4] achieves this goal through essentially two steps.

1. *Predictor step.* Extrapolate a distance Δs along the tangent $\boldsymbol{\tau}_0$ from a previously known point (\mathbf{u}_0, η_0) in the (\mathbf{u}, η) space, to obtain the predicted point (the point used as initial guess).

$$\mathbf{y} = \mathbf{y}_0 + \boldsymbol{\tau}_0 \Delta s$$

2. *Corrector step.* Force the solution to stay at a distance Δs in the plane perpendicular to the tangent. Or, equivalently, that the solution projected onto the tangent has length Δs .

$$(\mathbf{y} - \mathbf{y}_0) \cdot \boldsymbol{\tau}_0 = \Delta s$$

In these steps, a new object has been introduced: the tangent $\boldsymbol{\tau}$ of the solution curve $\mathbf{y}(s)$ which is defined as follows.

$$\boldsymbol{\tau} = \frac{d}{ds} \mathbf{y} = \left(\frac{d\mathbf{u}}{ds}, \frac{d\eta}{ds} \right) \quad (3.5)$$

An additional step must therefore be carried out to implement this method: computing the tangent vector at each point. To do this, it is convenient to revisit Eq. (3.1) and write out the dependence on the new parameter s explicitly.

$$0 = \mathbf{F}(\mathbf{u}(s), \eta(s)) \quad (3.6)$$

Taking the derivative with respect to s on both sides of the previous equation yields

$$0 = \mathbf{J}(\mathbf{u}(s), \eta(s)) \frac{d\mathbf{u}}{ds} + \mathbf{F}_\eta(\mathbf{u}(s), \eta(s)) \frac{d\eta}{ds} \quad (3.7)$$

Note that Eq. (3.7) does not provide a unique solution for the tangent vector. Consequently, another equation must be added by restricting the length of the vector, more specifically, to normalize it.

$$\left\| \frac{d\mathbf{u}}{ds} \right\|^2 + \left(\frac{d\eta}{ds} \right)^2 = 1 \quad (3.8)$$

Without loss of generality, one can fix the value of $\frac{d\eta}{ds} = 1$, solve Eq. (3.7) for $\frac{d\mathbf{u}}{ds}$ and then normalize the obtained vector $\boldsymbol{\tau}$. Since Eq. (3.7) is just a system of linear equations, it can be solved using a standard linear solver. It is important to mention that the sign of $\boldsymbol{\tau}$ must be

chosen such that it has the same orientation as the previously known tangent τ_0 i.e. such that $\tau \cdot \tau_0 > 0$. In the very first step of the continuation method, the previous tangent is unknown. In that case, one can choose the orientation of τ such that its last element (corresponding to $\frac{d\eta}{ds}$) is positive to move forward (increasing η) or negative to move backward (decreasing η).

To simplify the notation, it is convenient to define an extended vector function $\tilde{\mathbf{F}}$ that incorporates \mathbf{F} and the corrector step in the following manner,

$$\tilde{\mathbf{F}}(\mathbf{y}) = \begin{pmatrix} \mathbf{F}(\mathbf{y}) \\ (\mathbf{y} - \mathbf{y}_0) \cdot \tau_0 - \Delta s \end{pmatrix}. \quad (3.9)$$

The corresponding extended Jacobian $\tilde{\mathbf{J}}$ becomes

$$\tilde{\mathbf{J}} = \begin{pmatrix} \mathbf{J} & \mathbf{F}_\eta \\ \frac{d\mathbf{u}}{ds} & \frac{d\eta}{ds} \end{pmatrix}. \quad (3.10)$$

Notice that the last row of the extended Jacobian $\tilde{\mathbf{J}}$ corresponds exactly to the tangent vector τ .

The pseudo-arclength continuation algorithm can be summarized in the following steps.

0. Compute a first point in the solution branch $\mathbf{y}_0 = (\mathbf{u}_0, \eta_0)$, typically through direct numerical simulations. Additionally, one could run Newton's method once while keeping the parameter fixed at $\eta = \eta_0$ to obtain a more accurate approximation for \mathbf{u}_0 .
1. Solve Eq. (3.7) and find the tangent at that point τ_0 . Choose the orientation of τ_0 such that it points in the desired direction on the η -axis.
2. Using $\mathbf{y}_0 + \tau_0 \Delta s$ as initial guess in Newton's method, solve Eq. (3.9) to find the next point in the solution branch \mathbf{y}_{i+1} .
3. Again, solve Eq. (3.7) and find the tangent at that point τ_{i+1} . Choose the orientation such that it matches the previous tangent, $\tau_{i+1} \cdot \tau_i > 0$.
4. Repeat steps 3-4 until the whole solution branch has been computed. One could also track changes in the sign of the determinant of \mathbf{J} in order to estimate the location of bifurcation points.

Example 3.2.1. To illustrate the method, it is useful to revisit the previous example and implement the pseudo-arclength continuation to the same problem. The extended function $\tilde{\mathbf{F}}(u, \eta)$ can be written in the following form,

$$\tilde{\mathbf{F}}(u, \eta) = \begin{pmatrix} \eta + \varepsilon u - u^3 \\ (u - u_0) \frac{du}{ds} + (\eta - \eta_0) \frac{d\eta}{ds} - \Delta s \end{pmatrix}. \quad (3.11)$$

Therefore, the extended Jacobian $\tilde{\mathbf{J}}$ reads,

$$\tilde{\mathbf{J}} = \begin{pmatrix} \varepsilon - 3u^2 & 1 \\ \frac{du}{ds} & \frac{d\eta}{ds} \end{pmatrix}.$$

The tangent vector $\tau = (\tau_u, \tau_\eta)$ can be computed by solving Eq. (3.7). We start by fixing $\frac{d}{ds}\eta = 1$, then $\frac{d}{ds}u$ can be obtained directly,

$$\frac{du}{ds} = -\frac{F_\eta}{J} = -\frac{1}{\varepsilon - 3u^2}.$$

Finally, we normalize τ to obtain the tangent vector.

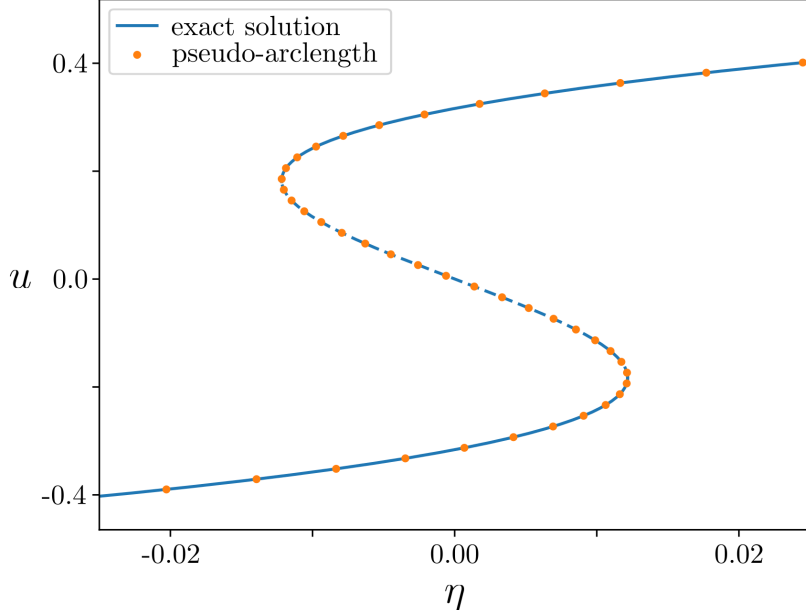


Figure 3.2: Solution of Eq. (3.11) as a function of the parameter η obtained through the pseudo-arclength continuation (orange dots) compared to the exact solution (blue curve).

3.3 Continuation of traveling states

In the particular case of following moving solutions with constant speed c , which is the core of this work, some difficulties arise. The first and most evident one, is that the desired solution is not steady anymore. This can be solved rather easily by changing to the co-moving frame of reference, i.e. by inserting the traveling wave ansatz $\mathbf{u}(x, t) = \mathbf{a}(x - ct)$, where a is the solution profile in the co-moving frame, into Eq. (3.1). Due to the chain rule, an additional term in the form of a spatial derivative appears in the equation,

$$0 = \mathbf{F}(\mathbf{a}, \eta) + c\partial_x \mathbf{a} \quad (3.12)$$

The second problem is that usually the speed c will change as parameters are varied along the solution branch. Therefore, at each step, the speed will have to be determined by the algorithm. The solution to this problem is to add the speed as another unknown, that is to say, we will now be interested in solving for $\mathbf{y} = (\mathbf{a}, c, \eta)$. This leads to the third and final problem, which is that due to the additional unknown, we are missing an additional equation that will guarantee a unique solution to the linearized system. Moreover, we will be

solving these systems considering periodic boundary conditions meaning that a translational invariance will appear. In order to deal with the translational symmetry and guarantee a unique solution, a *phase condition* or *pinning condition* must be established. Indeed, if we find a solution $\mathbf{a}(x)$, then $\tilde{\mathbf{a}}_\theta(x) = \mathbf{a}(x + \theta)$ is also a solution for every θ .

The most widely used condition is the *integral phase condition* [1] which takes a reference solution \mathbf{a}_0 for a certain parameter value η_0 close to the desired solution. The idea is to find the phase that minimizes the difference D between the desired solution \mathbf{a} and the reference solution \mathbf{a}_0 . We can define the difference as follows,

$$D(\theta) = \int_0^L dx' \|\mathbf{a}(x' + \theta) - \mathbf{a}_0(x')\|^2 \quad (3.13)$$

In order to minimize the difference, we differentiate the above equation, set it equal to zero and then integrate by parts. Thus, we arrive at the following condition which is simpler to implement.

$$p(\mathbf{a}, \mathbf{a}_0) = \int_0^L dx' \mathbf{a}(x') \cdot \frac{d\mathbf{a}_0}{dx} \Big|_{x'} = 0. \quad (3.14)$$

We can re-define the extended vector function for which we want to find the root of in the following manner,

$$\mathbf{H}(\mathbf{y}) = \begin{pmatrix} \mathbf{F}(\mathbf{a}, \eta) + c\partial_x \mathbf{a} \\ p(\mathbf{a}, \mathbf{a}_0) \\ q(\mathbf{y}, \mathbf{y}_0) \end{pmatrix} \quad (3.15)$$

The derivative of the integral phase condition with respect to the state vector $p_{\mathbf{a}}$ may differ depending on the chosen phase condition and implementation of the phase condition. In the simplest case, replacing the integral as a Riemann sum (which is the same as the trapezoidal rule in the case of periodic boundary conditions), the derivative reads

$$p_{\mathbf{a}} = \Delta x \frac{d\mathbf{a}_0}{dx}. \quad (3.16)$$

Therefore, the corresponding Jacobian of the extended function reads

$$\mathbf{J}_{\mathbf{H}}(\mathbf{y}) = \begin{pmatrix} \mathbf{J}(\mathbf{a}, \eta) + c\partial_x \mathbf{a} & \partial_x \mathbf{a} & \mathbf{F}_\eta(\mathbf{a}, \eta) \\ p_{\mathbf{a}}(\mathbf{a}_0) & 0 & 0 \\ \dot{\mathbf{a}} & \dot{T} & \dot{\eta} \end{pmatrix}. \quad (3.17)$$

Note that the last row corresponds, once again, exactly to the tangent vector $\tau = (d\mathbf{u}/ds, dT/ds, d\eta/ds) = (\dot{\mathbf{u}}, \dot{T}, \dot{\eta})$.

3.4 Continuation for periodic orbits

If we know wish to follow periodic solutions with the continuation method we must first derive a new set of equations to be solved. Mainly, periodic solutions are not steady solutions of the differential equation, however they satisfy the following boundary-value problem.

$$\frac{d\mathbf{u}}{dt} = \mathbf{F}(\mathbf{u}, \eta) \quad (3.18)$$

$$\mathbf{u}(t=0) = \mathbf{u}(t=T) \quad (3.19)$$

It is convenient to rescale the time $t \rightarrow tT$, therefore the condition for periodicity of the solution becomes $\mathbf{u}(t=0) = \mathbf{u}(t=1)$. Moreover, due to the rescaling in time, a factor T appears on the right-hand side of the dynamical equation. Therefore, the rescaled system becomes,

$$\frac{d\mathbf{u}}{dt} = T\mathbf{F}(\mathbf{u}, \eta) \quad (3.20)$$

$$\mathbf{u}(t=0) = \mathbf{u}(t=1) \quad (3.21)$$

Moreover, due to the additional time-dependence of \mathbf{u} , the parametrizing equation for the pseudo-arclength method needs to be modified accordingly. It now reads,

$$q(\mathbf{y}, \mathbf{y}_0) = \int_0^1 (\mathbf{u}(t) - \mathbf{u}_0(t)) \cdot \frac{d\mathbf{u}}{ds} dt + (T - T_0) \frac{dT}{ds} + (\eta - \eta_0) \frac{d\eta}{ds} - \Delta s = 0 \quad (3.22)$$

Additionally, one can add weights to the previous equation in order to tune the search direction in Newton's method "horizontally" (taking larger steps in the parameter η) or "vertically" (smaller steps in η), see [6] for a more detailed discussion.

Note that we have introduced the period T as another unknown which will be solved through Newton's method along with \mathbf{u} and η , i.e. we want to solve for $\mathbf{y}(t) \equiv (\mathbf{u}(t), T, \eta)$. Moreover, as in the previous section, a phase condition $p(\mathbf{u}, \mathbf{u}_0) = 0$ must be satisfied in order to deal with the translational invariance (in time) and guarantee the uniqueness of the solution. Finally, we can re-define the extended vector function for which we want to find the root of in the following manner,

$$\mathbf{H}(\mathbf{y}) = \begin{pmatrix} T\mathbf{F}(\mathbf{u}, \eta) - \frac{d\mathbf{u}}{dt} \\ p(\mathbf{u}, \mathbf{u}_0) \\ q(\mathbf{y}, \mathbf{y}_0) \end{pmatrix} \quad (3.23)$$

In order to solve this system of equations subject to periodic boundary conditions, many strategies can be followed. Namely, orthogonal collocation methods (implemented in AUTO

[1]), multiple shooting methods [3], and last but not least, finite difference methods (implemented in pde2path [6]). Although the latter has the least accuracy it is by far the simplest to implement. In the finite difference method, a possible approximation to the first equation in the above system is the trapezoidal rule (used for instance in the Crank-Nicolson scheme for simulating PDEs),

$$\left(\frac{F(\mathbf{u}_i) + F(\mathbf{u}_{i+1})}{2} \right) T - \frac{\mathbf{u}_{i+1} - \mathbf{u}_i}{t_{i+1} - t_i} = 0 \quad (3.24)$$

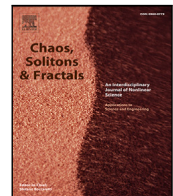
Note that the derivative of \mathbf{u} with respect to t can be written as a product of a matrix ∇_t and the time-discretized vector \mathbf{u}_i ($1 \leq i \leq n_t$), i.e. it can be written as $\nabla_t \mathbf{u}$, in which case the Jacobian \mathbf{J}_H of H reads

$$\mathbf{J}_H(\mathbf{y}) = \begin{pmatrix} T\mathbf{J}(\mathbf{u}, \eta) - \nabla_t & \mathbf{F}(\mathbf{u}, \eta) & T\mathbf{F}_\eta(\mathbf{u}, \eta) \\ p_{\mathbf{u}}(\mathbf{u}_0) & 0 & 0 \\ \dot{\mathbf{u}} & \dot{T} & \dot{\eta} \end{pmatrix}. \quad (3.25)$$

Chapter 4

Isolas of localized structures and Raman–Kerr frequency combs in micro-structured resonators (Chaos, Solitons & Fractals 174, 113808)

In section 2.3 we introduced the concept of dissipative localized structures (LSSs). Here, we will study the formation of such structures in nonlinear optical systems where they are often called optical or cavity solitons. More specifically, we will analyze the paradigmatic Lugiato-Lefever equation (LLE) [5] used to describe fiber resonators, and study the formation of LSSs when a fourth order derivative and a non-local term are considered.



Isolas of localized structures and Raman–Kerr frequency combs in micro-structured resonators

M. Tlidi ^{a,*}, M. Bataille-Gonzalez ^b, M.G. Clerc ^b, L. Bahloul ^{c,d}, S. Coulibaly ^e, B. Kostet ^a, C. Castillo-Pinto ^f, K. Panajotov ^{f,g}

^a Faculté des Sciences, Université libre de Bruxelles (ULB), Campus Plaine, 1050, Brussels, Belgium

^b Departamento de Física and Millennium Institute for Research in Optics, Facultad de Ciencias Físicas y Matemáticas, Universidad de Chile, Casilla 487-3, 1050, Santiago, Chile

^c Electronics Department, Institute of Science, University Center of Tipaza Morsli Abdallah, Ouade Merzouk, 4200, Tipaza, Algeria

^d Laboratoire d'Instrumentation, University of Sciences and Technology Houari Boumediene (USTHB), Algeria

^e Université de Lille, CNRS, UMR 8523-PhLAM-Physique des Lasers Atomes et Molécules, F-59000, Lille, France

^f Brussels Photonics Team, Department of Applied Physics and Photonics (B-PHOT TONA), Vrije Universiteit Brussel, Pleinlaan 2, 1050, Brussels, Belgium

^g Institute of Solid State Physics, Bulgarian Academy of Sciences, 72 Tzarigradsko Chaussee Blvd., 1784, Sofia, Bulgaria

A B S T R A C T

We theoretically investigate the combined impact of the Kerr and stimulated Raman scattering effect on the formation of localized structures and frequency comb generation. We focus on the regime of traveling wave instability. We first perform a real-order parameter description by deriving a Swift–Hohenberg equation with nonlocal delayed feedback. Second, we characterize the motion of traveling wave periodic solutions by estimating their thresholds as well their speed. By using a numerical continuation method, we construct a bifurcation diagram showing the emergence of traveling wave periodic solutions, as well as bright and dark moving localized structures. Numerical simulations of the generalized Lugiato–Lefever equation confirm evidence of isolas of localized structures. More importantly, we show that the stimulated Raman scattering strongly impacts the dynamics of localized structures by creating isolas consisting of bright and dark localized structures, and by inducing a motion of these structures. Finally, we provide a geometrical interpretation of the formation of isola stacks based on dynamical systems theory.

1. Introduction

In the early 2000s, Hänsch and Hall introduced and developed the optical frequency combs, which are equally spaced coherent laser lines [1,2]. They were generated by microcavity resonators and used to count light cycles. Their realization using mode-locked lasers and dissipative solitons has revolutionized many fields of science and technology, such as high-precision spectroscopy, metrology, and photonic analog-to-digital conversion [3,4]. The so-called soliton frequency combs are associated with the formation of localized structures (LSs) of light, which maintain their shape during propagation, and they have been experimentally reported in optical microcavities [5,6]. Those frequency combs are the spectral content of the localized structures, often called dissipative solitons, which have been theoretically predicted in driven cavities [7,8]. Dissipative solitons have been reported in the conservative limit when the injection and losses are both small and under zero frequency detuning limit [9,10]. The link between the localized structure in (micro-)resonators and frequency combs has been established [11–14]. The dynamics of interacting LSs can cause the stabilization of bounded localized states when a periodic

forcing is applied [15–17], when taking into account fourth-order dispersions [18–21] or spatial filtering (or gain dispersion in the time domain) [22]. This is caused by Cherenkov radiation [23–27], i.e., the radiation of dispersive waves that are weakly decaying.

Considerable attention has been paid recently to the formation of frequency combs under the combined action of Kerr nonlinearity and stimulated Raman scattering (SRS) in optical resonators such as whispering gallery mode resonators [28,29]. Since the Raman gain bandwidth is large (it is around 10 THz for silica glass), the combined influence of Raman scattering and Kerr nonlinearity is frequently observed [30–35]. The effects of SRS and Kerr on the front dynamics leading to the stabilization of LSs have recently been studied [36–40] in normal dispersion materials. In this case, LSs have been observed in a domain far from the traveling wave instability. In this regime, it has been shown that the combined action of SRS and Kerr nonlinearity is at the origin of generation of moving bright LSs [36–40]. In the absence of the SRS effect, bright LSs are unstable. The mechanism leading to the formation of LSs with varying width results from the locking front connecting two coexisting continuous wave states [41–44]. Close to the critical point associated with optical bistability, the

* Corresponding author.

E-mail address: mtlidi@ulb.ac.be (M. Tlidi).

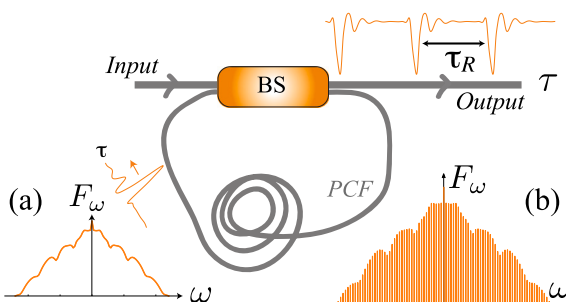


Fig. 1. Schematic setup of a ring cavity filled with a photonic crystal fiber (PCF). The cavity is driven by a coherent external injected beam. BS denotes a beam splitter and τ_R is the roundtrip time. (a) A single moving dark localized structure circulating within the cavity and its Fourier transform. (b) Frequency comb representing the Fourier transform of the train of dark localized structures coming out from the cavity.

interaction law between two well-separated fronts has been established analytically [37,39]. In many cases, properties of such localized states can be related to the phenomenon of collapsed snaking that has been found in the scalar Lugiato–Lefever equation (LLE [45]) with SRS [40] and without SRS [46,47], and in the vectorial case where polarization degree of freedom is considered [48,49].

The dispersion curve may be highly controlled using photonic crystal fibers. Such fibers play a significant role, especially traveling waves (TW) for supercontinuum generation [50–53]. When optical resonators are operating close to the zero dispersion wavelength, it is necessary to take into account higher-order dispersion. In silicon microring resonators, Kerr-Raman scattering and higher order dispersion have an impact on frequency comb formation [54–60]. In particular, complex dynamics characterized by the formation of dispersive waves, self-frequency-shifting, and frequency-locking have been reported [54].

In regimes devoid of traveling modulational instability, the impact of stimulated Raman scattering and the Kerr effect has been reported. In this case, bistability between CW solutions is necessary since the resulting LSs consist of an heteroclinic connection between the two branches of CW states [37,39]. Their bifurcation diagram follows a collapsed snaking type of bifurcation [40].

In this contribution, we theoretically investigate the homoclinic type of LSs in the regime where the system develops a traveling wave instability. Temporal LS can be formed even in the monostable regime. This type of solution has a homoclinic snaking type of bifurcation in the absence of SRS. We show that stimulated Raman scattering breaks the snaking structure and promotes LS branches in the form of isolas, which can form even in the monostable regime.

We show that when this instability becomes subcritical, the system develops a high degree of multistability: besides the continuous wave (CW), and the traveling periodic solutions, which are both stable, an additional variety of stable localized structures are generated. This behavior is independent of whether the system is operating in the monostable or the bistable regime. Using a continuation algorithm, we have established the bifurcation diagram associated with traveling waves. More importantly, we show that localized structures and combs branches of solution are isolas since they are not connected to any modulational instability or traveling wave thresholds.

The structure of the paper is as follows. We describe the creation of periodic TW solutions in the supercritical domain following the presentation of the Swift–Hohenberg equation with stimulated Raman scattering in Section 2. To characterize the motion, we estimate the threshold associated with the onset of motion as a function of injected field amplitude, as well as their speed. We show that when this instability becomes subcritical, the system develops a high degree of multistability: besides the continuous wave (CW), and the traveling periodic solutions, which are both stable, an additional variety of stable localized structures is generated. This behavior is independent of

whether the system is operating in the monostable or bistable regime. Then, in Section 3, we carry out a direct numerical simulation of dark and bright localized structures. We are able to create their bifurcation diagram, which provides proof of the existence of a stable single and multiple isolas, thanks to the continuation algorithm (see Subsection 3.1). In the last part of Subsection 3.2, we present numerical simulations showing that the generalized LLE supports isolas of temporal LSs. Section 4 discusses a geometrical interpretation of isola stack formation. Following the conclusions, we provide as an appendix a full derivation of the Swift–Hohenberg equation with nonlocal delayed feedback.

2. A derivation of a Swift–Hohenberg equation with stimulated Raman scattering

We consider a ring resonator filled-in with a Kerr dispersive medium such as a photonic crystal fiber (PCF). Fig. 1 shows a schematic of the PCF resonator. This resonator is coherently driven by a continuous wave monochromatic light with an electric field E_i and corresponding power E_i^2 . Through the use of a beam splitter, the transmitted portion of this field is directed into the cavity and propagates through the PCF under the influence of dispersion, the Kerr effect, stimulated Raman scattering, and losses. During each round trip, the driving field and the light that moves throughout the resonator are coherently superimposed. High-order chromatic dispersion effects are crucial to the dynamics of this system when the PCF resonator is operating close to the zero dispersion wavelength. Taking into account these effects, the slowly varying envelope of the electric field within the resonator is described by the following generalized Lugiato–Lefever equation [55]

$$\begin{aligned} \frac{\partial E}{\partial \zeta} = & E_i - (1 + i\Delta)E + i(1 - f_r)|E|^2 E \\ & + i\beta_2 \frac{\partial^2 E}{\partial T^2} + i\beta_4 \frac{\partial^4 E}{\partial T^4} \\ & + i f_r E \int_{-\infty}^T \phi(T - T') |E(T')|^2 dT'. \end{aligned} \quad (1)$$

where $E = E(\zeta, T)$ is the normalized mean-field cavity electric field, Δ accounts for the normalized detuning parameter, and losses are normalized to unity. The time ζ is the slow time describing the evolution over successive round trips, and T is the fast time in the reference frame moving with the group velocity of the light within the resonator. E_i is the input field amplitude. β_2 and β_4 are the second- and the fourth-order dispersion terms, respectively. The stimulated Raman scattering is described by the last term of Eq. (1) and by the cubic nonlinear term. The strength of the Raman is f_r . The kernel function is

$$\phi(\tau) = a \exp(-\tau/\tau_2) \sin(\tau/\tau_1)$$

with $a = \tau_0(\tau_1^2 + \tau_2^2)/(\tau_1 \tau_2)$, and $\tau_0 = [|\beta_4 L|/24\alpha]^{1/4}$, where α is the loss parameter, and L is the resonator length. The optical losses are determined by the mirror transmission and the intrinsic material absorption. The choice of this kernel, or influence function, shows an excellent agreement with experiments using standard fibers [61,62]. In the absence of the stimulated Raman scattering, i.e., $f_r = 0$, we recover the LLE with fourth-order dispersion [63]. In this case, Eq. (1) admits front-like states connecting the two continuous wave solutions (CWS) forming a bistable state [41], stationary LSs [18], and moving LSs due to the third-order dispersion effect [19,64–66].

We derive a paradigmatic Swift–Hohenberg equation (SHE) with stimulated Raman scattering describing the evolution of pulses propagating in a photonic crystal fiber resonator. This reduction is performed close to nascent optical bistability. Starting from the generalized LLE Eq. (1), the deviation u of the electric field from its value at the onset of bistability obeys a generalized SHE with stimulated Raman scattering

$$\begin{aligned} \partial_t u = & \eta + \mu u - u^3 + \beta \partial_\tau^2 u - \partial_\tau^4 u \\ & + \int_{-\infty}^\tau \phi(\tau - \tau') u(\tau') d\tau', \end{aligned} \quad (2)$$

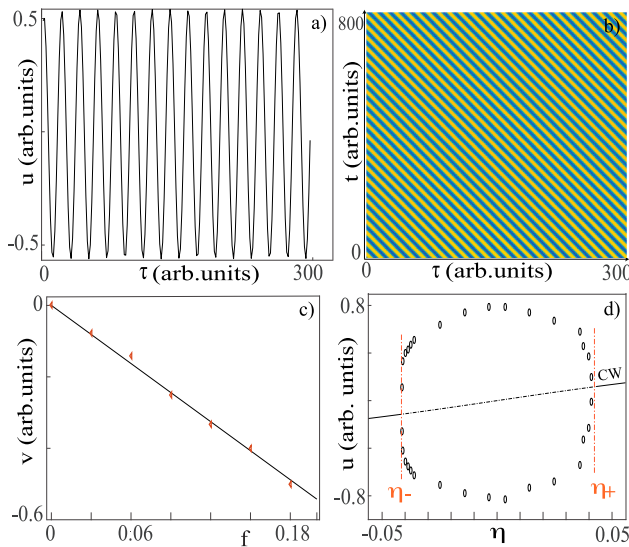


Fig. 2. Traveling wave solutions in the supercritical regime. (a) Profile of a periodic traveling wave solution obtained by numerical simulations of Eq. (2). (b) $t - \tau$ map showing the time evolution of the profile. (c) The velocity of the traveling wave solution v as a function of the strength of the Raman effect. Full line and red triangles show, respectively, the analytical solution (formula Eq. (5)) and numerical simulation results. (d) Supercritical bifurcation diagram obtained in the monostable regime. The full and broken lines correspond to the stable and unstable homogeneous steady state, respectively, while the circles correspond to the maxima and the minima of moving periodic structures. Parameters are $\beta = -1.5$, $\tau_0 = 14$, $f = 0.18$, $\tau_1 = 3$, $\tau_2 = 10$ (a, b, c) $\mu = -0.35$, and $\eta = -0.35$. (For interpretation of the references to color in this figure legend, the reader is referred to the web version of this article.)

A detailed derivation is presented in the Methods section. The parameters η and μ represent, respectively, the driven field and the frequency detuning deviations from their value at the critical point associated with bistability. The second and fourth-derivatives describe dispersion terms. The last contribution accounts for the stimulated Raman scattering with the new kernel function defined as $\phi(\tau) = \sqrt{3}/2af \exp^{-\tau_0(\tau-\tau')/\tau_2} \sin(\tau_0(\tau-\tau')/\tau_1)$ where f is the strength of the nonlocal delayed feedback.

The Fisher–Kolmogorov–Petrovsky–Piscunov (FKPP) equation derived in earlier research [37,39] is much different from Eq. (2). First, because the fourth derivative term originating from high-order dispersion is missing, the FKPP equation is unable to characterize the traveling modulational instability. Second, the scaling in fast and slow times utilized to derive the FKPP equation differs significantly from the scaling used to establish the Swift–Hohenberg with nonlocal response Eq. (2).

In the absence of stimulated Raman scattering, we recover the well-known SHE that has been first derived in the spatial domain [67,68] and in the temporal domain [66]. Without the fourth-order dispersion and the stimulated Raman scattering, Eq. (2) supports stationary localized structures and clusters of them both in the spatial domain [8] and in the temporal domain [66]. In this case, traveling wave instability and motion of temporal structures are forbidden. This is because, in the absence of stimulated Raman scattering and fourth order of dispersion, Eq. (2) is variational. This means that a Lyapunov functional exists for this equation, ensuring that the evolution will move towards the state, for which the functional has the smallest possible value that is compatible with the system boundary conditions.

The linear CW solutions of Eq. (2) satisfies the cubic equation $\eta = u_s^3 - (\mu + \sqrt{3}f/2)u_s = u_s^3 - 3\delta u_s/4$. The linear stability analysis with respect to finite frequency perturbations of the form $\exp(i\lambda t + i\omega\tau)$ yields eigenvalues λ of the linear operator. The CWs states exhibit a traveling wave instability leading to moving periodic solutions when the real part of λ is positive. When taking into account the stimulated Raman scattering and higher order dispersion, a portion of homogeneous solutions

u_s undergo a traveling wave instability in the range $u_- < u_s < u_+$. The thresholds associated with this instability are

$$u_{\pm} = \pm \sqrt{\frac{\beta^2 + 4\mu}{3} - \frac{\sqrt{3}f(\tau_1^2 + \tau_2^2)}{3(\tau_1^2 - \tau_2^2)}}. \quad (3)$$

The corresponding injected field amplitudes are

$$\eta_{\pm} = - \left[\frac{\sqrt{3}f}{6} \frac{\tau_1^2}{\tau_1^2 - \tau_2^2} + \frac{5\sqrt{3}f + 8\mu - \beta}{12} \right] u_{\pm}, \quad (4)$$

where the frequency at both thresholds is $\omega_c^2 = -\beta/2$ with ω_c as the critical frequency. From this threshold emerge periodic traveling wave solutions whose profile and $t - \tau$ map are shown respectively, in Fig. 2(a) and 2(b). We derive an analytical formula for the velocity v of a traveling wave solution. The results are plotted in Fig. 2(c), showing excellent agreement between the analytical formula and numerical results. The bifurcation diagram is shown in Fig. 2(d) indicating that the traveling wave instabilities appear supercritically. The mathematical expressions for the traveling wave instability thresholds η_{\pm} and the corresponding intracavity field amplitudes u_{\pm} are provided explicitly in Methods section, respectively (see Eqs. (3) and (4)). The temporal period at both thresholds is $T_c = 2\pi\sqrt{2}/\sqrt{-\beta}$. We have also estimated the linear velocity of the periodic solution

$$v = \frac{\partial Im(\lambda)}{\partial \omega_c} = \frac{4\sqrt{3}f_r\beta\tau_0^3\tau_1^4\tau_2^4 (\tau_1^2 + \tau_2^2) A_1}{A_2^2}, \quad (5)$$

where A_1 and A_2 are

$$\begin{aligned} A_1 &= [3\beta\tau_1^2\tau_2^2 - 4\tau_0^2(\tau_1^2 - \tau_2^2)] \\ &\quad - 4\tau_0^4(\tau_1^2 + \tau_2^2)^2, \\ A_2 &= \beta\tau_1^2\tau_2^2 [\beta\tau_1^2\tau_2^2 - 4\tau_0^2(\tau_1^2 - \tau_2^2)] \\ &\quad + 4\tau_0^4(\tau_1^2 + \tau_2^2)^2. \end{aligned} \quad (6)$$

The velocity as well as the thresholds associated with the traveling wave instability have been obtained analytically within the limit of a low-frequency regime.

3. Isolas of frequency comb generation

In the absence of stimulated Raman scattering, the fourth-order dispersion strongly affects the dynamical behavior of all fiber resonators by allowing for new unstable frequencies to appear, and the modulational unstable domain to become bounded [63]. In the monostable case, the primary instability threshold is degenerate where two separate frequencies simultaneously appear while in the bistable case, high-frequency modulational instability precedes the limit point [63]. Furthermore, the fourth-order dispersion allows for the stabilization of dark LSs in the temporal [18] and spatial [69] domains. The interaction and pinning can be strongly modified by the influence of high-order dispersion effects [25,26].

Localized structures usually found close to the subcritical modulational instability [7,8] exhibit a well-known homoclinic snaking type of bifurcation that has been first reported in the time domain in [18], and in the spacial domain [69] (see also recent papers on this issue [70,71]). They exhibit multistability behavior in a finite range of parameters referred to as the pinning region [72]. From a dynamical point of view, their bifurcation diagram consists of two snaking curves; one describes LSs with odd number of peaks, the other corresponds to an even number of peaks. The two snaking curves are connected and emerge from the modulational instability threshold. They are intertwined, which is associated with the back-and-forth oscillations across the pinning region. This feature is a characteristic of systems possessing a reflection symmetry in the spatial domain $x \rightarrow -x$ or in the temporal domain $(\tau \rightarrow -\tau)$ such as a Swift–Hohenberg type of equation [73,74] and the Lugiato–Lefever equation [70,71,75].

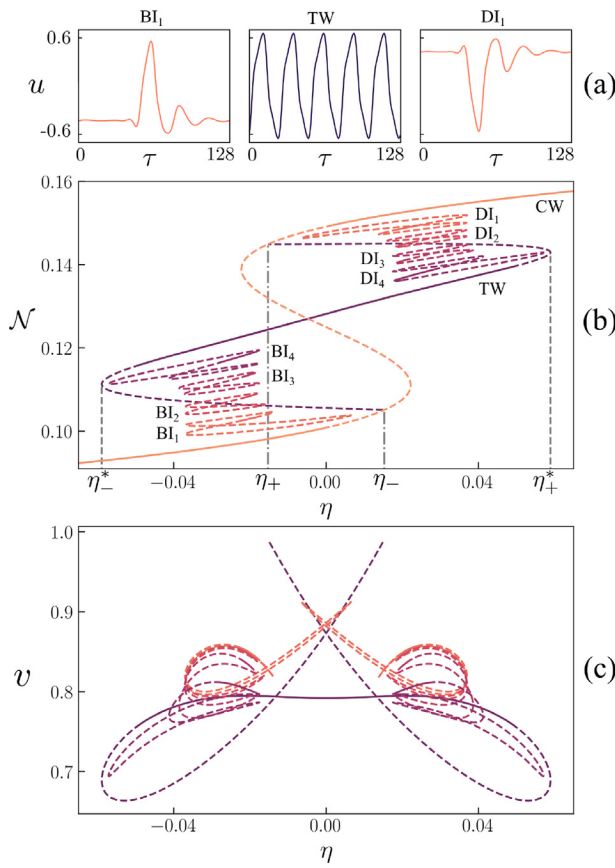


Fig. 3. Isola stack of localized structures obtained by continuation algorithm of Eq. (2). (a) Solution profiles for the respective points in the bifurcation diagram with $\eta = -0.015$, $\eta = 0.003$, and $\eta = +0.014$. (b) Bifurcation diagram obtained in the bistable regime. BI_i and DI_i, i=1,2,3,4 represent bright and dark isolas of solutions with n peaks and n dips, respectively. (c) Speed of LSs as a function of the injection parameter η . Parameters are $\mu = -0.1$, $\beta = -1.8$, $f = 0.28$, $\tau_0 = 1$, $\tau_1 = 3$, and $\tau_2 = 10$. (For interpretation of the references to color in this figure legend, the reader is referred to the web version of this article.)

3.1. Isolas of localized structures in the Swift–Hohenberg equation with nonlocal response

In what follows, we investigate numerically the formation of both bright and dark LSs under the combined influence of SRS-Kerr together with fourth-order dispersion. The presence of stimulated Raman scattering breaks the reflection symmetry and allows for the motion of LS. We focus on a strongly nonlinear regime where the traveling wave bifurcation is subcritical. For this purpose, we proceed by discretizing Eq. (2) in $N = 512$ nodes with a temporal step size of $\Delta\tau = 0.25$. Temporal derivatives with respect to the retarded time τ are then computed spectrally for better accuracy and time integration is performed using a 4th order adaptive Runge–Kutta scheme. Traveling waves and moving bright and dark localized structures solutions of Eq. (2) are obtained by integrating numerically with periodic boundary conditions. They are shown in Fig. 3(a), and they are denoted by TW, BI₁, and DI₁, respectively.

We first seek moving periodic and localized states with constant speed v . These states correspond to solutions of Eq. (2) in the co-moving frame with v

$$0 = \eta + \mu u - u^3 + v\partial_\tau u + \beta\partial_\tau^2 u - \partial_\tau^4 u \quad (7)$$

$$+ \frac{\sqrt{3}}{2fa} \int_{-\infty}^\tau \phi(\tau - \tau')u(\tau')d\tau'.$$

In addition, due to the translational symmetry of the system, we must add a pinning condition in order to ensure the uniqueness of the

solution

$$0 = \int u_0(\tau)\partial_\tau u(\tau)d\tau. \quad (8)$$

This condition can be derived by imposing that the difference with a previously known solution u_0 for a given parameter $\eta_0 \approx \eta$ must be minimized, i.e., $\min_{\Delta\tau} \|D(\Delta\tau)\|$, where $\|\cdot\|$ is the L_2 norm, which will be defined below, and $D(\Delta\tau) \equiv u(\tau + \Delta\tau) - u_0(\tau)$. Eqs. (7) and (8) are solved by means of the pseudo-arclength continuation method [76] which allows to seamlessly follow the solution branch through folds (cf. Fig. 3).

To visualize these solutions, it is convenient to plot the dimensionless L_2 norm,

$$\mathcal{N} = \int d\tau |u - u_s|^2 \quad (9)$$

as a function of η . The results are summarized in the bifurcation diagram shown in Fig. 3(b). The critical thresholds η_{\pm} associated with the TW instability are located on the upper and lower branch of the CW solution.

In the bistable regime, the TW instability always appears subcritically. From the threshold associated with this instability emerges an unstable branch of TW periodic solutions (dotted purple curve). The existence domain of TW periodic solutions is in the range $\eta_-^* < \eta < \eta_+^*$ (purple curve). This branch of TW solutions is connected to the upper threshold η_+ by a dotted purple curve as shown in Fig. 3(b). More importantly, the left (right) portion of Fig. 3(b) shows a set of branches of bright (dark) LS. These localized state branches are distinguished by the multitude of peaks and dips in their temporal structure. An example of periodic TW wave, bright and dark localized structures are shown in Fig. 3(a). The two sets of branches of bright and dark LSs form isolas of localized states that are not connected to the thresholds of the TW instabilities. We estimate the velocity of LSs to better characterize them, and the results are presented in Fig. 3(c). This figure shows that the speed reduces as the number of peaks rises. The isola branch with the purple color corresponds to the single peak solution that is the fastest LSs.

Although both the bright and the dark localized branches of solutions are shown in the bifurcation diagram in Fig. 3, to simplify the analysis, we focus on the dark localized structures. Their shape changes as a function of the strength of the injected field amplitude as shown Fig. 4(a) for the corresponding points A, B, C, and D in the bifurcation diagram of Fig. 4(c). This figure is obtained by zooming in on Fig. 3(b) around the upper CW solution. This portion of the bifurcation diagram reveals clearly that branches of localized structures are not connected to the TW instability. Moving dark localized structures form single or multiple isolas. This feature is displayed in Fig. 4(c). The spectra of dark LS are shown in Fig. 4(b).

3.2. Isolas of localized structures in the generalized LLE with Raman scattering

The reduction from the generalized LLE Eq. (1) to a Swift–Hohenberg equation without a nonlocal delayed response Eq. (2) is a well-known framework for the analysis of periodic or localized structures [8]. It typically applies to systems that experience a modulational instability close to a second-order critical point, marking the onset of a hysteresis loop (nascent bistability). It has been demonstrated that the Swift–Hohenberg equation with high orders of dispersion and no Raman scattering reproduces qualitatively the same results as the full LLE model [66].

In what follows, we shall show that isolas of localized structures are also solutions of the full LLE model Eq. (1). For this purpose, let us fix the detuning parameter by considering the monostable regime, i.e., $\Delta < \sqrt{3}$. Fig. 5 depicts an example of a single peak moving localized structures and their corresponding comb.

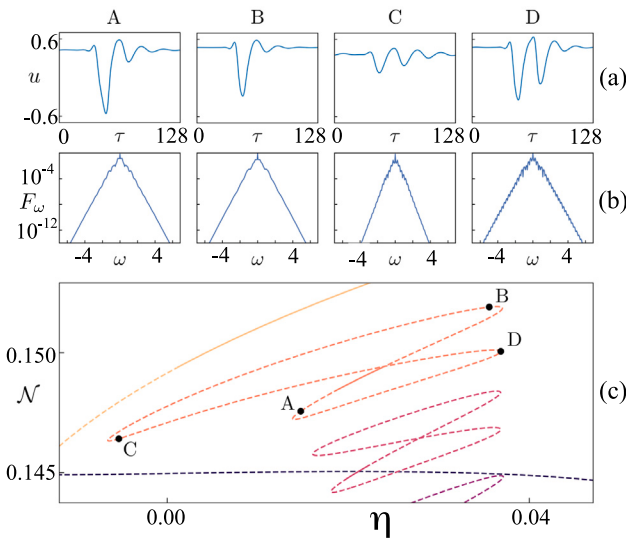


Fig. 4. (a) Solution profiles corresponding to the points A, B, C and D in the bifurcation diagram. (b) Corresponding Fourier spectra. (c) Magnification on the upper CW branch of the bifurcation diagram presented in Fig. 3(b). Same parameters as in Fig. 3. (For interpretation of the references to color in this figure legend, the reader is referred to the web version of this article.)

They are obtained numerically by using a periodic boundary condition compatible with the ring geometry of the optical resonator depicted in Fig. 1. The grid size is 512 with a temporal step size of 0.25.

The $T\text{-}\zeta$ map of Fig. 5(a) depicts traveling temporal localized structures with a constant speed. The motion is directly imputable to the stimulated Raman scattering effect since it breaks the reflection symmetry $\zeta \rightarrow -\zeta$. As shown in Fig. 5(b), the profile of temporal localized structures becomes asymmetric in this case. The spectral content of the intensity profile forms an optical frequency comb that shows an asymmetry as shown in Fig. 5(c). The comb lines are all equally spaced since the free spectral range, given by the inverse of the cavity round-trip time, has a fixed value.

Fig. 6 depicts a single peak localized structure (BI_1), bounded states (BI_2), and a periodic train of peaks (TW) moving at constant speed. The above mentioned continuation algorithm allows for the construction of the bifurcation diagram shown in Fig. 6(b). There are four curves in the plot of the L_2 norm as a function of the injected field E_i . The blue curve displays a single CW solution. The red curve represents the branch of traveling periodic solutions that emerges from the CW solutions. The green and orange curves represent the single and bound branches, which state localized structures with one and two peaks, respectively. Because they are far apart, temporal localized structures interact via their exponentially decaying tails and bounded states. Interactions of localized structure have been studied in the absence of stimulated Raman scattering, in the spatial domain [77]. This weak type of interaction is affected by the third- [25] and the fourth- [26] orders of dispersion.

The profile of a moving peak localized structure is deeply affected by the change of the injected field amplitude. This feature is illustrated in Fig. 7(a). A zoom on that figure shows that neither branches of single and bounded states localized are connected to the CW solutions (see Fig. 7(b)). As in the limit of nascent bistability where the dynamics is governed by a Swift–Hohenberg with nonlocal delayed feedback (Eq. (2)), the generalized LLE Eq. (1) exhibits isola type of solutions. The stimulated Raman scattering is directly responsible for disconnecting the localized branches of solutions from the CW solution. Because we integrate the nonlocal delayed integral term from $-\infty$ to a finite time, the reflection symmetry is broken. However, the branches of periodic TW solutions are still connected to the CW solutions.

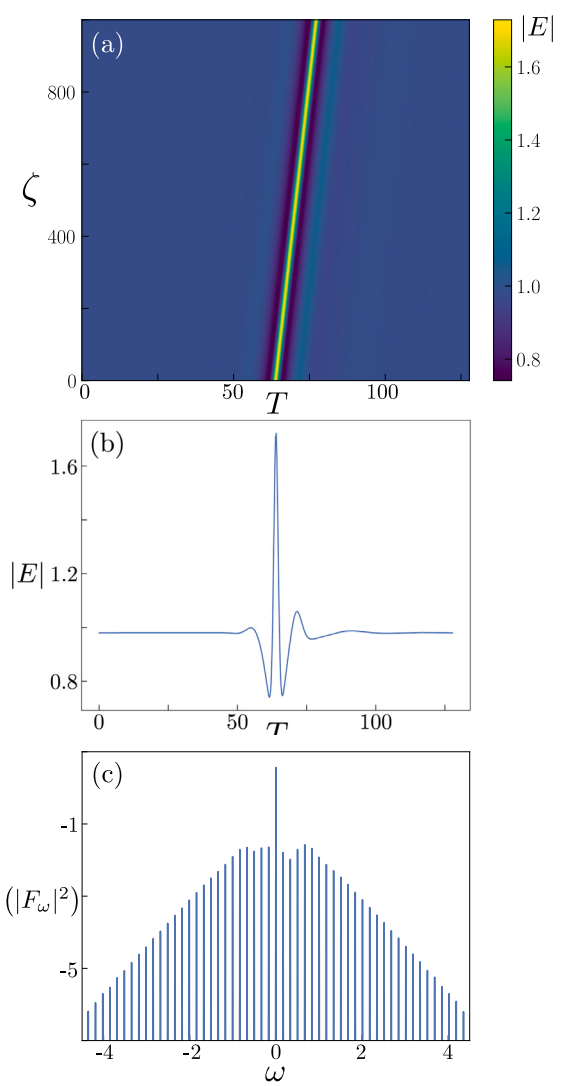


Fig. 5. Moving localized structures obtained by numerical simulations of Eq. (1). (a) $T\text{-}\zeta$ map. (b) Temporal profile (c) Corresponding Fourier spectrum. Parameters are $\Delta = 1.7$, $E_i = 1.219$, $f_r = 0.05$, $\beta_2 = 1$, $\beta_4 = 0.01$, $\tau_0 = 1$, $\tau_1 = 3$, $\tau_2 = 10$. Numerical simulation has been performed using 512 cells, with a T step of 0.25 and a ζ step of 0.001.

In order to better understand the creation of isolas from the perspective of dynamical system theory, we give a geometrical explanation in the next section.

4. Geometrical interpretation

The localized states are stationary solutions of the co-moving frame of Eq. (2). Geometrically, these solutions correspond to homoclinic curves in the phase portrait [78]. The latter is a geometrical representation of the trajectories of the dynamical system of Eq. (2) in the phase plane, which is the Poincaré plane (see Fig. 8). The geometrical interpretation of homoclinic snaking is a well-documented issue and is by now fairly well understood [74]. The homoclinic orbit bifurcates from a heteroclinic loop which is generated by connecting CW (equilibrium) to a periodic orbit. The homoclinic curves correspond to the asymptotic state of the localized solutions and are formed by the intersection of the stable (W^s) and unstable (W^u) manifolds of the uniform equilibrium. The phase portrait's manifold intersection is shown schematically in Fig. 8. The points represent the various localized states or homoclinic curves. Note that the equilibrium that produces manifolds is a hyperbolic equilibrium for the related stationary system and corresponds to

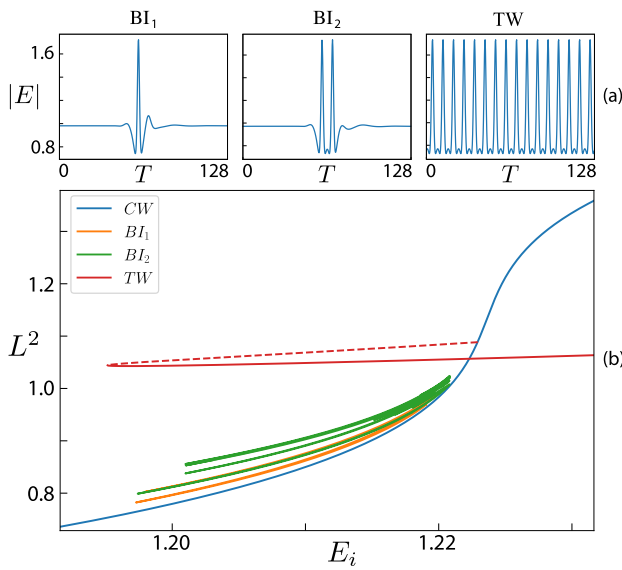


Fig. 6. (a) Temporal profile of a single, bounded states, and periodic train of pulses indicated by \$BI_1\$, \$BI_2\$, and \$TW\$, respectively. (b) Bifurcation diagram representing \$CW\$ (blue curve), train of periodic pulses (red curve) solutions. The unstable branch of \$TW\$ is indicated in dotted curve. The two isolas of localized structures are indicated by green and orange colors, respectively. Parameters are the same as in Fig. 5. (For interpretation of the references to color in this figure legend, the reader is referred to the web version of this article.)

a uniform stable condition of the spatiotemporal system (co-mobile). That is, the manifolds are the nonlinear extension of the eigenvectors associated with the equilibrium.

When the phase portrait's dimension is higher than two, the manifolds surrounding a hyperbolic point exhibit a complicated geometric structure typically referred to as *manifold entanglement* [79,80]. Poincaré first proposed that this entanglement would lead to chaotic behavior in regular temporal systems [81]. The coexistence of localized structures caused by the entangled manifolds in the portrait space of stationary systems is known as the homoclinic snaking bifurcation diagram [74,82]. This coexistence of solutions is characterized by the fact that the symmetrical localized states are connected with other ones with more or less one spatial oscillation. This process occurs through saddle-node bifurcations, generating a snake-like structure in the bifurcation diagram [74]. Experimental observation of this bifurcation diagram has been carried out for a liquid crystal light valve with optical feedback [83]. The ordered sequence of homoclinic curves (localized states) results from spatial reflection symmetry in the system ($\tau \rightarrow -\tau$), where Π represents the spatial reflection symmetry plane.

Then the unstable manifold intercepts the plane of symmetry Π . Due to the reflection symmetry, the stable manifold intercepts Π in a mirror image. This entanglement generates a sequence of symmetric localized states represented by the green dots in Fig. 8(a). The bifurcation diagram associated with LSs contains two intertwined snaking curves. This classical scenario is not expected in irreversible systems, i.e., systems devoid of reflection symmetry. In this case, asymmetric solutions shown in Fig. 3(a) or in Fig. 8(b) are possible. Fig. 8(b) illustrates asymmetrical solutions indicated by black points. These are close to the homoclinic bifurcation diagram, but not connected with other LSs. This behavior is referred to as *isolas* [84–88]. Namely, the solutions only connect with other four asymmetric ones, forming a loop in the phase diagram, typically with the shape of a Lissajous curve (see Figs. 3 and 4(c)).

In the case that the system under study loses reflection symmetry ($\tau \neq -\tau$), the intersection of the stable and unstable manifolds does not coincide generically with the surface Π that initially accounted for the plane of symmetry [89]. Even both manifolds now are not symmetrical.

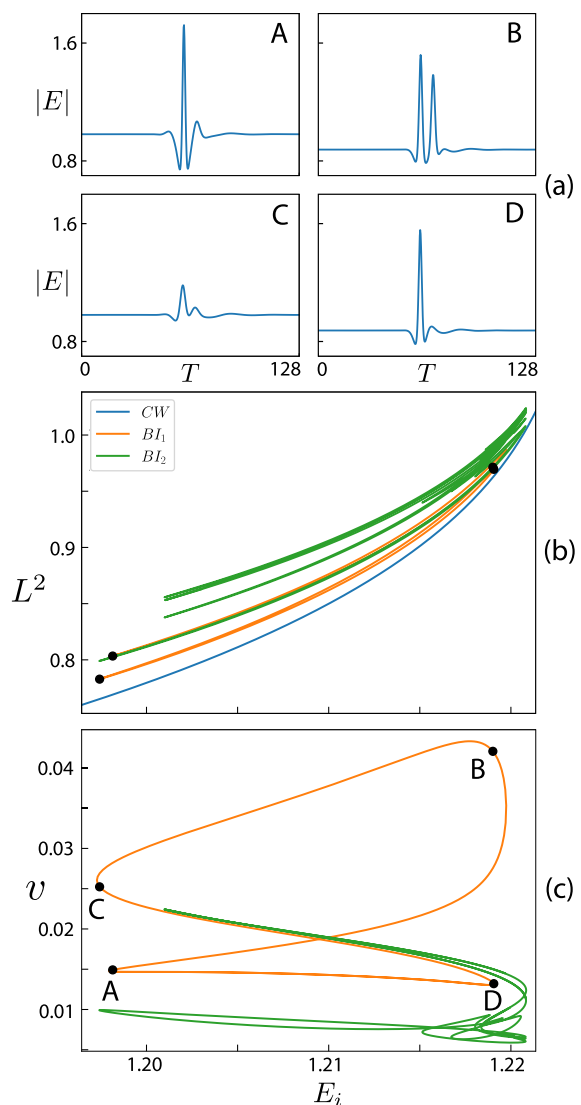


Fig. 7. (a) Profiles of localized structures at different values of the injected field intensity. (b) Zoom of Fig. 6(b) showing isola of solutions for the generalized LLE Eq. (1). (c) Speed of the localized structures as a function of the injected field intensity. Parameters are the same as in Fig. 6. (For interpretation of the references to color in this figure legend, the reader is referred to the web version of this article.)

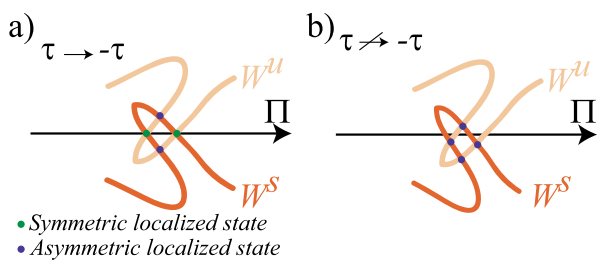


Fig. 8. Schematic representation of stable (\$W^s\$) and unstable (\$W^u\$) manifold in the phase portrait. Representation of intersection of stable and unstable manifolds in systems with reflection symmetry (a) and without symmetry (b). Π accounts for the spatial reflection symmetry plane. The colored dots represent the homoclinic curves (localized structures). (For interpretation of the references to color in this figure legend, the reader is referred to the web version of this article.)

Fig. 8(b) depicts the typical image of the intercepts of manifolds in systems without reflection symmetry. Then all localized structures become asymmetric since there is no ordered sequence imposed by reflection

symmetry. Hence, the system transforms the homoclinic snaking into an isola stack (see Fig. 3) [86,87,89]. Namely the localized structures in the bifurcation diagram are connected by groups of four solutions generically.

In brief, the Swift–Hohenberg Eq. (2) without the effect of stimulated Raman scattering is known to exhibit a homoclinic snaking bifurcation diagram [89]. When taking into account the odd-order of dispersion, the reflexion symmetry is broken. For instance, in the presence of third-order dispersion, bright and dark dissipative solitons become asymmetric and acquire an additional group velocity shift associated with this asymmetry [90]. In this case, isolas of localized structures have been reported [90]. Incorporating the stimulated Raman scattering breaks the reflection symmetry and induces an isola stack. In this case, the homoclinic snaking bifurcation structure breaks up.

5. Conclusions

To sum up, we have investigated the confinement of light in driven nonlinear ring cavities containing a micro-structured photonic crystal fiber. The effects of the Kerr effect, stimulated Raman scattering, and high orders of dispersion on the formation of temporal localized structures have been theoretically examined. In the spectrum domain, these nonlinear solutions correspond to combs.

We performed a real order parameter description leading to the derivation of a Swift–Hohenberg type of equation with a nonlocal delayed response. Due to the presence of stimulated Raman scattering, the resultant Swift–Hohenberg equation is nonvariational, which means that there is no potential or Lyapunov functional to minimize. We show that this equation supports traveling waves solutions. We have characterized them in the supercritical regime. The threshold as well as the speed are estimated.

In the subcritical regime where periodic traveling solutions coexist with stable background (CW solution), both bright and dark moving localized structures are stabilized. These structures are asymmetric and direct numerical simulations have indicated that both structures have an overlapping domain of coexistence. By using a continuation algorithm, we have established their bifurcation diagram and estimated their velocity. More importantly, the stimulated Raman scattering breaks the reflection symmetry and destroys the homoclinic snaking bifurcation structure, allowing for isola stacks of dark localized states to form. This is in contrast with reversible systems that possess the reflection symmetry where the bifurcation diagram consists of two intertwined snaking curves.

The full LLE has been numerically simulated to demonstrate proof of isolas branches of solutions. As a function of the injected field strength, single peak and bounded states of localized branches of solutions have been constructed. Note that there have been reports of other type of localized structures with varying width [37,39,40]. These solutions arise from front interaction, need bistability between CWs for their formation, and exhibit a collapsed snaking type of bifurcation in their bifurcation structure. Contrastingly, the localized states described here are distinct in a number of ways: they have a finite size determined by the frequency that is the most unstable; their formation does not necessitate bistability; and their bifurcation diagram exhibits behavior akin to an isola stack. Finally, we have provided a geometrical interpretation of the impact of broken reflection symmetry mediated by the stimulated Raman scattering on the formation of isola stacks.

Declaration of competing interest

The authors declare that they have no known competing financial interests or personal relationships that could have appeared to influence the work reported in this paper.

Data availability

Data will be made available on request.

Acknowledgments

M.G.C. acknowledges the financial support of ANID– Millennium Science Initiative Program–ICN17-012 (MIRO) and FONDECYT project 1210353. K.P. acknowledges the support by the Fonds Wetenschappelijk Onderzoek-Vlaanderen FWO (G0E5819N) and the Methusalem Foundation. M.T acknowledges financial support from the Fonds de la Recherche Scientifique FNRS under Grant CDR no. 35333527 “Semiconductor optical comb generator”. A part of this work was supported by the “Laboratoire Associé International” University of Lille - ULB on “Self-organisation of light and extreme events” (LAI-ALLURE”).

Compliance with ethics requirements

This article does not contain any studies with human or animal subjects.

Appendix

A.1. Derivation of the Swift–Hohenberg equation with delayed nonlocal response

The purpose of this section is to present the derivation of a Swift–Hohenberg with a delayed nonlocal response, i.e., the stimulated Raman scattering. To do that, we explore the fast-slow time dynamics of the generalized LLE Eq. (1), in the neighborhood of the critical point associated with nascent bistability. At this second-order critical point that marks the onset of a hysteresis loop, the output versus input characteristics have an infinite slope, i.e., $\partial E_i / \partial |E_s| = \partial^2 E_i / \partial |E_s|^2 = 0$ where $|E_s|$ is the CW solutions of Eq. (1) that satisfy $E_i^2 = |E_s|^2[1 + (\Delta - |E_s|^2)^2]$. The coordinates of the critical point associated with bistability are [45]

$$E_c = (3 - i\sqrt{3}) \frac{E_{ic}}{4}, \quad E_{ic}^2 = \frac{8\sqrt{3}}{9}, \quad \text{and} \quad \Delta_c = \sqrt{3}. \quad (10)$$

To explore the vicinity of the second-order critical point, we define a small parameter ϵ which measures the distance from the critical point associated with the bistability as

$$\Delta = \Delta_c + \delta\epsilon^2. \quad (11)$$

We then expand the input field amplitude, and the slowly varying intracavity electric field in terms of ϵ as

$$E_i = E_{ic} + s_1\epsilon + s_2\epsilon^2 + s\epsilon^3 + \dots, \quad (12)$$

$$E = E_c + \epsilon(u_0, v_0) + \epsilon^2(u_1, v_1) \\ + \epsilon^3(u_2, v_2) + \dots \quad (13)$$

where u_i and v_i denote the real and the imaginary parts of the intracavity field. Our goal is to derive a slow time and slow space amplitude equation. A preliminary analysis indicates that we need to consider a small second-order dispersion coefficient $\beta_2 \equiv \epsilon\beta$ to have bounded solutions in both slow and fast time. We seek corrections to the steady states at criticality that depend on slow variables $t = \epsilon^2\zeta$ and $\tau = 3^{1/4}\epsilon T$. We assume in addition that the strength of the delayed Raman effect is small, i.e., $f_r \rightarrow f\epsilon^2$, and we set the β_4 value to one. Replacing the above expansions in the generalized Lugiato–Lefever Eq. (1), we obtain at the leading order in ϵ : $s_1 = 0$ and $u_0 = \sqrt{3}v_0$. At the next order ϵ^2 , we obtain $s_2 = \sqrt{\delta/2\sqrt{3}}$. Finally at ϵ^3 , we get

$$\frac{\partial u_0}{\partial t} = s + \left(\frac{\delta}{\sqrt{3}} - \frac{2f}{3} \right) u_0 - \frac{4}{3\sqrt{3}} u_0^3 \quad (14)$$

$$\begin{aligned}
& + \frac{\beta}{\sqrt{3}} \frac{\partial^2 u_0}{\partial \tau^2} - \frac{1}{\sqrt{3}} \frac{\partial^4 u_0}{\partial \tau^4} \\
& + \frac{2af}{3} \int_{-\infty}^{\tau} e^{-\frac{\tau_0(\tau-\tau')}{\tau_2}} \\
& \sin [\tau_0(\tau-\tau')/\tau_1] u_0(\tau') d\tau',
\end{aligned}$$

With the following changes of parameters $t \rightarrow 3^{3/2}\tau/4$, $\eta = (3^{3/2}/4)s$, $\mu = \sqrt{3}(\sqrt{3}\delta - 2f)/4$, and $\beta \rightarrow 3/4\beta$, we obtain the Swift–Hohenberg equation with stimulated Raman scattering Eq. (2), where the new kernel function is defined as $\phi(\tau) = \sqrt{3}/2af \exp^{-\tau_0(\tau-\tau')/\tau_2} \sin(\tau_0(\tau-\tau')/\tau_1)$.

References

- [1] Jones DJ, Diddams SA, Ranka JK, Stentz A, Windeler RS, Hall JL, et al. Carrier-envelope phase control of femtosecond mode-locked lasers and direct optical frequency synthesis. *Science* 2000;288:635.
- [2] Udem T, Holzwarth R, Hänsch TW. Optical frequency metrology. *Nature* 2002;416:233.
- [3] Fortier T, Baumann E. 20 Years of developments in optical frequency comb technology and applications. *Commun Phys* 2019;2:1.
- [4] Picqué N, Hänsch TW. Frequency comb spectroscopy. *Nature Photon* 2019;13:146.
- [5] Herr T, Brasch V, Jost JD, Wang CY, Kondratiiev NM, Gorodetsky ML, et al. Temporal solitons in optical microresonators. *Nature Photon* 2014;8:145.
- [6] Kippenberg TJ, Gaeta AL, Lipson M, Gorodetsky ML. Dissipative Kerr solitons in optical microresonators. *Science* 2018;361:6402.
- [7] Scroggie AJ, Firth WJ, McDonald GS, Tlidi M, Lefever R, Lugiato LA. Pattern formation in a passive Kerr cavity. *Chaos Solitons Fractals* 1994;4:1323.
- [8] Tlidi M, Mandel P, Lefever R. Localized structures and localized patterns in optical bistability. *Phys Rev Lett* 1994;73:640.
- [9] Nozaki K, Bekki N. Low-dimensional chaos in a driven damped nonlinear Schrödinger equation. *Physica D* 1986;21:381.
- [10] Wabnitz S. Suppression of interactions in a phase-locked soliton optical memory. *Opt Lett* 1993;18:601.
- [11] Matsko AB, Savchenkov AA, Liang W, Ilchenko VS, Seidel D, Maleki L. Mode-locked Kerr frequency combs. *Opt Lett* 2011;36:2845.
- [12] Coen S, Randle HG, Sylvestre T, Erkintalo M. Modeling of octave-spanning Kerr frequency combs using a generalized mean-field Lugiato–Lefever model. *Opt Lett* 2013;38:37.
- [13] Lugiato LA, Prati F, Gorodetsky M, Kippenberg TJ. From the Lugiato–Lefever equation to microresonator-based soliton Kerr frequency combs. *Phil Trans R Soc A* 2018;376:20180113.
- [14] Bao H, Olivier L, Rowley M, Chu ST, Little BE, Morandotti R, et al. Turing patterns in a fiber laser with a nested microresonator: Robust and controllable microcomb generation. *Phys Rev Res* 2020;2:023395.
- [15] Soto-Crespo JM, Akhmediev N, Grelu P, Belhocine F. Quantized separations of phase-locked soliton pairs in fiber lasers. *Opt Lett* 2003;28:1757.
- [16] Olivier M, Roy V, Piché M. Third-order dispersion and bound states of pulses in a fiber laser. *Opt Lett* 2006;31:580.
- [17] Berrios-Caro E, Clerc MG, Leon AO. Flaming 2π kinks in parametrically driven systems. *Phys Rev E* 2016;94:052217.
- [18] Tlidi M, Gelens L. High-order dispersion stabilizes dark dissipative solitons in all-fiber cavities. *Opt Lett* 2010;35:306.
- [19] Tlidi M, Bahloul L, Cherbi L, Hariz A, Coulibaly S. Drift of dark cavity solitons in a photonic-crystal fiber resonator. *Phys Rev A* 2013;88:035802.
- [20] Milian C, Skryabin DV. Soliton families and resonant radiation in a micro-ring resonator near zero group-velocity dispersion. *Opt Express* 2014;22:3732.
- [21] Bahloul L, Cherbi L, Hariz A, Tlidi M. Temporal localized structures in photonic crystal fibre resonators and their spontaneous symmetry-breaking instability. *Phil Trans R Soc A* 2014;372:20140020.
- [22] Turaev D, Vladimirov AG, Zelik S. Long-range interaction and synchronization of oscillating dissipative solitons. *Phys Rev Lett* 2012;108:263906.
- [23] Akhmediev N, Karlsson M. Cherenkov radiation emitted by solitons in optical fibers. *Phys Rev A* 1995;51:2602.
- [24] Skryabin DV, Gorbach AV. Colloquium: Looking at a soliton through the prism of optical supercontinuum. *Rev Modern Phys* 2010;82:1287.
- [25] Vladimirov AG, Gurevich SV, Tlidi M. Effect of Cherenkov radiation on localized-state interaction. *Phys Rev A* 2018;97:013816.
- [26] Vladimirov AG, Tlidi M, Taki M. Dissipative soliton interaction in Kerr resonators with high-order dispersion. *Phys Rev A* 2021;103:063505.
- [27] Brasch V, Geiselmann M, Herr T, Lihachev G, Pfeiffer MHP, Gorodetsky ML, et al. Photonic chip-based optical frequency comb using soliton Cherenkov radiation. *Science* 2016;351:357.
- [28] Spillane SM, Kippenberg TJ, Vahala KJ. Ultralow-threshold Raman laser using a spherical dielectric microcavity. *Nature* 2002;415:621.
- [29] Lin G, Coillet A, Chembo YK. Nonlinear photonics with high-whispering-gallery-mode resonators. *Adv Opt Photonics* 2017;9:828.
- [30] Min B, Yang L, Vahala K. Controlled transition between parametric and Raman oscillations in ultrahigh-Q silica toroidal microcavities. *Appl Phys Lett* 2005;87:181109.
- [31] Liang W, Ilchenko V, Savchenkov A, Matsko A, Seidel D, Maleki L. Passively mode-locked Raman laser. *Phys Rev Lett* 2010;105:143903.
- [32] Karpov M, Guo H, Kordts A, Brasch V, Pfeiffer MHP, Zervas M, et al. Raman self-frequency shift of dissipative Kerr solitons in an optical microresonator. *Phys Rev Lett* 2016;116:103902.
- [33] Liu X, Sun C, Xiong B, Wang L, Wang J, Han Y, et al. Integrated high-Q crystalline AlN microresonators for broadband Kerr and Raman frequency combs. *ACS Photonics* 2018;5:1943.
- [34] Chen-Jinnai A, Kato T, Fujii S, Nagano T, Kobatake T, Tanabe T. Broad bandwidth third-harmonic generation via four-wave mixing and stimulated Raman scattering in a microcavity. *Opt Express* 2016;24:26322.
- [35] Zhu S, Shi L, Ren L, Zhao Y, Jiang B, Xiao B, Zhang X. Controllable Kerr and Raman-Kerr frequency combs in functionalized microsphere resonators. *Nanophotonics* 2019;8:2321.
- [36] Cherenkov AV, Kondratiiev NM, Lobanov VE, Shitikov AE, Skryabin DV, Gorodetsky ML. Raman-Kerr frequency combs in microresonators with normal dispersion. *Opt Express* 2017;25:31148.
- [37] Clerc MG, Coulibaly S, Tlidi M. Time-delayed nonlocal response inducing traveling temporal localized structures. *Phys Rev Res* 2020;2:013024.
- [38] Yao S, Bao C, Wang P, Yang C. Generation of stable and breathing flat-top solitons via Raman assisted four wave mixing in microresonators. *Phys Rev A* 2020;101:023833.
- [39] Clerc MG, Coulibaly S, Parra-Rivas P, Tlidi M. Non-local Raman response in Kerr resonators: Moving temporal localized structures and bifurcation structure. *Chaos* 2020;30:083111.
- [40] Parra-Rivas P, Coulibaly S, Clerc MG, Tlidi M. Influence of stimulated Raman scattering on Kerr domain walls and localized structures. *Phys Rev A* 2021;103:013507.
- [41] Coen S, Tlidi M, Emplit P, Haelterman M. Convection versus dispersion in optical bistability. *Phys Rev Lett* 1999;83:2328.
- [42] Odent V, Tlidi M, Clerc MG, Glorieux P, Louvergneaux E. Experimental observation of front propagation in a negatively diffractive inhomogeneous Kerr cavity. *Phys Rev A* 2014;90:011806(R).
- [43] Xue X, Xuan Y, Liu Y, Wang P-H, Chen S, Wang J, et al. Mode-locked dark pulse Kerr combs in normal-dispersion microresonators. *Nat Photon* 2015;9:594.
- [44] Garbin B, Wang Y, Murdoch SG, Oppo G-L, Coen S, Erkintalo M. Experimental and numerical investigations of switching wave dynamics in a normally dispersive fibre ring resonator. *Eur Phys J D* 2017;71:240.
- [45] Lugiato LA, Lefever R. Spatial dissipative structures in passive optical systems. *Phys Rev Lett* 1987;58:2209.
- [46] Parra-Rivas P, Knobloch E, Gomila D, Gelens L. Dark solitons in the Lugiato–Lefever equation with normal dispersion. *Phys Rev A* 2016;93:063839.
- [47] Parra-Rivas P, Gomila D, Knobloch E, Coen S, Gelens L. Origin and stability of dark pulse Kerr combs in normal dispersion resonators. *Opt Lett* 2016;41:2402.
- [48] Kostet B, Gopalakrishnan S, Averlant E, Soupart Y, Panajotov K, Tlidi M. Vectorial dark dissipative solitons in Kerr resonators. *OSA Continuum* 2021;4:1564.
- [49] Kostet B, Soupart Y, Panajotov K, Tlidi M. Coexistence of dark vector soliton Kerr combs in normal dispersion resonators. *Phys Rev A* 2021;104:053530.
- [50] Yulin AV, Skryabin DV, J. Russell P St. Four-wave mixing of linear waves and solitons in fibers with higher-order dispersion. *Opt Lett* 2004;29:2411.
- [51] Demircan A, Bandelow U. Supercontinuum generation by the modulation instability. *Opt Commun* 2005;244:181.
- [52] Dudley JM, Genty G, Coen S. Supercontinuum generation in photonic crystal fiber. *Rev Modern Phys* 2006;78:1135.
- [53] Dudley JM, Taylor JR, editors. Supercontinuum generation in optical fibers. Cambridge University Press; 2010.
- [54] Milian C, Gorbach AV, Taki M, Yulin AV, Skryabin DV. Solitons and frequency combs in silica microring resonators: Interplay of the Raman and higher-order dispersion effects. *Phys Rev A* 2015;92:033851.
- [55] Chembo YK, Grudinin IS, Yu N. Spatiotemporal dynamics of Kerr-Raman optical frequency combs. *Phys Rev A* 2015;92:043818.
- [56] Lin G, Chembo YK. Phase-locking transition in Raman combs generated with whispering gallery mode resonators. *Opt Lett* 2016;41:3718.
- [57] Cherenkov A, Kondratiiev N, Lobanov V, Shitikov A, Skryabin D, Gorodetsky M. Raman-Kerr frequency combs in microresonators with normal dispersion. *Opt Express* 2017;25:31148.
- [58] Liu K, Yao S, Yang C. Raman pure quartic solitons in Kerr microresonators. *Opt Lett* 2021;46:993.
- [59] Liu M, Huang H, Lu Z, Wang Y, Cai Y, Zhao W. Dynamics of dark breathers and Raman-Kerr frequency combs influenced by high-order dispersion. *Opt Express* 2021;29:18095.
- [60] Liu M, Huang H, Lu Z, Zhou W, Wang Y, Cai Y, et al. Stimulated Raman scattering induced dark pulse and microcomb generation in the mid-infrared. *New J Phys* 2022;24:053003.

- [61] Blow KJ, Wood D. Theoretical description of transient stimulated Raman scattering in optical fibers. *IEEE J Quantum Electron* 1989;25:2665.
- [62] Lin Q, Agrawal GP. Raman response function for silica fibers. *Opt Lett* 2006;31:3086.
- [63] Tlidi M, Mussot A, Louvergneaux E, Kozyreff K, Vladimirov AG, Taki M. Control and removal of modulational instabilities in low-dispersion photonic crystal fiber cavities. *Opt Lett* 2007;32:662.
- [64] Parra-Rivas P, Gomila D, Gelens L. Coexistence of stable dark- and bright-soliton Kerr combs in normal-dispersion resonators. *Phys Rev A* 2017;95:053863.
- [65] Vladimirov AG, Gurevich SV, Tlidi M. Effect of cherenkov radiation on localized-state interaction. *Phys Rev A* 2018;97:013816.
- [66] Hariz A, Bahloul L, Cherbi L, Panajotov K, Clerc M, Ferré MA, et al. Swift-Hohenberg equation with third-order dispersion for optical fiber resonators. *Phys Rev A* 2019;100:023816.
- [67] Mandel P, Georgiou M, Erneux T. Transverse effects in coherently driven nonlinear cavities. *Phys Rev A* 1992;46:4252.
- [68] Tlidi M, Georgiou M, Mandel P. Transverse patterns in nascent optical bistability. *Phys Rev A* 1993;48:4605.
- [69] Tlidi M, Kockaert P, Gelens L. Dark localized structures in a cavity filled with a left-handed material. *Phys Rev A* 2011;84:013807.
- [70] Parra-Rivas P, Gomila D, Matías MA, Coen S, Gelens L. Dynamics of localized and patterned structures in the Lugiato-Lefever equation determine the stability and shape of optical frequency combs. *Phys Rev A* 2014;89:043813.
- [71] Parra-Rivas P, Knobloch E, Gelens L, Gomila D. Origin, bifurcation structure and stability of localized states in Kerr dispersive optical cavities. *IMA J Appl Math* 2021;86:856.
- [72] Pomeau Y. Front motion, metastability and subcritical bifurcations in hydrodynamics. *Physica D* 1986;23:3.
- [73] Champneys AR. Homoclinic orbits in reversible systems and their applications in mechanics, fluids and optics. *Physica D* 1998;112:158.
- [74] Woods PD, Champneys AR. Heteroclinic tangles and homoclinic snaking in the unfolding of a degenerate reversible Hamiltonian Hopf bifurcation. *Physica D* 1999;129:147.
- [75] Gomila D, Scroggie AJ, Firth WJ. Bifurcation structure of dissipative solitons. *Physica D* 2007;227:70.
- [76] Keller HB. Numerical solution of bifurcation and nonlinear eigenvalue problem. In: Application of bifurcation theory. Academic Press; 1977.
- [77] Vladimirov AG, McSloy JM, Skryabin DV, Firth WJ. Two-dimensional clusters of solitary structures in driven optical cavities. *Phys Rev E* 2002;65:046606.
- [78] Coullet P. Localized patterns and fronts in nonequilibrium systems. *Int J Bifurcation Chaos* 2002;12:2445.
- [79] Jackson EA. Perspectives of nonlinear dynamics: Volume 1. Cambridge: Cambridge University Press; 1989.
- [80] Wiggins S. Normally hyperbolic invariant manifolds in dynamical systems. Springer Science & Business Media; 1994.
- [81] Poincaré H. Les Méthodes Nouvelles de la Mécanique Céleste. Vol. III, Paris, 1899 reprint. New York: Dover; 1957.
- [82] Coullet P, Riera C, Tresser C. Stable static localized structures in one dimension. *Phys Rev Lett* 2000;84:3069.
- [83] Haudin F, Rojas RG, Bortolozzo U, Residori S, Clerc MG. Homoclinic snaking of localized patterns in a spatially forced system. *Phys Rev Lett* 2011;107:264101.
- [84] Wadee MK, Coman CD, Bassom AP. Solitary wave interaction phenomena in a strut buckling model incorporating restabilisation. *Physica D* 2002;163:26.
- [85] Beck M, Knobloch J, Lloyd DJ, Sandstede B, Wagenknecht T. Snakes, ladders, and isolas of localized patterns. *SIAM J Math Anal* 2009;41:936.
- [86] Knobloch J, Lloyd DJ, Sandstede B, Wagenknecht T. Isolas of 2-pulse solutions in homoclinic snaking scenarios. *J Dynam Differential Equations* 23:93, 52011.
- [87] Makrides E, Sandstede B. Predicting the bifurcation structure of localized snaking patterns. *Physica D* 2014;268:59.
- [88] Nishiura Y, Watanabe T. Traveling pulses with oscillatory tails, figure-eight-like stack of isolas, and dynamics in heterogeneous media. *Physica D* 2022;440:133448.
- [89] Burke J, Houghton SM, Knobloch E. Swift-Hohenberg equation with broken reflection symmetry. *Phys Rev E* 2009;80:036202.
- [90] Parra-Rivas P, Gomila D, Leo F, Coen S, Gelens L. Third-order chromatic dispersion stabilizes Kerr frequency combs. *Opt Lett* 2014;39:2971.

Chapter 5

Moving spiral wave chimeras
(Physical Review E, 104(2), L022203)

Moving spiral wave chimeras

Martin Bataille-Gonzalez¹, Marcel G. Clerc¹, and Oleh E. Omel'chenko^{2,*}

¹Departamento de Física and Millennium Institute for Research in Optics, Facultad de Ciencias Físicas y Matemáticas, Universidad de Chile, Casilla 487-3, Santiago, Chile

²Institute of Physics and Astronomy, University of Potsdam, Karl-Liebknecht-Straße 24/25, 14476 Potsdam, Germany



(Received 29 March 2021; accepted 4 August 2021; published 20 August 2021)

We consider a two-dimensional array of heterogeneous nonlocally coupled phase oscillators on a flat torus and study the bound states of two counter-rotating spiral chimeras, shortly two-core spiral chimeras, observed in this system. In contrast to other known spiral chimeras with motionless incoherent cores, the two-core spiral chimeras typically show a drift motion. Due to this drift, their incoherent cores become spatially modulated and develop specific fingerprint patterns of varying synchrony levels. In the continuum limit of infinitely many oscillators, the two-core spiral chimeras can be studied using the Ott-Antonsen equation. Numerical analysis of this equation allows us to reveal the stability region of different spiral chimeras, which we group into three main classes—symmetric, asymmetric, and meandering spiral chimeras.

DOI: 10.1103/PhysRevE.104.L022203

Spiral waves are ubiquitous in nature [1]. They can be found in various biological and chemical systems, including cardiac [2] and epithelial [3] tissues, mammalian neocortex [4,5], spatially distributed cell populations [6,7], and oscillatory chemical reactions [8–12]. From a functional point of view, rotating spiral waves are often associated with cardiac arrhythmia and fibrillation [13]. Moreover, such waves have also been observed in two-dimensional cilia arrays [14,15], where they may be related to the transport function of the corresponding tissue or cell colony [16].

Until recently, the mathematical description of spiral waves was mainly based on multicomponent reaction-diffusion systems [17,18] with excitable or oscillatory local dynamics. The effect of diffusion, in this case, guarantees that the spiral wave profile is smooth everywhere, except the phase defect at the tip of the spiral arms. However, is this a correct assumption for biological systems that consist of individual cells and are therefore inherently discrete? In general, these systems can show more complicated dynamical patterns that differ qualitatively from those in continuous media. A wide variety of such unusual patterns has been recently discovered in systems with nonlocal coupling [19–22]. For example, in 2003, Kuramoto and Shima reported the existence of strange spiral waves in two-dimensional arrays of nonlocally coupled limit-cycle oscillators [23,24]. The spiral arms of these waves consist of synchronized/coherent oscillators and resemble the spiral arms of usual spiral waves in continuous media. But the dynamics of the oscillators close to the spiral defect (in the so called spiral core) turns out to be spatially randomized and incoherent such that it masks the position of the phase defect. Similar coexistence of coherent and incoherent dynamics in a homogeneous oscillatory medium is currently known as the *chimera state* (see Refs. [19–22] and references

therein), therefore spiral waves with coherent spiral arms and incoherent cores were called *spiral wave chimeras* [25] or simply *spiral chimeras*.

So far, spiral chimeras have been observed as motionless patterns with fixed positions of their incoherent cores and uniformly rotating coherent spiral arms. In particular, one-core and multicore spiral chimeras were reported in two-dimensional arrays with open boundary conditions [23–25] and periodic boundary conditions representing a flat torus [26–31] or a sphere [32,33]. Beyond phase oscillator models, the existence of spiral chimeras was also confirmed for many realistic systems consisting of limit-cycle oscillators [23,24,34–38], integrate-and-fire neurons [39,40], or even locally chaotic dynamical units [41]. Moreover, recently spiral chimeras were observed in laboratory experiments with the discrete Belousov-Zhabotinsky (BZ) chemical oscillators [42–44].

In this Letter, we show that spiral wave chimeras, in general, do not need to be motionless. Even in translationally invariant systems with isotropic nonlocal coupling, they can move along straight lines or more complicated twisted trajectories. Similarly to moving spiral pairs in oscillatory continuous media [45], the simplest moving spiral chimera looks like a bound state of two reflection-symmetric counter-rotating spirals that move perpendicular to the line connecting their cores. However, due to nonlocal coupling, these chimera states acquire several remarkable properties. First, their core regions are typically spatially modulated. Second, the symmetry breaking in spiral chimeras occurs quite differently than in continuous media [46,47]: Even if the two spiral cores are nonidentical, they continue to drift together. Moreover, in some cases, the direction of the chimera's movement turns out to depend smoothly on system parameters. As a result, asymmetric spiral chimeras can move in arbitrary direction, even along the line connecting their cores.

*Corresponding author: omelchenko@uni-potsdam.de

Model. We consider a two-dimensional array of phase oscillators $\{\theta_{jk}(t)\}_{j,k=1}^N$ evolving according to

$$\frac{d\theta_{jk}}{dt} = \omega_{jk} - \frac{1}{|B_\sigma(j, k)|} \sum_{(m,n) \in B_\sigma(j, k)} \sin(\theta_{jk} - \theta_{mn} + \alpha). \quad (1)$$

Here ω_{jk} are natural frequencies of the oscillators drawn randomly and independently from a Lorentzian distribution $g(\omega) = \gamma/[\pi(\omega^2 + \gamma^2)]$, with width $\gamma > 0$, $\alpha \in (0, \pi/2)$ is the phase lag parameter, $\sigma \in (0, 1/2)$ is the relative coupling radius, and

$$B_\sigma(j, k) = \{(m, n) : (m - j)^2 + (n - k)^2 \leq \sigma^2 N^2\}$$

denotes the circular neighborhood of the point (j, k) where the distances $m - j$ and $n - k$ are considered mod N . The interaction term in Eq. (1) is referred to as nonlocal coupling and is normalized by the number of points $|B_\sigma(j, k)|$ in the neighborhood $B_\sigma(j, k)$.

It is well known [30] that Eq. (1) supports different motionless chimera patterns, including stripe and spot chimera states as well as four-core spiral chimeras. This Letter demonstrates that the same equation also supports a qualitatively different type of chimera states, called *moving spiral chimeras*. Figure 1 provides several examples of such states in the array of 1024×1024 oscillators (see also Ref. [48] for their movies). The left column shows the phase snapshots, while the right column shows the corresponding local order parameters calculated by

$$z_{jk}(t) = \frac{1}{|B_\delta(j, k)|} \sum_{(m,n) \in B_\delta(j, k)} e^{i\theta_{mn}(t)}, \quad (2)$$

with $\delta = 1/(2\sqrt{N})$. By definition, the absolute value $|z_{jk}(t)|$ measures the degree of synchronization between the neighbors of the oscillator $\theta_{jk}(t)$. In particular, $|z_{jk}(t)| = 1$ corresponds to perfect synchrony of the phases, whereas $|z_{jk}(t)| \approx 0$ stands for their complete disorder. Thus a chimera state is characterized by the coexistence of nearly unit values $|z_{jk}(t)|$ in the coherent region with relatively small values of $|z_{jk}(t)|$ in the incoherent region. Notice that to find the positions of incoherent cores it is convenient to use not the local order parameter $z_{jk}(t)$, but a mean field $w_{jk}(t)$ computed by the formula (2) with $\delta = \sigma$. The modulus $|w_{jk}(t)|$ has pronounced minima at the sites, which can be identified with the phase defects of the corresponding spirals.

In our numerical simulations performed with a fixed-step fourth order Runge-Kutta integrator, we have observed three main types of moving two-core spiral chimeras:

(a) Symmetric spiral chimeras. These chimeras have incoherent cores of nearly the same shape and size. In the graph of the local order parameter $z_{jk}(t)$ each incoherent core looks either as a circle with a phase defect in the middle, or as a specific fingerprint pattern composed of curved stripes corresponding to higher and lower local synchrony of the oscillators. Symmetric spiral chimeras move strictly vertically or horizontally.

(b) Asymmetric spiral chimeras. These chimeras have incoherent cores of different shapes and sizes. The cores move

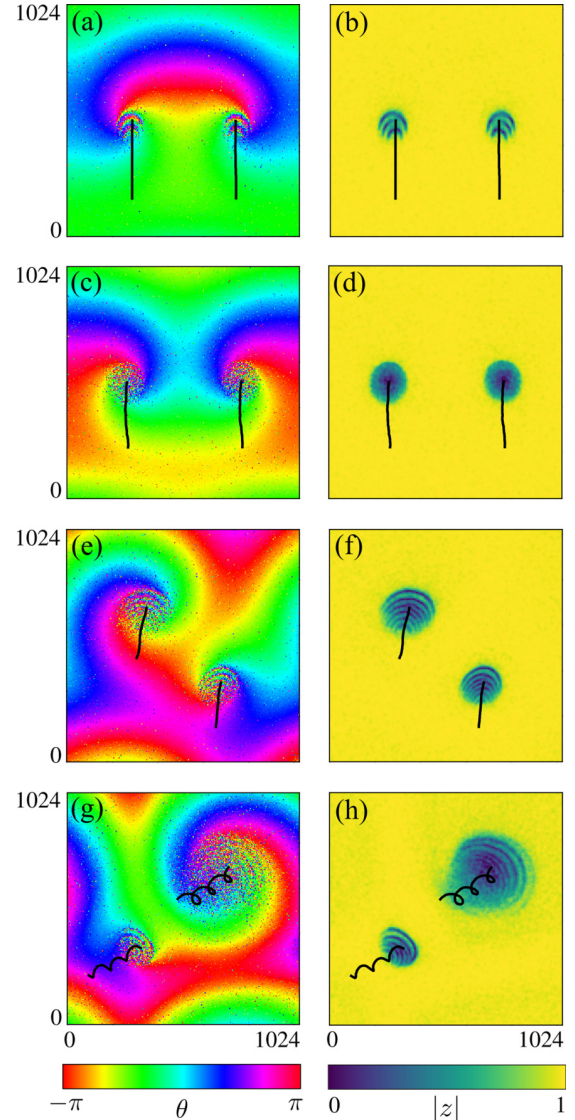


FIG. 1. Moving spiral chimeras in Eq. (1) with $\alpha = 0.6$ [(a) and (b)], $\alpha = 0.7$ [(c) and (d)], $\alpha = 0.8$ [(e) and (f)], and $\alpha = 1.01$ [(g) and (h)]. Other parameters: $N = 1024$, $\sigma = 0.25$, and $\gamma = 0.01$. The left and right columns show snapshots $\theta_{jk}(t)$ and the local order parameters $|z_{jk}(t)|$ computed by (2). The black curves show movement trajectories of the incoherent cores.

along straight lines in a direction, which in general is neither vertical nor horizontal.

(c) Meandering spiral chimeras. These are nonstationary versions of asymmetric spiral chimeras. They move not as a rigid body but rather as a periodically breathing pattern. Their movement trajectories are not straight lines, but twisted curves which can be thought of as a superposition of a uniform drift and oscillatory motion.

In the following, we outline the stability regions in the parameter plane (α, σ) for each of the above moving spiral chimeras.

Methods. For every trajectory of Eq. (1), we can define a piecewise-linear function $Z_N(x, y, t)$ on the flat torus $(x, y) \in$

$[-\pi, \pi]^2$ such that

$$Z_N(-\pi + 2\pi j/N, -\pi + 2\pi k/N, t) = z_{jk}(t).$$

It is well known that in the continuum limit case, i.e., when $N \rightarrow \infty$, the long-term dynamics of $Z_N(x, y, t)$ is asymptotically close to a solution $z(x, y, t)$ of the Ott-Antonsen equation

$$\frac{dz}{dt} = -\gamma z + \frac{1}{2} e^{-i\alpha} \mathcal{G}z - \frac{1}{2} e^{i\alpha} z^2 \mathcal{G}\bar{z}, \quad (3)$$

where \bar{z} denotes the complex conjugate of z , and $\mathcal{G}z$ is a convolution term of the form

$$(\mathcal{G}z)(x, y, t) = \frac{1}{\pi^3 \sigma^2} \iint_{|x-x'|^2 + |y-y'|^2 \leq \pi^2 \sigma^2} z(x', y', t) dx' dy'.$$

Note that the distance $|x - x'|^2 + |y - y'|^2$ in the above integral has to be computed accounting for periodic boundary conditions in the x and y directions. The derivation of Eq. (3) is based on the invariant manifold reduction technique suggested in Ref. [49] and its details can be found in Refs. [21,50]. Thus, the existence and stability of moving spiral chimeras in Eq. (1) can be studied using Eq. (3).

We discretize Eq. (3) on a uniform grid with 256×256 nodes, replace all integrals by trapezoid rule and carry out direct numerical simulations of the resulting ordinary differential equations using the Python *RK45* solver from the SciPy package with adaptive or fixed ($dt = 0.1$) time step. We keep $\gamma = 0.01$ fixed and change parameters σ and α . For every chosen pair (α, σ) we integrate the discretized version of Eq. (3) over 2×10^4 time units. The initial part of the trajectory of the length 10^4 is discarded as a transient and the remaining part of the length 10^4 is analyzed in the following way.

We compute a mean field $w(x, y, t) = (\mathcal{G}z)(x, y, t)$. In the case of a two-core spiral chimera, this complex function has exactly two phase defects where $|w(x, y, t)| = 0$. This allows us to trace the trajectory of each defect and compute its instantaneous velocity $\mathbf{v}(t) = (v_x(t), v_y(t))$. Though the trajectories of two phase defects can be different, the long-time averages $\langle v_x \rangle$ and $\langle v_y \rangle$ calculated along one of the trajectories are the same as those calculated along the other trajectory, therefore we can define two scalars characterizing the spiral chimera motion:

- (i) the mean drift velocity $s = |\langle v_x \rangle + i\langle v_y \rangle|$, and
- (ii) the direction of drift motion

$$\psi = \arg(\langle v_x \rangle + i\langle v_y \rangle).$$

Obviously, for a symmetric spiral chimera, we must obtain $\psi = 0, \pm\pi/2, \pi$, whereas all other values ψ are indications of asymmetric spiral chimeras.

It turns out that all solutions of Eq. (3) corresponding to two-core spiral chimeras assume one of the following two forms. Symmetric and asymmetric spiral chimeras are described by an ansatz

$$z(x, y, t) = a(x - s_x t, y - s_y t) e^{i\Omega t}, \quad (4)$$

where $a(x, y)$ is a complex amplitude and s_x , s_y , and Ω are real constants. A symmetric spiral chimera is obtained if $s_x = 0$ and $a(-x, y) = a(x, y)$ or if $s_y = 0$ and $a(x, -y) =$

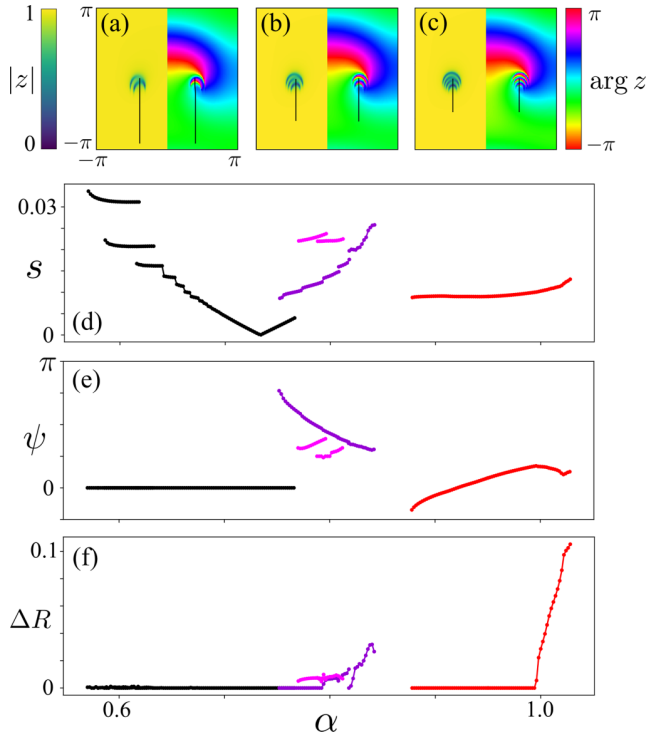


FIG. 2. Mean drift velocity s (d), direction of drift motion ψ (e) and variance of the global order parameter ΔR (f) for two-core spiral chimeras in Eq. (3) with $\sigma = 0.25$ and $\gamma = 0.01$. The black and color dots in (d)–(f) correspond to symmetric and asymmetric spiral chimeras, respectively. Three top panels exemplify solutions $z(x, y, t)$ for $\alpha = 0.58$ (a), $\alpha = 0.60$ (b), and $\alpha = 0.63$ (c). The black curves in these panels show the trajectories of incoherent cores.

$a(x, y)$. Otherwise the spiral chimera is asymmetric. The second ansatz representing meandering spiral chimeras reads

$$z(x, y, t) = a(x - s_x t, y - s_y t, t) e^{i\Omega t}, \quad (5)$$

where the amplitude $a(x, y, t)$ depends explicitly on time. (Typically this dependence is periodic.) In order to distinguish between cases (4) and (5) numerically one can compute the difference $\Delta R = \max_t R(t) - \min_t R(t)$, where

$$R(t) = \left| \frac{1}{4\pi^2} \int_{-\pi}^{\pi} \int_{-\pi}^{\pi} z(x, y, t) dx dy \right|^2$$

is the global order parameter. Then in the former case, one obtains $\Delta R = 0$, while in the latter case one gets $\Delta R > 0$. Therefore spiral chimeras described by formulas (4) and (5) can be called stationary and nonstationary spiral chimeras, respectively.

Results. Using the local order parameters from Fig. 1 as initial conditions and performing forward and backward α -sweeps with the step $d\alpha = 0.002$ for fixed coupling radius $\sigma = 0.25$, we obtained a diagram shown in Fig. 2. Note that two adjacent points were connected by a line only in the case if the right point was obtained in the forward sweep starting from the left point and vice versa. Moreover, each sweep was stopped at the value α for which stable two-core spiral chimeras ceased to exist. Figure 2 reveals that stable symmetric spiral chimeras can be found for $\alpha \in$

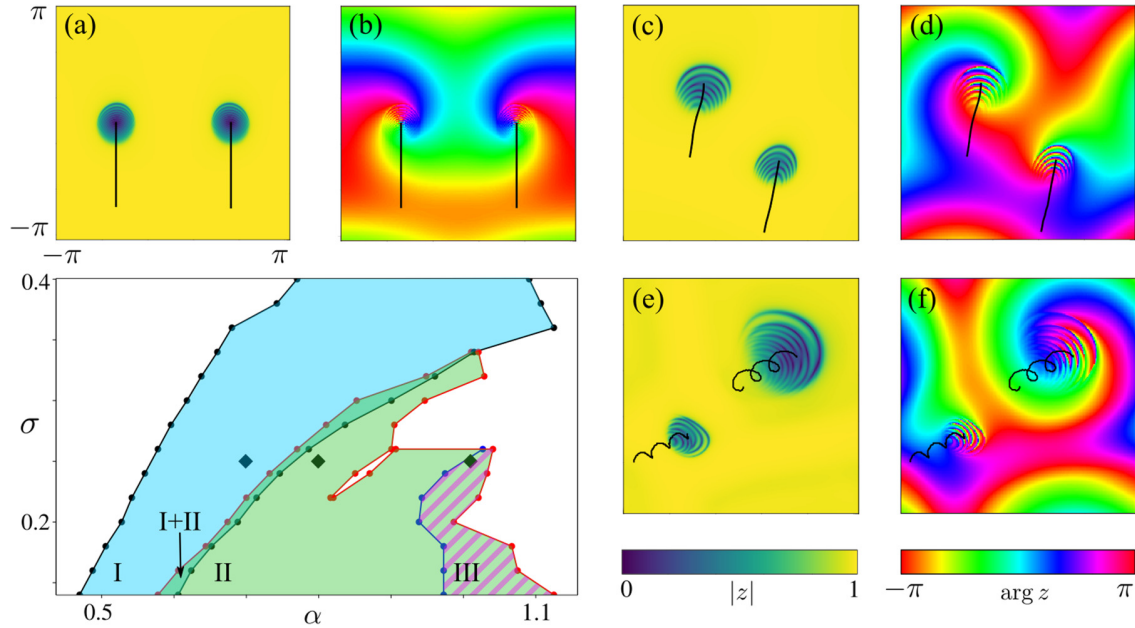


FIG. 3. The main panel (bottom left) shows the stability regions of the symmetric (I), stationary asymmetric (II), and meandering (III) two-core spiral chimeras in the Eq. (3) with $\gamma = 0.01$. The boundaries of these regions consist of the dots, for which α sweeps were carried out, and the interpolating lines. Additional panels exemplify solutions $z(x, y, t)$ for $(\alpha, \sigma) = (0.7, 0.25)$ [(a) and (b)], $(0.8, 0.25)$ [(c) and (d)], and $(1.01, 0.25)$ [(e) and (f)]. These parameters are indicated by diamonds in the stability diagram. The black curves in the panels (a)–(f) show movement trajectories of the incoherent cores.

$[0.57, 0.766]$, whereas stable asymmetric spiral chimeras can be found in two disjoint intervals $\alpha \in [0.752, 0.852]$ and $\alpha \in [0.878, 1.028]$. Note that the ranges of symmetric and asymmetric chimeras have a small overlap where both of them coexist stably. Moreover, several other bi- and tristability ranges can be found in the left and middle parts of the diagram.

The branch of symmetric spiral chimeras consists of several disconnected curves. The chimeras on the leftmost curve are the fastest. Their core regions are simple patterns consisting of two curved stripes corresponding to small values of $|z(x, y, t)|$. On the second and third curves from above we find spiral chimeras with core regions composed of three and four stripes, respectively. The general rule is that for α increasing from 0.57 to 0.734 the motion of spiral chimeras slows down, while the number of stripes in their core regions grows. As a result, these regions begin to look as intricate fingerprint patterns. However, for $\alpha \approx 0.734$ the incoherent stripes merge together and the core regions become circular-shaped, which is typical for motionless spiral chimeras [27].

The branch of asymmetric spiral chimeras also consists of several disconnected curves. All these spiral chimeras have nonvanishing mean velocities $s > 0.008$ and their core regions typically look as fingerprint patterns composed of many incoherent stripes. The most prominent feature of asymmetric spiral chimeras is that for sufficiently large values α they become nonstationary and transform into meandering spiral chimeras. For example, Fig. 2 indicates that asymmetric spiral chimeras are stationary ($\Delta R = 0$) for $\alpha \in [0.752, 0.792]$ (on the slowest part of the branch only) and for $\alpha \in [0.996, 1.028]$. For all other

phase lags these chimeras do not behave as rigidly moving patterns, but breathe periodically on top of the uniform drift motion.

Parameter sweeps similar to Fig. 2 were also performed for other coupling radii σ varying from 0.14 to 0.4 with the step $d\sigma = 0.02$. Thus we obtained a stability diagram shown in Fig. 3. Our general observations can be summarized as follows. The branch of symmetric spiral chimeras has a similar shape for all values σ , though it shifts to larger values α for increasing coupling radius. Regarding the asymmetric spiral chimeras, we found that their stability range has the maximal size for small values σ and shrinks gradually for increasing coupling radius until it eventually vanishes for $\sigma > 0.34$. We also found that the size of the core region of a spiral chimera typically increases with increasing parameters α and σ . However, the mean drift velocity s turns out to be more sensitive to the changes of the coupling radius σ than to the changes of the phase lag α . Notice that two-core spiral chimeras can also be found for coupling radii smaller than 0.14, but in this case their drift velocity decreases significantly and almost vanishes for $\sigma \leq 0.1$ such that they appear as pinned spiral waves or spiral waves moving along closed circular orbits.

Conclusions. Discrete two-dimensional media made up of oscillatory or excitable active units are found in many biological systems. Above, we have shown that under the influence of nonlocal coupling, these media can support moving spiral wave chimeras with a complex distribution of synchronous and asynchronous regions. Using the Ott-Antonsen equation (3), we computed stability diagrams for these chimera states and found how the speed and the direction of their

drift depend on system parameters. This information can be used to search for moving spiral chimeras in experiments similar to Refs. [42–44] or in the cilia carpet system studied theoretically in Ref. [14].

Several interesting questions about the nature of moving spiral chimeras still remain open. First, it seems likely that the distinct solution curves in Fig. 2 are connected by unstable solution branches. Moreover, it is unclear whether there is a branch that connects the moving spiral chimeras with their motionless counterparts. To answer these questions, one needs to perform a more detailed analysis of traveling wave solutions (4) in Eq. (3) by analogy with Refs. [51,52]. The same approach can also be used to study the behavior of moving spiral chimeras for small values of the coupling radius σ , which we have not addressed in this Letter. Another challenging problem is the rigorous mathematical description of moving spiral chimeras in Eq. (1) with identical oscillators. It is known [53,54] that in this case, Eq. (3) becomes singular and can no longer be used. Finally, we emphasize that Eq. (1) can show more complex moving spiral chimeras, see Fig. 4, which also deserve consideration. We hope that further research in the field will answer the above questions and, therefore,

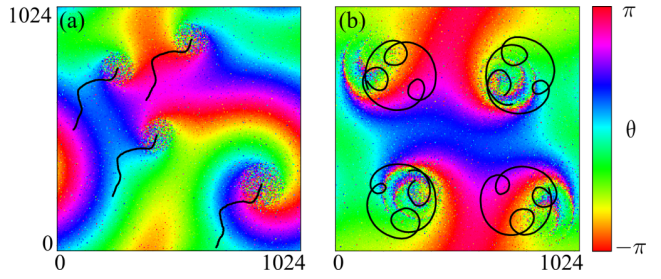


FIG. 4. Four-core moving spiral chimeras in Eq. (1) with $\alpha = 0.8$, $\sigma = 0.2$ (a) and $\alpha = 0.9$, $\sigma = 0.25$ (b). For other parameters and notations see Fig. 1.

improve our understanding of pattern formation in discrete active media with nonlocal coupling.

Acknowledgment. The work of O.E.O. was supported by the Deutsche Forschungsgemeinschaft under Grant No. OM 99/2-1. M.B.G. acknowledges the hospitality of the University of Potsdam during his research internship. M.G.C. thanks for the financial support ANID-Millenium Science Initiative Program-ICN17_012.

- [1] K. Tsuji and S. C. Müller (eds.), *Spirals and Vortices* (Springer, Cham, 2019).
- [2] J. M. Davidenko, A. M. Pertsov, R. Salomonsz, W. Baxter, and J. Jalife, *Nature (London)* **355**, 349 (1992).
- [3] G. Seiden and S. Currant, *New J. Phys.* **17**, 033049 (2015).
- [4] X. Huang, W. C. Troy, Q. Yang, H. Ma, C. R. Laing, S. J. Schiff, and J.-Y. Wu, *J. Neurosci.* **24**, 9897 (2004).
- [5] X. Huang, W. Xu, J. Liang, K. Takagaki, X. Gao, and J.-Y. Wu, *Neuron* **68**, 978 (2010).
- [6] J. Lechleiter, S. Girard, E. Peralta, and D. Clapham, *Science* **252**, 123 (1997).
- [7] J. Lauzeral, J. Halloy, and A. Goldbeter, *Proc. Natl. Acad. Sci. USA* **94**, 9153 (1997).
- [8] A. M. Zhabotinsky and A. N. Zaikin, *J. Theor. Biol.* **40**, 45 (1973).
- [9] A. T. Winfree, *Science* **175**, 634 (1972).
- [10] A. S. Mikhailov and K. Showalter, *Phys. Rep.* **425**, 79 (2006).
- [11] V. K. Vanag and I. R. Epstein, in *Self-Organized Morphology in Nanostructured Materials*, edited by K. Al-Shamery and J. Parisi (Springer, Berlin, 2008), pp. 89–113.
- [12] G. Ertl, *Science* **254**, 1750 (1991).
- [13] R. A. Gray, A. M. Pertsov, and J. Jalife, *Nature (London)* **392**, 75 (1998).
- [14] N. Uchida and R. Golestanian, *Phys. Rev. Lett.* **104**, 178103 (2010).
- [15] R. Golestanian, J. M. Yeomans, and N. Uchida, *Soft Matter* **7**, 3074 (2011).
- [16] W. Gilpin, M. S. Bull, and M. Prakash, *Nat. Rev. Phys.* **2**, 74 (2020).
- [17] A. T. Winfree, *Chaos* **1**, 303 (1991).
- [18] D. Barkley, *Phys. Rev. Lett.* **72**, 164 (1994).
- [19] M. J. Panaggio and D. M. Abrams, *Nonlinearity* **28**, R67 (2015).
- [20] E. Schöll, *Eur. Phys. J. Spec. Top.* **225**, 891 (2016).
- [21] O. E. Omel'chenko, *Nonlinearity* **31**, R121 (2018).
- [22] S. Majhi, B. K. Bera, D. Ghosh, and M. Perc, *Phys. Life Rev.* **28**, 100 (2019).
- [23] Y. Kuramoto and S. Shima, *Prog. Theor. Phys. Suppl.* **150**, 115 (2003).
- [24] S. I. Shima and Y. Kuramoto, *Phys. Rev. E* **69**, 036213 (2004).
- [25] E. A. Martens, C. R. Laing, and S. H. Strogatz, *Phys. Rev. Lett.* **104**, 044101 (2010).
- [26] P.-J. Kim, T.-W. Ko, H. Jeong, and H.-T. Moon, *Phys. Rev. E* **70**, 065201(R) (2004).
- [27] O. E. Omel'chenko, M. Wolfrum, S. Yanchuk, Y. L. Maistrenko, and O. Sudakov, *Phys. Rev. E* **85**, 036210 (2012).
- [28] M. J. Panaggio and D. M. Abrams, *Phys. Rev. Lett.* **110**, 094102 (2013).
- [29] J. Xie, E. Knobloch, and H.-C. Kao, *Phys. Rev. E* **92**, 042921 (2015).
- [30] C. R. Laing, *SIAM J. Appl. Dyn. Syst.* **16**, 974 (2017).
- [31] O. E. Omel'chenko, M. Wolfrum, and E. Knobloch, *SIAM J. Appl. Dyn. Syst.* **17**, 97 (2018).
- [32] M. J. Panaggio and D. M. Abrams, *Phys. Rev. E* **91**, 022909 (2015).
- [33] R.-S. Kim and C.-U. Choe, *Phys. Rev. E* **98**, 042207 (2018).
- [34] X. Tang, T. Yang, I. R. Epstein, Y. Liu, Y. Zhao, and Q. Gao, *J. Chem. Phys.* **141**, 024110 (2014).
- [35] B.-W. Li and H. Dierckx, *Phys. Rev. E* **93**, 020202(R) (2016).
- [36] A. V. Bukh and V. S. Anishchenko, *Chaos Solitons Fract.* **131**, 109492 (2020).
- [37] I. A. Shepelev, A. V. Bukh, S. S. Muni, and V. S. Anishchenko, *Regul. Chaotic Dynam.* **25**, 597 (2020).
- [38] V. Maistrenko, O. Sudakov, and Y. Maistrenko, *Eur. Phys. J. Spec. Top.* **229**, 2327 (2020).
- [39] A. Schmidt, T. Kasimatis, J. Hizanidis, A. Provata, and P. Hövel, *Phys. Rev. E* **95**, 032224 (2017).
- [40] G. Argyropoulos and A. Provata, *Front. Appl. Math. Stat.* **5**, 35 (2019).

- [41] C. Gu, G. St-Yves, and J. Davidsen, *Phys. Rev. Lett.* **111**, 134101 (2013).
- [42] S. Nkomo, M. R. Tinsley, and K. Showalter, *Phys. Rev. Lett.* **110**, 244102 (2013).
- [43] J. F. Totz, J. Rode, M. R. Tinsley, K. Showalter, and H. Engel, *Nat. Phys.* **14**, 282 (2017).
- [44] J. F. Totz, M. R. Tinsley, H. Engel, and K. Showalter, *Sci. Rep.* **10**, 7821 (2020).
- [45] I. S. Aranson, L. Kramer, and A. Weber, *Phys. Rev. E* **47**, 3231 (1993).
- [46] I. S. Aranson, L. Kramer, and A. Weber, *Phys. Rev. E* **48**, R9(R) (1993).
- [47] I. Schebesch and H. Engel, *Phys. Rev. E* **60**, 6429 (1999).
- [48] See the Supplemental Material <http://link.aps.org/supplemental/10.1103/PhysRevE.104.L022203> for movies showing the dynamics of spiral wave chimeras in Figs. 1(a), 1(e), and 1(g).
- [49] E. Ott and T. M. Antonsen, *Chaos* **18**, 037113 (2008).
- [50] C. R. Laing, *Physica D* **238**, 1569 (2009).
- [51] O. E. Omel'chenko, *Nonlinearity* **33**, 611 (2020).
- [52] C. R. Laing and O. E. Omel'chenko, *Chaos* **30**, 043117 (2020).
- [53] O. E. Omel'chenko, *J. Phys. A: Math. Theor.* **52**, 104001 (2019).
- [54] J. Xie, E. Knobloch, and H.-C. Kao, *Phys. Rev. E* **90**, 022919 (2014).

Chapter 6

Traveling spiral wave chimeras in
coupled oscillator systems:
emergence, dynamics, and transitions
(New Journal of Physics 25, 103023)

New Journal of Physics

The open access journal at the forefront of physics

Deutsche Physikalische Gesellschaft  DPG

IOP Institute of Physics

Published in partnership
with: Deutsche Physikalische
Gesellschaft and the Institute
of Physics



PAPER

OPEN ACCESS

RECEIVED

14 June 2023

REVISED

16 September 2023

ACCEPTED FOR PUBLICATION

26 September 2023

PUBLISHED

13 October 2023

Original Content from
this work may be used
under the terms of the
[Creative Commons
Attribution 4.0 licence](#).

Any further distribution
of this work must
maintain attribution to
the author(s) and the title
of the work, journal
citation and DOI.



Traveling spiral wave chimeras in coupled oscillator systems: emergence, dynamics, and transitions

M Bataille-Gonzalez¹, M G Clerc¹ , E Knobloch² and O E Omel'chenko^{3,*} 

¹ Departamento de Física and Millennium Institute for Research in Optics, Facultad de Ciencias Físicas y Matemáticas, Universidad de Chile, Santiago, Chile

² Department of Physics, University of California at Berkeley, Berkeley, CA 94720, United States of America

³ Institute of Physics and Astronomy, University of Potsdam, Karl-Liebknecht-Str. 24/25, 14476 Potsdam, Germany

* Author to whom any correspondence should be addressed.

E-mail: omelchenko@uni-potsdam.de

Keywords: coupled oscillators, chimera state, spiral wave, drift

Supplementary material for this article is available [online](#)

Abstract

Systems of coupled nonlinear oscillators often exhibit states of partial synchrony in which some of the oscillators oscillate coherently while the rest remain incoherent. If such a state emerges spontaneously, in other words, if it cannot be associated with any heterogeneity in the system, it is generally referred to as a chimera state. In planar oscillator arrays, these chimera states can take the form of rotating spiral waves surrounding an incoherent core, resembling those observed in oscillatory or excitable media, and may display complex dynamical behavior. To understand this behavior we study stationary and moving chimera states in planar phase oscillator arrays using a combination of direct numerical simulations and numerical continuation of solutions of the corresponding continuum limit, focusing on the existence and properties of traveling spiral wave chimeras as a function of the system parameters. The oscillators are coupled nonlocally and their frequencies are drawn from a Lorentzian distribution. Two cases are discussed in detail, that of a top-hat coupling function and a two-parameter truncated Fourier approximation to this function in Cartesian coordinates. The latter allows semi-analytical progress, including determination of stability properties, leading to a classification of possible behaviors of both static and moving chimera states. The transition from stationary to moving chimeras is shown to be accompanied by the appearance of complex filamentary structures within the incoherent spiral wave core representing secondary coherence regions associated with temporal resonances. As the parameters are varied the number of such filaments may grow, a process reflected in a series of folds in the corresponding bifurcation diagram showing the drift speed s as a function of the phase-lag parameter α .

1. Introduction

Coupled oscillator systems have played a fundamental role in our understanding and modeling of physical systems since the seminal work of Huygens [1, 2]. More recently, coupled oscillator systems have been used to model certain aspects of neural activity in the brain [3–5], collective dynamics of cilia carpets coupled by hydrodynamic interaction [6, 7], as well as oscillatory and excitable media such as those modeling chemical oscillations [8–11]. In all these examples the key question of interest is the extent of synchronization, both in frequency and in phase, within the oscillator population and its dependence on the oscillator properties and the nature of their coupling. Systems of two coupled oscillators are well described by the Adler equation [12] for the phase difference between the oscillators, but substantial progress is possible in the limit of an infinite number of oscillators, both with all-to-all coupling and with sparse coupling corresponding to different types of oscillator networks. The theory distinguishes between a phase description, in which the amplitude dynamics are adiabatically eliminated, and an amplitude-phase description that is required for highly

nonlinear systems. In either case one tends to find clusters of synchronized oscillators, that is, states of partial synchrony. The theory has numerous key applications, ranging from coupled laser arrays [13] used to maximize power output to the working of the electrical power grid [14]. In each case the identification of the clusters, their number and extent, as well as their stability, represent a major challenge to our understanding of large arrays of coupled oscillators.

If the oscillators are identical and interact attractively, one may expect that all will ultimately oscillate in synchrony. That this is not inevitable was pointed out in 2002 by Kuramoto and Battogtokh [15], who discovered a remarkable state of partial synchrony in a system of coupled identical phase oscillators, in which a subset of the oscillators synchronizes but the remainder remains incoherent. Subsequently called chimera states [16], these states of partial synchrony have been studied by numerous authors in recent years [17–22]. In the simplest case, the oscillators are on a ring and coupled nonlocally via a periodic coupling function. In the presence of a phase lag α in the coupling, the resulting coherent region may drift through the system [23], with oscillators at the leading edge kicked into synchrony while those at the trailing edge fall out of synchrony, thereby maintaining, at least approximately, a constant size of the traveling coherent region. The dynamics of these synchronization and desynchronization fronts thus provide a key to the understanding of the formation of traveling chimera states and their stability properties.

Chimera states are also found in systems of nonidentical oscillators. While less surprising, the resulting states of partial synchrony exhibit similar properties, and in particular motion, whenever the parameter α is nonzero. We distinguish this type of system, in which motion arises spontaneously, from situations in which the motion is forced, for example, via an asymmetrical coupling function [24].

While studies of one-dimensional coupled oscillator arrays are common, similar studies of two- or even three-dimensional oscillator arrays are less frequent. In planar arrays of identical oscillators, one tends to find incoherent cores, surrounded by a rotating coherent spiral wave [25–27] somewhat reminiscent of the rotating spiral waves familiar from oscillatory or excitable media [28, 29]. One may also find coherent cores embedded in an incoherent background [30, 31], although stripe and spot patterns are also possible [32]. In some cases, these may become destabilized via a Hopf bifurcation, leading either to standing oscillating chimera states or to traveling structures as predicted by abstract theory [33]. Three-dimensional arrays support a greater variety of states, most of which are only known via direct numerical simulations [34]. Remarkably, in the special case of a sinusoidal coupling function it is possible to establish the existence and stability properties of such states *semi-analytically* [31, 35, 36], and in particular to predict the onset of spontaneous motion and even the *stability* of the resulting moving structures. This is so even though the transition from stationary to time-dependent chimeras is accompanied in general by the appearance of complex filamentary structures within the incoherent core representing secondary coherence regions associated with temporal resonances between the spiral wave frequency and the spatial translation. These structures, first observed in [35], are a property of quasiperiodic states as explained in [31], and form regardless of whether this state is a standing oscillation as in [31, 35] or, as shown here, a traveling chimera. We show here that the properties of these resonance structures are responsible for much of the remarkable complexity of the associated bifurcation diagram.

Most of the above results have been obtained using Kuramoto's model of phase-coupled oscillators, although some recent work has been devoted to more realistic oscillator systems, among which coupled Stuart-Landau oscillator systems are most popular [37]. However, arrays of both coupled van der Pol oscillators [38] and coupled FitzHugh–Nagumo oscillators [10] have also been studied from this point of view. These models extend the work on the Kuramoto model to include amplitude dynamics in addition to the phases, and in the case of the van der Pol oscillators, to coupled relaxation oscillators, i.e. to oscillators with a strongly nonlinear phase evolution, as well as to excitable systems.

From an experimental perspective, there is a great deal of evidence for the existence of chimera states in one-dimensional arrays of coupled oscillators [8, 11, 39–42], while two-dimensional oscillator arrays (not to mention three-dimensional arrays) remain poorly studied. To the best of our knowledge, the only example of their laboratory realization involves nonlocally coupled Belousov–Zhabotinsky chemical oscillators [8, 9]. In these experiments, spiral wave chimeras were indeed observed, but usually in the form of moving structures. In some cases, this motion resembles a two-dimensional random walk that may be associated with finite-size fluctuations by analogy with one-dimensional systems [43]. On the other hand, spiral wave chimeras with persistent drift motion were also reported. Motivated by the latter observation, we seek the simplest model for studying such drifting structures, and one that allows a detailed study of the emergence and stability properties of uniformly drifting spiral wave chimeras and their parameter dependence, as well as their relationship to other synchronization patterns in the system.

Since the mathematics behind traveling partially coherent states in more realistic systems involving both amplitude and phase dynamics remains largely beyond current reach, we revisit here the Kuramoto model, within which traveling structures can be simulated and, depending on the coupling function adopted,

computed semi-analytically, at least in the continuum limit described by the Ott–Antonsen ansatz [44]. It is important to realize that for identical oscillators the Ott–Antonsen approach precludes a simple self-consistent description of traveling chimera states (see [45, lemma 2] and [46, section 4]). However, this is no longer the case when the oscillators are nonidentical, and in this paper we therefore assume that the oscillator frequencies are drawn from a Lorentzian frequency distribution of width γ . Thus γ becomes an additional (and key) parameter of the system that manifests itself as a damping term in the continuum description.

In recent work [47] we have studied a discrete two-dimensional oscillator system of this type with a nonlocal coupling function and showed that this system is able to support bound states of two counter-rotating spiral waves with incoherent cores that drift either rigidly or exhibit more complex meandering motion. The specific example considered in [47] was a two-dimensional array of phase oscillators $\{\theta_{jk}(t)\}_{j,k=1}^N$ evolving according to

$$\frac{d\theta_{jk}}{dt} = \omega_{jk} - \frac{1}{|B_\sigma(j,k)|} \sum_{(m,n) \in B_\sigma(j,k)} \sin(\theta_{jk} - \theta_{mn} + \alpha). \quad (1)$$

This equation implies that each oscillator (j, k) interacts only with its neighbors within the circular region

$$B_\sigma(j,k) = \left\{ (m,n) : (m-j)^2 + (n-k)^2 \leq \sigma^2 N^2 \right\},$$

where the distances $m-j$ and $n-k$ are considered mod N and $\sigma \in (0, 1/2)$ is the relative coupling radius. The interaction is normalized by the number of points $|B_\sigma(j,k)|$ in the region $B_\sigma(j,k)$ and involves a phase lag parameter $\alpha \in [0, \pi/2]$. In addition, it is assumed that the oscillators are heterogeneous in the sense that their natural frequencies ω_{jk} are drawn randomly and independently from a Lorentzian distribution

$$g(\omega) = \frac{\gamma}{\pi} \frac{1}{\gamma^2 + \omega^2} \quad (2)$$

of width $\gamma > 0$.

The system (1) was found to exhibit a large variety of different moving spiral wave chimeras associated with the complex spatial structure of their incoherent cores, as summarized in figure 1 for two different values of the phase lag parameter α . In particular, these states exhibit staggered coexistence as a function of α (see below), behavior that is associated with different numbers of crescent-shaped filaments in the core of a moving spiral, hereafter referred to as fingerprint patterns (see figure 1(b–d)). Similar slanted snaking bifurcation diagrams have been observed for spatially localized states in both fluid and optical systems [48–52] and are a consequence of the nonlocal nature of the system (1). As a result the relationship between the presence of stable, albeit moving chimera states and the system parameters is exceedingly intricate and remains to be elucidated.

In this paper we are able to identify, for the first time, the main prerequisites necessary for the emergence of moving spiral wave chimeras of different types and to establish their stability properties. To this end we formulate a version of problem (1) that is tractable semi-analytically, and employ extensive numerical continuation to follow distinct states through parameter space, together with their stability properties. This approach builds a picture of the parameter space of the problem, enables us to identify the different chimera states that are possible, and ultimately allows a detailed understanding of the system. Our results are corroborated using extensive direct numerical simulations of this system and provide a roadmap for understanding more realistic coupled oscillator systems.

2. Results

The model (1) is a particular case of a more general nonlocally coupled system

$$\frac{d\theta_{jk}}{dt} = \omega_{jk} - \left(\frac{2\pi}{N} \right)^2 \sum_{m,n=1}^N G_{jk;mn} \sin(\theta_{jk} - \theta_{mn} + \alpha) \quad (3)$$

with

$$G_{jk;mn} = G \left(\frac{2\pi(j-m)}{N}, \frac{2\pi(k-n)}{N} \right),$$

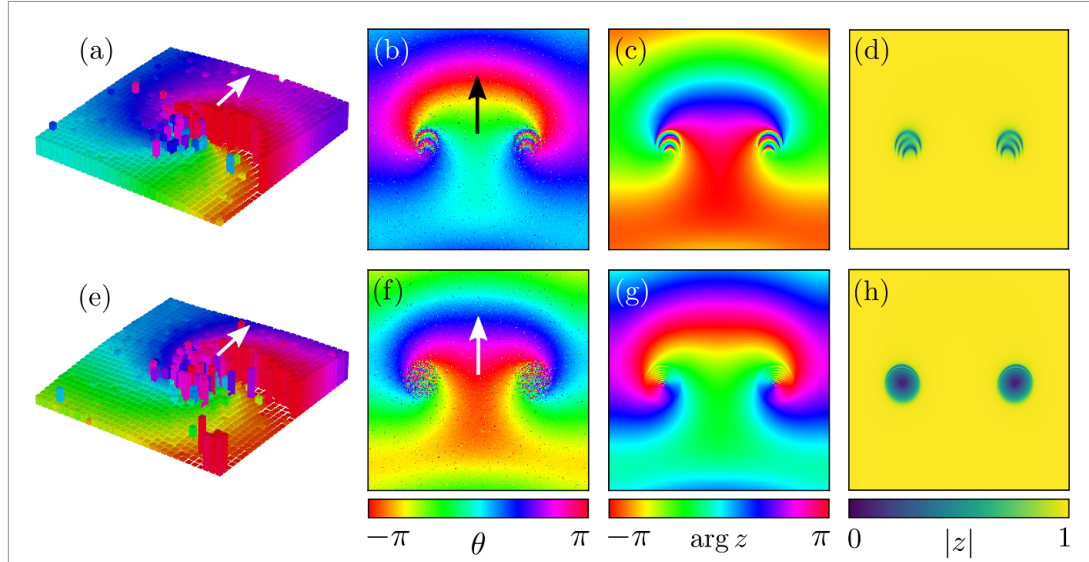


Figure 1. Moving spiral wave chimeras (two left columns) in the discrete oscillator array (1) and their continuum limit counterparts (two right columns) determined from equation (6). The arrows indicate the drift direction. Panels (a) and (e) focus on the behavior of the phase near a single spiral core while panels (b) and (f) present snapshots of the corresponding phase $\theta_{jk}(t)$ of the full array of oscillators, revealing the presence of a pair of incoherent spiral cores surrounded by a coherent region in the form of a rotating spiral. The pattern moves in the y direction at a constant speed. Under appropriate conditions, the incoherent cores break up into nested filamentary structures (panels (b) and (c)). Panels (c) and (g) show snapshots of $\arg z(x, y, t)$ while panels (d) and (h) show snapshots of $|z(x, y, t)|$, a representation that eliminates the global spiral wave frequency Ω and focuses on the fingerprint structure of their spiral cores. The continuum limit evidently provides an accurate description of the discrete system, even for a moderate number of oscillators. The supplementary material [53] provides an animation of the state in panels (c) and (g). Parameters: $N = 128$, $\gamma = 0.01$, $\sigma = 0.25$ with $\alpha = 0.6$ (top row) and $\alpha = 0.7$ (bottom row).

where $G(x, y)$ is a non-constant coupling function, which is 2π -periodic with respect to x and y and satisfies the symmetry conditions

$$G(-x, y) = G(x, -y) = G(-x, -y) = G(x, y) \quad (4)$$

and the normalization condition

$$\int_{-\pi}^{\pi} \int_{-\pi}^{\pi} G(x, y) dx dy = 1.$$

Indeed, if we assume

$$G(x, y) = \begin{cases} 1/(\pi^3 \sigma^2) & \text{for } x^2 + y^2 \leq \pi^2 \sigma^2, \\ 0 & \text{for } x^2 + y^2 > \pi^2 \sigma^2 \end{cases} \quad (5)$$

in the square domain $(x, y) \in [-\pi, \pi]^2$, then equation (3) reduces to model (1). The resulting coupling function $G(x, y)$ is shown in figure 2(a).

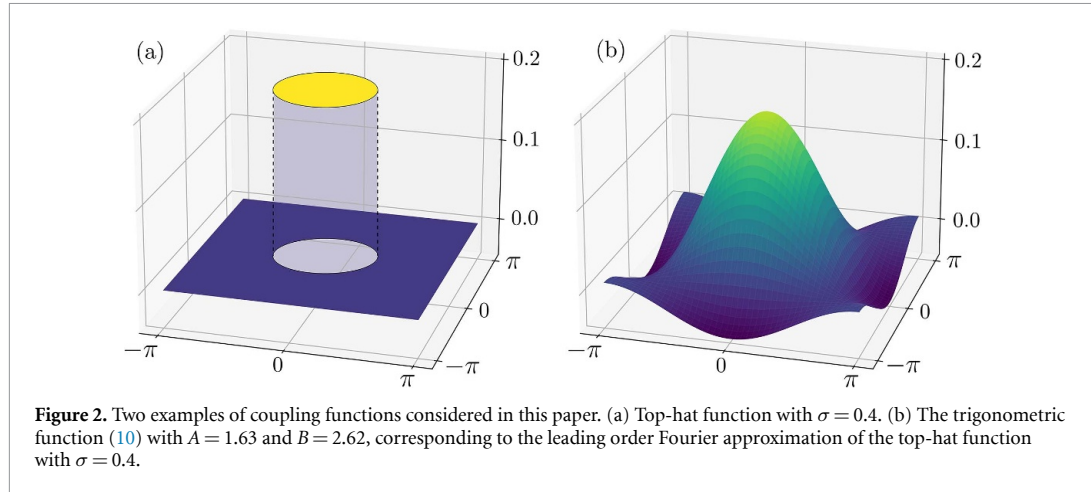
It is well-known [19, 54, 55] that in the continuum limit $N \rightarrow \infty$ the long-term dynamics of equation (3) settle down on the Ott–Antonsen manifold parametrized by a complex-valued function $z(x, y, t)$. This function is the local order parameter at the position (x, y) at time t and quantifies the synchronization degree of oscillators $\theta_{jk}(t)$ with $(-\pi + 2\pi j/N, -\pi + 2\pi k/N) \approx (x, y)$. Importantly, in the case of Lorentzian-distributed natural frequencies ω_{jk} the evolution of $z(x, y, t)$ is described by the integro-differential equation

$$\frac{dz}{dt} = -\gamma z + \frac{1}{2} e^{-i\alpha} \mathcal{G}z - \frac{1}{2} e^{i\alpha} z^2 \bar{\mathcal{G}}z, \quad (6)$$

where the damping parameter $\gamma > 0$ is determined by the width of the distribution in equation (2) and

$$(\mathcal{G}z)(x, y, t) = \int_{-\pi}^{\pi} dx' \int_{-\pi}^{\pi} G(x - x', y - y') z(x', y', t) dy'$$

is a convolution-type integral operator with the coupling function $G(x, y)$ from (3). The above observation allows us to use equation (6) as a mathematical tool for investigating the properties of moving spiral wave chimeras in the system (3).



The discrete system (3) is invariant under discrete translations in two directions, while the continuum description (6) is invariant under continuous translations. Both are in addition invariant with respect to the group D_4 of rotations and reflections of a square inherited from the coupling function. The problem (6) is therefore invariant under the group $T^2 \dot{+} D_4$, the semidirect product of the two-torus of translations and the discrete group D_4 . The solutions of this problem may respect certain subgroups of this symmetry group or have no symmetry. This observation applies to both stationary and drifting states. In particular, every uniformly drifting state satisfying equation (6), including the simplest moving spiral wave chimeras, corresponds to a solution of the form

$$z(x, y, t) = a(x - s_x t, y - s_y t) e^{i\Omega t}, \quad (7)$$

where $(s_x, s_y)^T \in \mathbb{R}^2$ is the velocity vector and $\Omega \in \mathbb{R}$ is the collective phase frequency. In the case $s_x = s_y = 0$, the pattern is called motionless or stationary. If, in addition, we also have $\Omega = 0$, the corresponding pattern is called static.

From the symmetry conditions (4) it follows that among all possible moving solutions (7) there are two special solution types related to these symmetries: solutions of the form

$$z(x, y, t) = a(x, y - st) e^{i\Omega t} \quad (8)$$

with $s \in \mathbb{R}$ and $a(-x, y) = a(x, y)$ (hereafter Z_2 symmetry) corresponding to uniform motion in the y direction, and solutions of the form

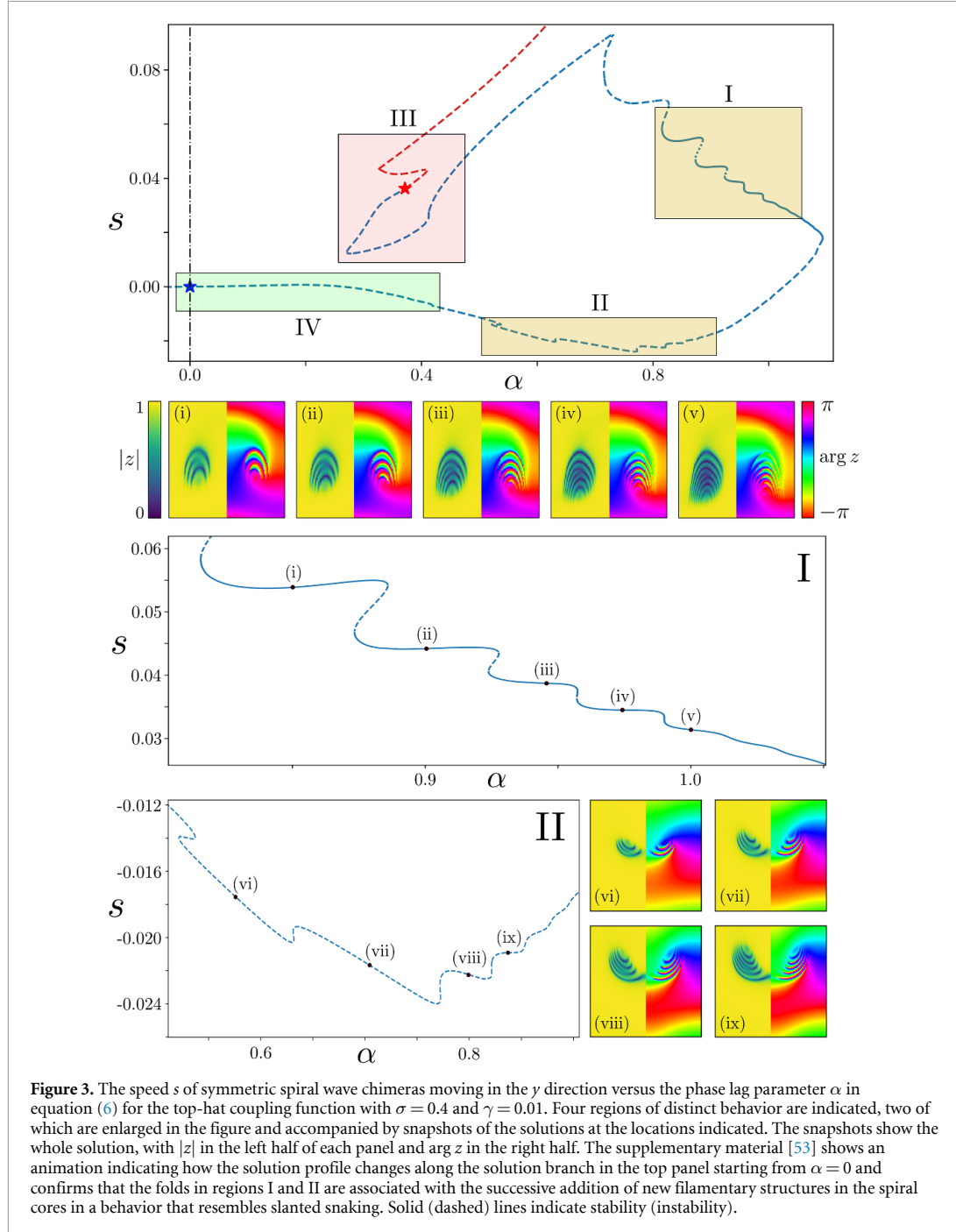
$$z(x, y, t) = a(x - st, y - st) e^{i\Omega t} \quad (9)$$

with $s \in \mathbb{R}$ and $a(y, x) = a(x, y)$ (hereafter \tilde{Z}_2 symmetry), corresponding to uniform motion along a diagonal. We refer to these solutions as *symmetric* spiral waves but distinguish them by their symmetries Z_2 and \tilde{Z}_2 under reflection. Note that rotations by 90° rotate a Z_2 -symmetric state into another Z_2 -symmetric state, and similarly for \tilde{Z}_2 -symmetric states.

2.1. Top-hat coupling function

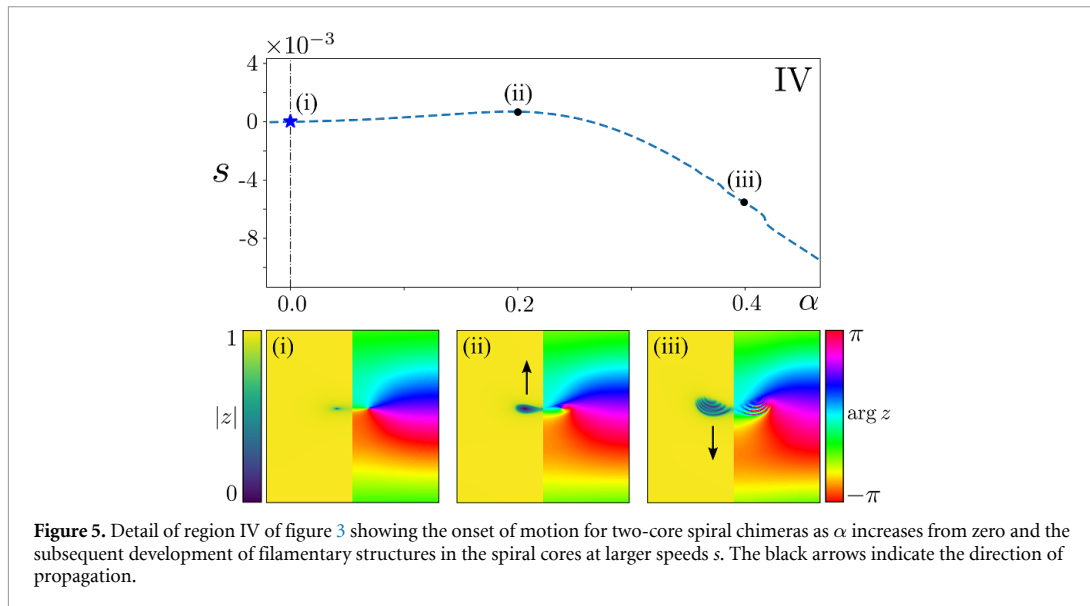
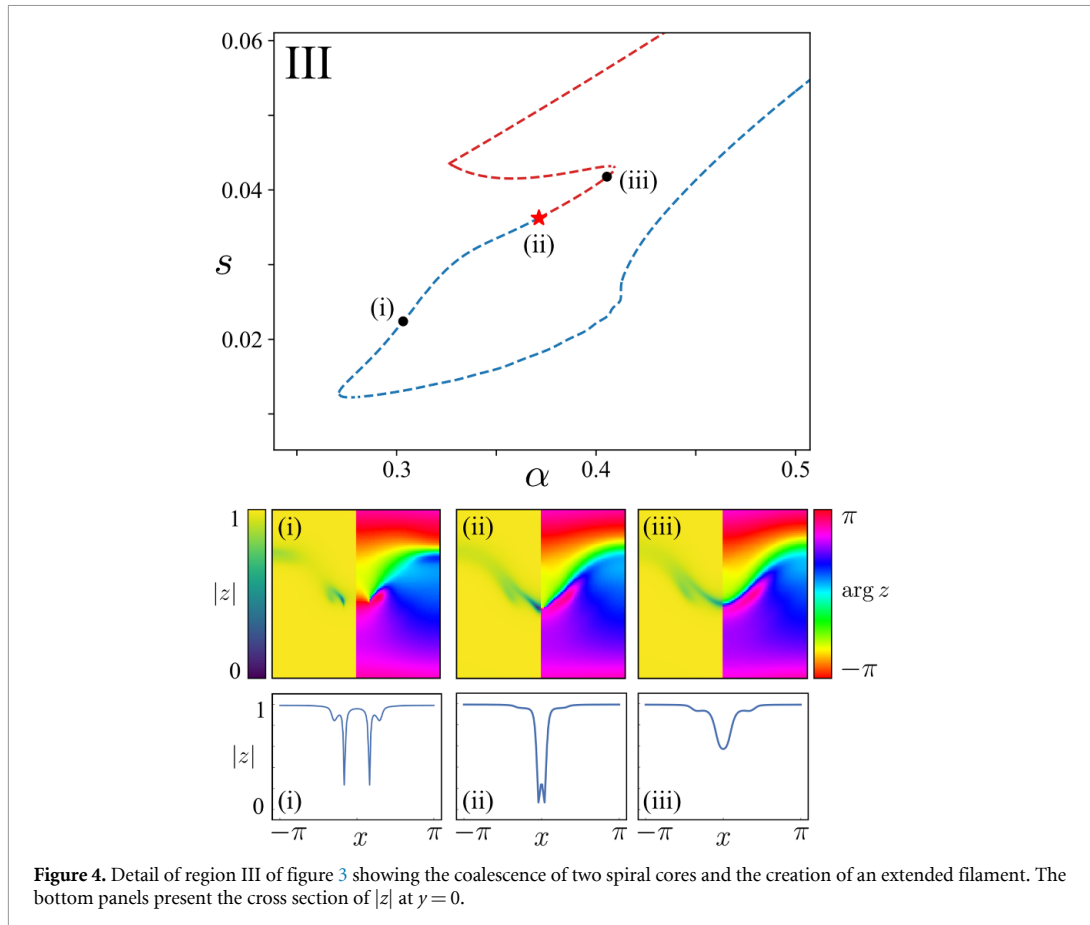
The bifurcation diagram for Z_2 -symmetric spiral wave chimeras (8) with the top-hat coupling function (5) with $\sigma = 0.4$ is shown in figure 3. The diagram shows the speed s as a function of the phase lag parameter α , obtained by inserting ansatz (8) into equation (6), discretizing the resulting equation on a square grid with 128 nodes in x and y directions and using an arc-length continuation scheme and a standard Newton solver to follow the branch of equilibria of the resulting system of 128×64 nonlinear equations. (Note that owing to the reflection symmetry of $a(x, y)$, the number of equations is reduced by half.) This procedure allows us to compute both stable and unstable solutions; in all cases, the predictions of this approach were confirmed using direct numerical simulations of the discrete system (1).

Figure 3 identifies four key regions in this diagram with different behavior. Enlargements of regions I and II are included in the figure together with solution snapshots at the locations labeled in the bifurcation diagram. These depict $|z|$ in the left half of each panel and $\arg z$ in the right half and show that the sequence of folds in regions I and II is associated with an increasing number of filamentary structures in the spiral

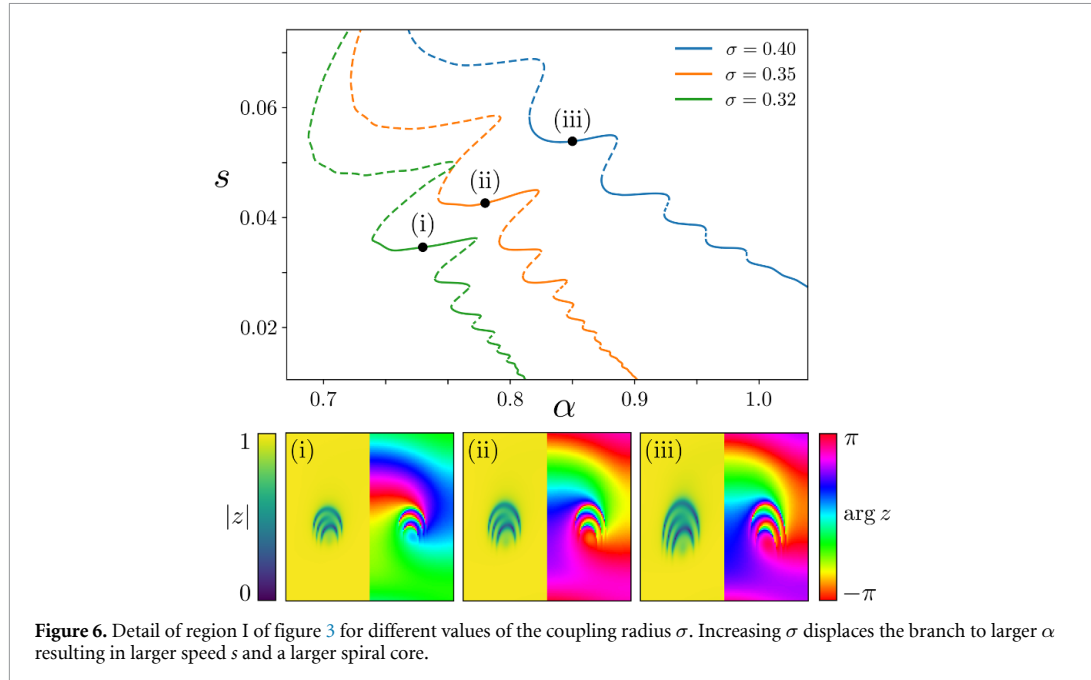


cores as α increases. In both regions the bifurcation diagram resembles slanted snaking [48–52]. As discussed below, these filamentary structures are a consequence of the two-frequency nature of the traveling chimera state: its global oscillation frequency Ω and its translation frequency determined by the speed s .

Figures 4 and 5 show the corresponding behavior in regions III and IV. The former shows the gradual approach of the two cores to one another along the branch, resulting in the presence of filaments that extend across the whole domain beyond the location indicated by the red star, while the latter shows the gradual onset of the translation motion from $\alpha = 0$ until $\alpha = 0.4$ where the speed s is large enough for prominent filaments to be present in the spiral cores. Finally, figure 6 shows the effects of decreasing the top-hat radius σ on the behavior in region I. We observe that as σ decreases so does the corresponding value of α resulting in smaller speed s and a smaller spiral core, all for a given number of core filaments. Overall, however, the behavior remains qualitatively unchanged.



We remark that even with a relatively small number of discretization points the time needed to calculate the diagram shown in figure 3 turned out to be extremely long (ca. 6 weeks on a dedicated computer with large RAM). In contrast, the results we are going to describe in the next section were obtained much more rapidly (ca. 3–4 days on a laptop with a double number of discretization points in each direction). This remarkable computational speed-up was achieved thanks to the use of a special analytical technique for



calculating periodic orbits in the Ott–Antonsen manifold proposed in [56] by one of the authors of this paper.

2.2. Trigonometric coupling function

The results for the top-hat coupling function (5) illustrate some of the complexities inherent in the present problem. Since our ultimate goal is to understand the properties of spiral wave chimeras in the case of general coupling functions $G(x, y)$, we need a deeper analytical approach to this problem. This becomes possible if we limit ourselves to a narrower class of D_4 -symmetric functions of the form

$$G(x, y) = \frac{1}{(2\pi)^2} (1 + A(\cos x + \cos y) + B \cos x \cos y), \quad (10)$$

where A and B are real parameters such that $A^2 + B^2 \neq 0$. This expression arises as a truncation of a Fourier series representation of the coupling function $G(x, y)$, assumed to be an absolutely integrable 2π -periodic function:

$$G(x, y) = \sum_{n,m=-\infty}^{\infty} \hat{g}_{nm} e^{i(nx+my)}, \quad (11)$$

where

$$\hat{g}_{nm} = \frac{1}{(2\pi)^2} \int_{-\pi}^{\pi} \int_{-\pi}^{\pi} G(x, y) e^{-i(nx+my)} dx dy.$$

Moreover, if this function satisfies (4), then

$$\hat{g}_{-n,m} = \hat{g}_{n,-m} = \hat{g}_{-n,-m} = \hat{g}_{n,m}.$$

In addition, if its integral is normalized to the identity,

$$\int_{-\pi}^{\pi} \int_{-\pi}^{\pi} G(x, y) dx dy = 1,$$

then $\hat{g}_{0,0} = 1/(2\pi)^2$. The simplest non-constant truncation of (11) is obtained on keeping terms with indices $n, m = 0, \pm 1$ only, leading to (10) with

$$A = 8\pi^2 \hat{g}_{1,0}, \quad B = 16\pi^2 \hat{g}_{1,1}.$$

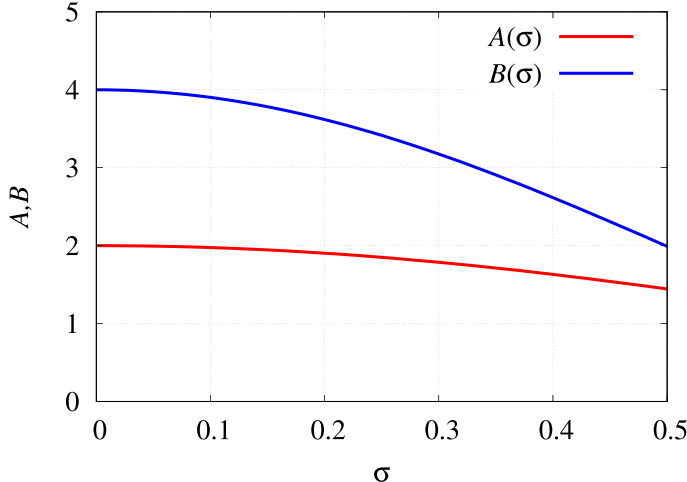


Figure 7. The parameters A and B in equation (10) corresponding to the leading order Fourier approximation to the top-hat coupling function (5) with different σ .

For example, if we calculate the Fourier coefficients $\hat{g}_{1,0}$ and $\hat{g}_{1,1}$ of the top-hat coupling function (5) and insert them in the above formulas, we obtain the fit $\sigma \mapsto (A(\sigma), B(\sigma))$ shown in figure 7.

In the following we study the resulting spiral chimeras as a function of the coefficients A and B in the relevant range revealed by figure 7, together with their stability properties, starting with stationary two-core chimeras for $\alpha = 0$. The damping parameter γ is fixed at $\gamma = 0.01$.

2.3. Static patterns

For $\alpha = 0$ equation (6) is variational and all chimera states are therefore time-independent and motionless, and correspond to equilibria of the form

$$z(x, y, t) = a(x, y).$$

In section 3.1 below, we construct the self-consistency equation determining these equilibria and explain how we solve it. In addition, we describe how the linear stability analysis of such equilibria can be performed. Using these mathematical tools, we calculate bifurcation diagrams for various values of the coupling parameters A and B . Specifically, we show that all static solutions of equation (6) with the coupling function (10) and $\alpha = 0$, including two-core chimeras, have the form

$$a(x, y) = \frac{w(x, y)}{\gamma + \sqrt{\gamma^2 + |w(x, y)|^2}}, \quad (12)$$

where

$$w(x, y) \in \text{Span} \{1, \cos x, \cos y, \sin x, \sin y, \cos x \cos y, \cos x \sin y, \sin x \cos y, \sin x \sin y\}.$$

Patterns with symmetry under the reflection $x \rightarrow -x$, i.e. with $a(-x, y) = a(x, y)$, are Z_2 -symmetric, and are described by a subset of the admissible functions $w(x, y)$, namely

$$w(x, y) \in \text{Span} \{1, \cos x, \cos y, \sin y, \cos x \cos y, \cos x \sin y\},$$

while patterns satisfying $a(y, x) = a(x, y)$, i.e. with reflection symmetry in the diagonal, are \tilde{Z}_2 -symmetric, and are described by functions $w(x, y)$ of the form

$$w(x, y) \in \text{Span} \{1, \cos x + \cos y, \sin x + \sin y, \cos x \cos y, \sin x \sin y\}.$$

Among these states we distinguish between *fundamental* states that are independent of the parameter B in (10), and *compound* states that depend on B . The former include the following:

- (a) Completely incoherent state

$$a(x, y) = 0.$$

(b) Partially coherent uniform state

$$a(x,y) = \sqrt{1 - 2\gamma}, \quad \gamma < 1/2.$$

(c) Partially coherent splay state

$$a(x,y) = q e^{iy}, \quad q \in (0,1).$$

(d) Generalized antiphase state

$$a(x,y) = \frac{p + iq \sin y}{\gamma + \sqrt{\gamma^2 + p^2 + q^2 \sin^2 y}}, \quad p \geq 0, q > 0,$$

called an antiphase state when $p = 0$.

(e) Planar state

$$a(x,y) = \frac{p + r \cos y + iq \sin y}{\gamma + \sqrt{\gamma^2 + (p + r \cos y)^2 + q^2 \sin^2 y}}$$

with $p, r, q > 0$.

(f) Four-core spiral pattern

$$a(x,y) = \frac{q(\cos x + i \sin y)}{\gamma + \sqrt{\gamma^2 + q^2 (\cos^2 x + \sin^2 y)}}, \quad q > 0.$$

(g) Generalized four-core spiral pattern

$$a(x,y) = \frac{p \cos x + r \cos y + iq \sin y}{\gamma + \sqrt{\gamma^2 + (p \cos x + r \cos y)^2 + q^2 \sin^2 y}}$$

with $p, r, q > 0$.

The above states are all Z_2 -symmetric, but similar expressions can be written for fundamental \tilde{Z}_2 -symmetric states. This is a consequence of the following.

2.3.1. Equivalence of the cases $A = 0$ and $B = 0$

From the identity

$$\frac{1}{(2\pi)^2} (1 + B \cos x \cos y) = \frac{1}{(2\pi)^2} \left(1 + \frac{B}{2} (\cos(x-y) + \cos(x+y)) \right)$$

it follows that every pattern observed for $(A, B) = (A_0, 0)$ has its counterpart rotated by the angle $\pi/4$ and observed for $(A, B) = (0, 2A_0)$. Therefore, the dynamics of equation (6) in the case $A = 0$ and in the case $B = 0$ are identical modulo the above spatial rotation and rescaling. This result is independent of the value of the phase lag parameter α .

2.4. Bifurcation diagrams for static patterns

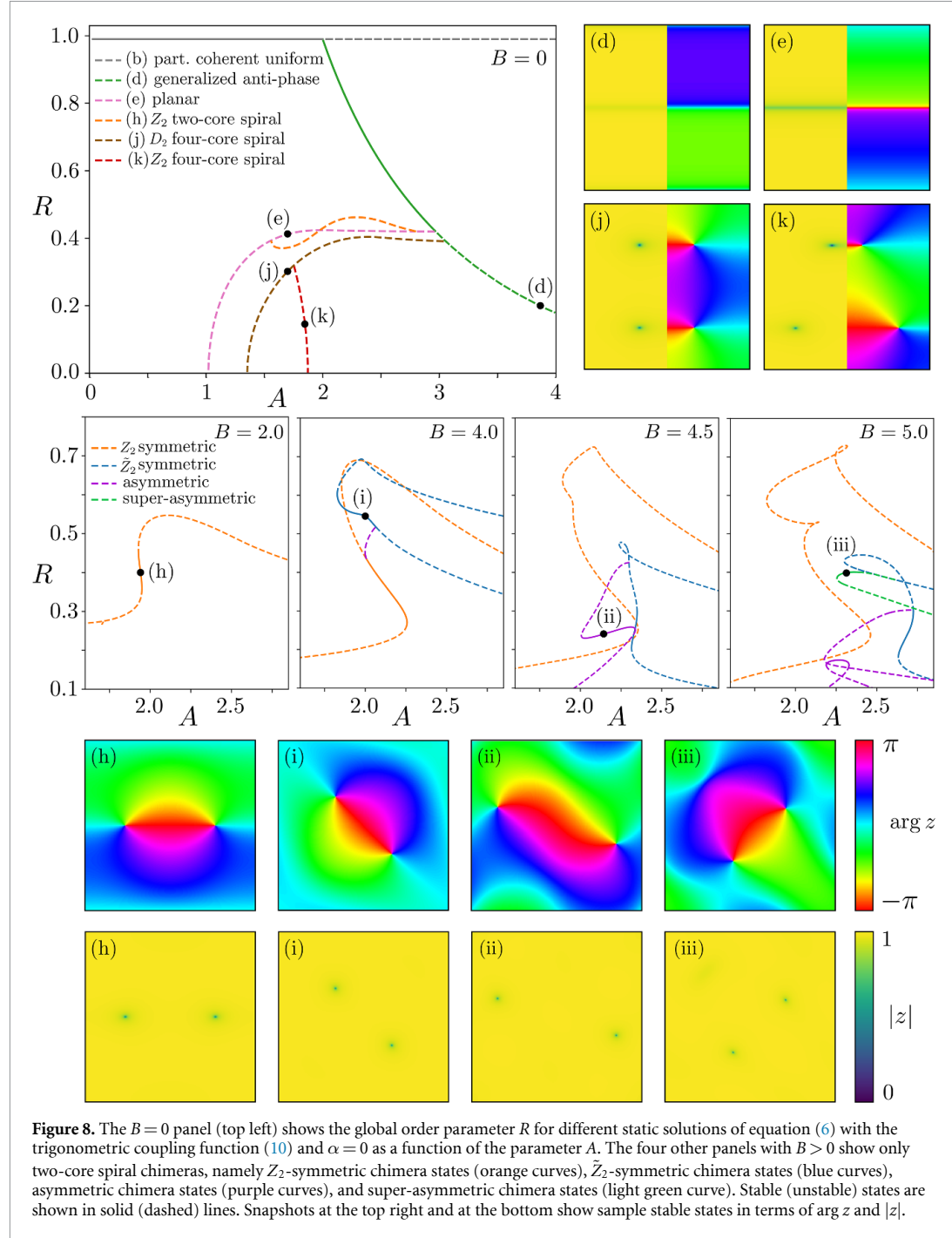
Thanks to the simplicity of the above formulas, the existence and stability properties of the completely incoherent state, the partially coherent uniform state and the partially coherent splay state can be described comprehensively. In particular, in section 3.1 we show that:

- (i) the completely incoherent state is linearly stable if $\gamma \geq \max(1/2, A/4, B/8)$ and unstable otherwise,
- (ii) the partially coherent uniform state exists only for $\gamma < 1/2$ and is linearly stable if $A \leq 2$ and $B \leq 4$ and unstable otherwise.

The stability analysis of the partially coherent splay state can be performed by generalizing the analytical scheme proposed in [35, 57]; the stability analysis for four-core spiral patterns in the case $B = 0$ was performed in [31, 36].

To display our results, including stability results, we employ the global order parameter

$$R \equiv \frac{1}{(2\pi)^2} \left| \int_{-\pi}^{\pi} \int_{-\pi}^{\pi} a(x,y) dx dy \right|. \quad (13)$$



However, a number of the states listed above have the same global order parameter, $R=0$, as the completely incoherent state. To distinguish among these states, we introduce the quantity

$$S = \frac{1}{(2\pi)^2} \left| \int_{-\pi}^{\pi} \int_{-\pi}^{\pi} a(x,y) \sin y \, dx \, dy \right| \quad (14)$$

measuring the contribution of $\sin y$ in the Fourier expansion of $a(x,y)$.

Figure 8, top panel, shows the global order parameter R for static states computed from equation (6) for different values of the parameter A in equation (10) when $B=0$, $\alpha=0$. We observe:

- (i) $B=0$: the partially coherent uniform state $R=\sqrt{1-2\gamma}$ (gray line, state (b)) becomes unstable through a pitchfork of revolution at $A=2$. This bifurcation gives rise to fundamental Z_2 -symmetric states

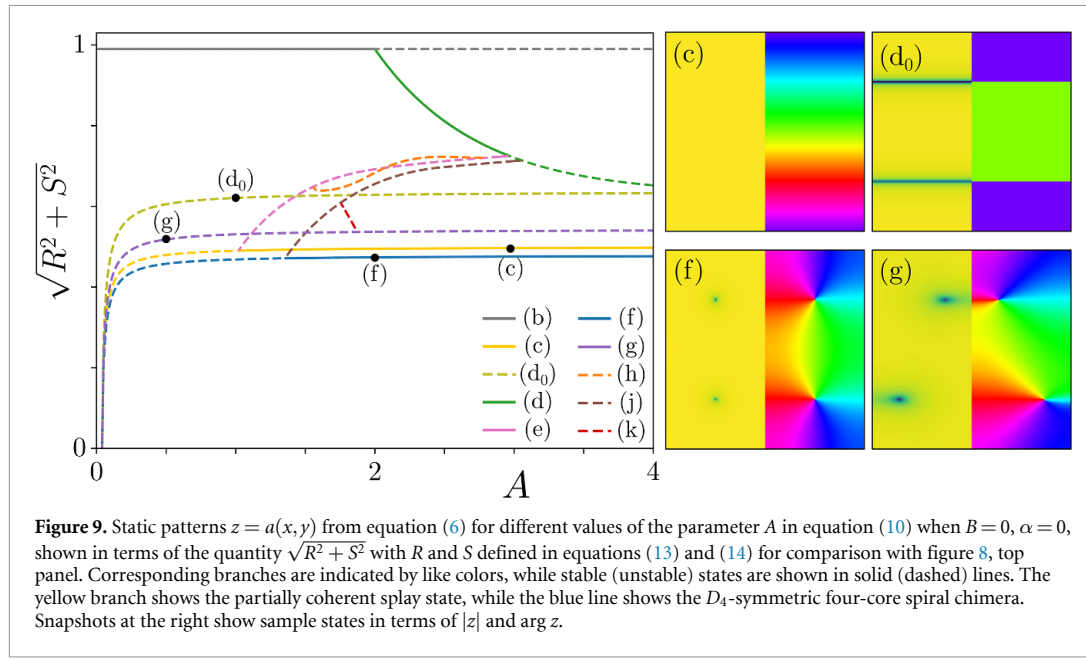


Figure 9. Static patterns $z = a(x, y)$ from equation (6) for different values of the parameter A in equation (10) when $B = 0$, $\alpha = 0$, shown in terms of the quantity $\sqrt{R^2 + S^2}$ with R and S defined in equations (13) and (14) for comparison with figure 8, top panel. Corresponding branches are indicated by like colors, while stable (unstable) states are shown in solid (dashed) lines. The yellow branch shows the partially coherent splay state, while the blue line shows the D_4 -symmetric four-core spiral chimera. Snapshots at the right show sample states in terms of $|z|$ and $\arg z$.

(green curve, state (d)). For this state $|a(x, y)|$ has period π in the y direction. These states lose stability at a secondary pitchfork bifurcation creating a branch of fundamental Z_2 -symmetric solutions with period 2π in $|a(x, y)|$ in the y direction (pink curve, state (e)). This new arc-shaped branch in figure 8(a) is everywhere unstable and connects the green branch of period π states with the branch of partially coherent splay states with $R = 0$.

Along the pink branch of period 2π states there are two tertiary pitchfork bifurcation points, with a S-shaped branch of Z_2 -symmetric states modulated in both x and y directions in between (orange curve, state (h)). These states correspond to stationary compound Z_2 -symmetric two-core spiral chimeras and so depend on the parameter B . At $B = 0$ these states are all unstable (dashed orange curve).

On the dashed brown branch we find unstable compound $D_2 = Z_2^2$ -symmetric four-core chimeras (state (j)) described by the formula (12) with $w(x, y) \in \text{Span}\{1, \cos x, \sin y, \cos x \sin y\}$. This branch connects the period π fundamental states with the fundamental D_4 -symmetric four-core chimeras with $R = 0$. A tertiary branch of unstable compound states (dashed red curve, state (k)) bifurcates from the brown branch.

- (ii) $B = 0$: to distinguish between the different states with $R = 0$ we show in figure 9 the same bifurcation diagram but showing the quantity $\sqrt{R^2 + S^2}$ as a function of A instead of R . In this figure, the yellow line shows the partially coherent splay states (state (c)), while the blue line corresponds to D_4 -symmetric four-core spiral chimeras (state (f)). We see that each of these states bifurcates from the completely incoherent state $a(x, y) = 0$ at $A = 4\gamma$ and loses stability with decreasing A in subcritical bifurcations, generating unstable states with $R > 0$. Moreover, two other unstable fundamental branches, a branch of anti-phase states (light green curve, state (d₀)) and a branch of generalized four-core patterns (dark purple curve, state (g)) also emerge at the same parameter value, $A = 4\gamma$, indicating the highly degenerate nature of this point.
- (iii) $B > 0$: figure 8 shows how the behavior of the compound states changes with the coefficient B in the coupling function. The figure shows that while the fundamental Z_2 -symmetric solution is independent of B its stability may change as B changes. A similar statement applies to fundamental \tilde{Z}_2 -symmetric solutions. The stability of tertiary states may likewise change. In particular, at $B = 2$, there appears a narrow parameter range $A \approx (1.93, 1.95)$ with stable Z_2 -symmetric two-core spiral chimeras. This range corresponds to the segment of the orange solution branch with negative slope.
- (iv) At $B = 4$, the segment of the orange branch with negative slope is broader but the stability range of Z_2 -symmetric spiral chimeras is limited by a (subcritical) quaternary bifurcation to (unstable) asymmetric two-core states (purple branch) that connect the states with Z_2 symmetry to similar states with \tilde{Z}_2 symmetry (blue branch, state (i)). By asymmetric we mean any state that is neither Z_2 - nor

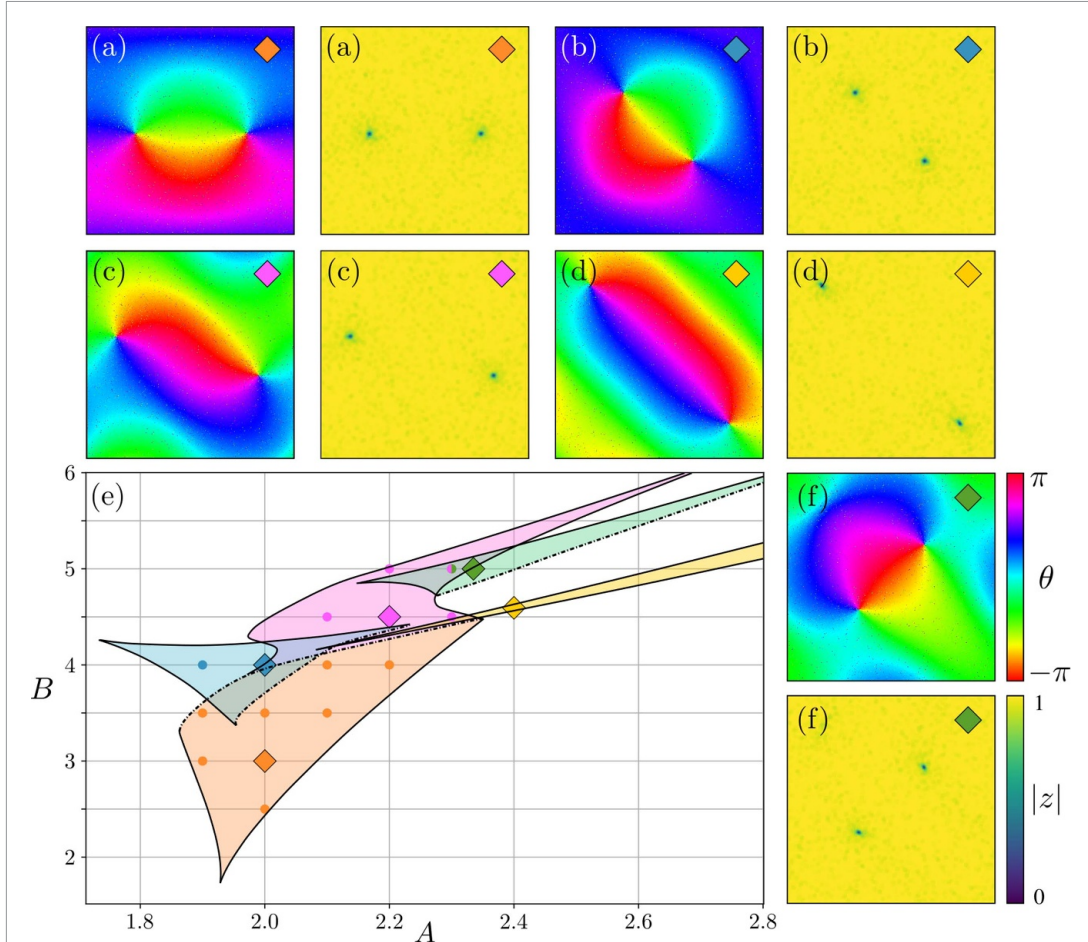


Figure 10. The (A, B) parameter plane (panel (e)) showing regions of stable (shaded) static spiral wave chimeras from the Ott–Antonsen equation (6) with $\alpha = 0$ together with solution snapshots corresponding to the color-coded diamond symbols, showing the phase θ and modulus $|z|$ of the complex order parameter z . Filled circles indicate the parameters of stable spiral wave chimeras found in direct numerical simulations of equation (3) with $N = 512$. The solid and dash-dotted stability boundaries correspond to fold and pitchfork bifurcations, respectively. (a) Z_2 -symmetric chimera, (b) \tilde{Z}_2 -symmetric chimera, (c) Z_2 -asymmetric chimera, (d) \tilde{Z}_2 -symmetric chimera and (f) \tilde{Z}_2 -asymmetric (super-asymmetric) chimera. Profiles (b) and (d) correspond to different stability intervals on the same solution branch (see blue branch in figure 8).

\tilde{Z}_2 -symmetric. Stability calculation points to a narrow region of bistability between the Z_2 - and \tilde{Z}_2 -symmetric states. Stable asymmetric states are present at larger values of B (purple branch, state (ii)).

- (v) At $B = 5$, the Z_2 -symmetric spiral chimeras are unstable, but \tilde{Z}_2 -symmetric spiral chimeras can still be stable in a certain parameter range (blue branch, state (i)). A branch of \tilde{Z}_2 -asymmetric spiral chimeras (light green branch, state (iii)) bifurcates from the \tilde{Z}_2 -symmetric spiral chimeras and some of these may also be stable. We call the resulting states super-asymmetric to distinguish them from the other states previously called asymmetric. The reason for this terminology is the following. Every Z_2 - or \tilde{Z}_2 -symmetric state as well as every asymmetric state is represented by expression (12) with an appropriate function $w(x, y)$ in the nine-dimensional manifold determined by expressions (22) and (25) from section 3.1. In contrast, for super-asymmetric states such a representation is not possible. In this case, the corresponding function $w(x, y)$ is still given by (22) but with fully complex coefficients, except for those in the pinning conditions (24).

For every static two-core spiral chimera shown in figure 8 we performed continuation of its stability boundaries. As a result, we identified five partly overlapping stability regions in the (A, B) plane shown in figure 10. Each of these regions is bounded by two fold bifurcation curves (solid lines) and one pitchfork bifurcation curve (dash-dotted line).

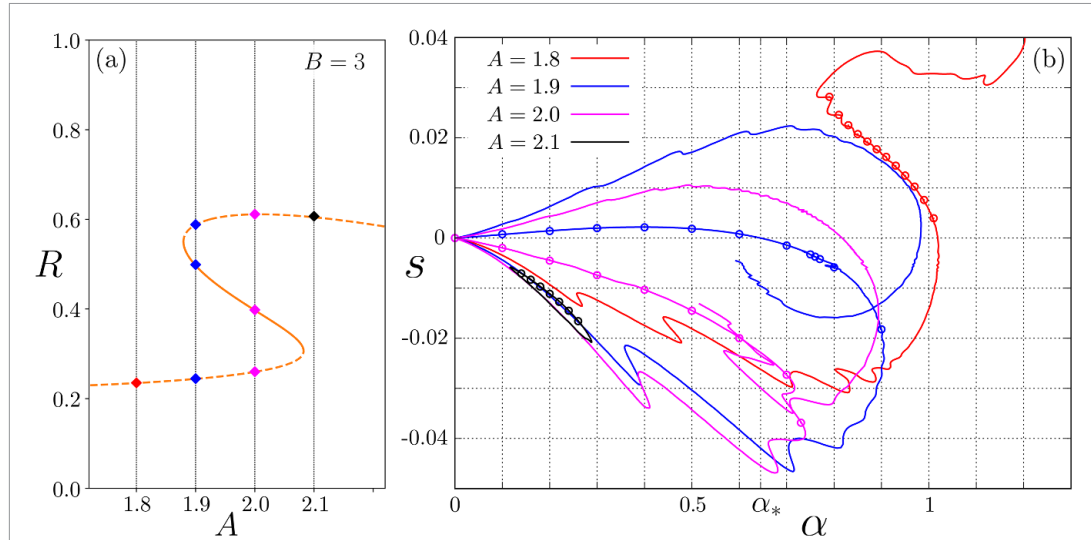


Figure 11. (a) The global order parameter R of Z_2 -symmetric two-core spiral wave chimeras versus the parameter A of the trigonometric coupling function (10) when $B = 3$ and $\alpha = 0$. (b) The speed s of symmetric spiral wave chimeras moving in the y direction versus the phase lag parameter α computed from equation (6) with the trigonometric coupling function (10) with four different values A (color-coded) and $B = 3$. Open circles indicate the speed of stable spiral wave chimeras found in direct numerical simulations of equation (3) with the same coupling function (10) and $N = 512$.

2.5. Moving spiral wave chimeras

Moving spiral wave chimeras are observed in the non-variational case, i.e. for $\alpha \neq 0$. To continue such states in parameter space we used a numerical method based on the self-consistency equation from section 3.2 together with a non-iterative algorithm for calculating periodic orbits in the Ott–Antonsen manifold [56]. To describe typical bifurcation diagrams as the phase lag α changes, we consider the case $B = 3$. Figure 11(a) shows a diagram analogous to figure 8 that indicates that for $A = 2$ and $\alpha = 0$ there are three coexisting motionless Z_2 -symmetric two-core spiral wave chimeras (pink diamonds). Only one, the one with an intermediate value of R , is stable. When α increases each of these spiral patterns persists as a moving spiral wave chimera and its stability remains unchanged for small α (pink curves in figure 11(b)). For larger α the dependence of the speed s on α becomes nonlinear (figure 11(b)) and the bottom and intermediate branches annihilate in a fold point at $\alpha \approx 0.74$ while the upper, $s > 0$ branch continues beyond this point.

If we take $A = 2.1$ the upper, $s > 0$ branch continues to exist (not shown) while a loop composed of the two $s < 0$ branches detaches from $\alpha = 0$ (black curves) but stable solutions continue to exist on the upper portion of the resulting isola. This loop shrinks rapidly with increasing A and disappears by $A = 2.2$, thereby eliminating stable two-core spiral chimera states.

A qualitatively different scenario occurs if we decrease the parameter A . For $A = 1.9$ the middle branch now corresponds to $s > 0$ forming part of a looped branch that grows in size and intersects the horizontal axis at some $\alpha_* \approx 0.645$ (blue curves). Thus the spiral wave chimeras travel in opposite directions for $\alpha < \alpha_*$ and $\alpha > \alpha_*$.

In contrast, for $A = 1.8$ and $\alpha = 0$ the remaining two-core spiral wave chimera (figure 11(a)) results in moving states with $s < 0$ (red curve in figure 11(b)) with the two upper branches detached from $\alpha = 0$ forming an S-shaped curve whose intermediate section corresponds to numerically stable two-core spiral wave chimeras. Snapshots of the solutions along this branch (figure 12) show that with increasing $|s|$ the incoherent regions around the phase defects develop internal structure in the form of crescent-shaped filaments. Along the bottom part of the branch, the development of each new filament corresponds to an S-shaped fold in the solution branch in the (α, s) plane reminiscent of slanted snaking of spatially localized states [48–52]. However, in other cases, especially when the number of filaments is large (more than 10 or so) or s is close to zero, the speed s evolves monotonically with α in a manner reminiscent of *smooth* snaking [51]. Both behaviors are characteristic of nonlocal systems.

Note that the shape of the solution branch for $A = 1.8$ resembles qualitatively the behavior of the solution curve in figure 3 calculated for the top-hat coupling function. Moreover, the changes in the profiles $a(x, y)$ along the curve are also reminiscent of those shown in figure 3.

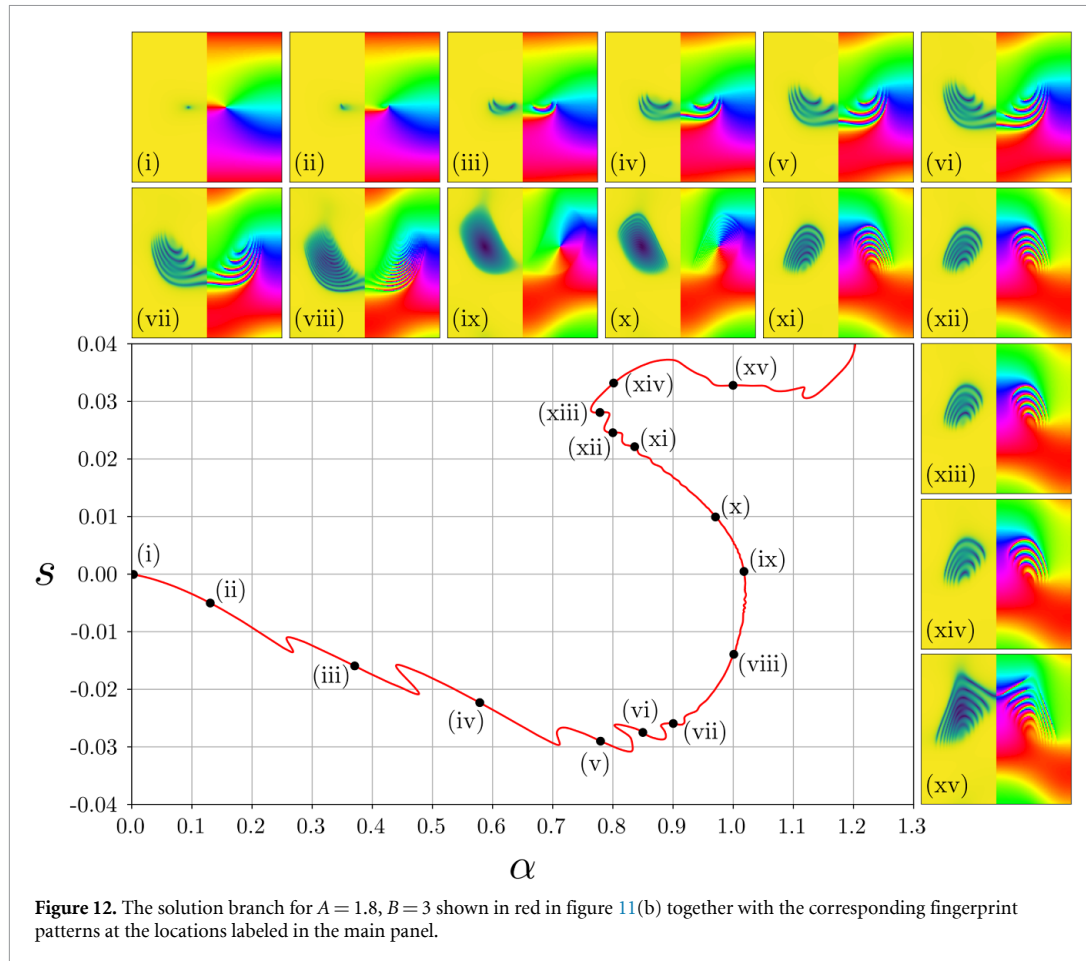


Figure 12. The solution branch for $A = 1.8$, $B = 3$ shown in red in figure 11(b) together with the corresponding fingerprint patterns at the locations labeled in the main panel.

3. Methods

3.1. Static patterns for equation (6) with $\alpha = 0$

In the case $\alpha = 0$, equation (6) is variational and its long-term dynamics therefore correspond to static patterns or equilibria of the form

$$z(x, y, t) = a(x, y). \quad (15)$$

All two-core spiral wave solutions of equation (6) shown in figure 8 have this form. Below we describe the mathematical methods used to carry out continuation and stability analysis of these states. For this, we adapt the techniques from [36, 45].

3.1.1. Self-consistency equation

Inserting ansatz (15) into equation (6) we obtain

$$0 = -\gamma a + \frac{1}{2} \mathcal{G}a - \frac{1}{2} a^2 \mathcal{G}\bar{a}$$

or equivalently

$$\bar{w}(x, y) a^2 + 2\gamma a - w(x, y) = 0, \quad (16)$$

where

$$w(x, y) = (\mathcal{G}a)(x, y). \quad (17)$$

Solving equation (16) for a and choosing the square root branch that ensures the inequality $|a| \leq 1$, we obtain

$$\begin{aligned} a(x,y) &= \frac{-\gamma + \sqrt{\gamma^2 + |w(x,y)|^2}}{\bar{w}(x,y)} \\ &= \frac{w(x,y)}{\gamma + \sqrt{\gamma^2 + |w(x,y)|^2}}. \end{aligned} \quad (18)$$

Expressions (17) and (18) agree with one another iff the function $w(x,y)$ satisfies the self-consistency equation

$$w(x,y) = \int_{-\pi}^{\pi} \int_{-\pi}^{\pi} G(x-x',y-y') H_{\gamma}(w(x',y')) dx' dy', \quad (19)$$

where

$$H_{\gamma}(w) = \frac{w}{\gamma + \sqrt{\gamma^2 + |w|^2}}.$$

3.1.2. Reduced self-consistency equation

Let us consider equation (19) in the case of the trigonometric coupling function (10). First, we define an inner product on the space $C([- \pi, \pi]; \mathbb{C})$,

$$\langle u, v \rangle = \frac{1}{(2\pi)^2} \int_{-\pi}^{\pi} \int_{-\pi}^{\pi} u(x,y) \bar{v}(x,y) dx dy.$$

Then, it is easy to see that for the trigonometric coupling function (10) we have

$$(\mathcal{G}u)(x,y) = \sum_{k=1}^9 \xi_k \langle u, \psi_k \rangle \psi_k(x,y),$$

where

$$\begin{aligned} \psi_1(x,y) &= 1, & \psi_2(x,y) &= \cos x, & \psi_3(x,y) &= \cos y, \\ \psi_4(x,y) &= \sin y, & \psi_5(x,y) &= \cos x \cos y, & \psi_6(x,y) &= \cos x \sin y, \\ \psi_7(x,y) &= \sin x, & \psi_8(x,y) &= \sin x \cos y, & \psi_9(x,y) &= \sin x \sin y, \end{aligned}$$

and

$$\xi_k = \begin{cases} 1 & \text{for } k = 1, \\ A & \text{for } k = 2, 3, 4, 7, \\ B & \text{for } k = 5, 6, 8, 9. \end{cases} \quad (20)$$

Note that the functions $\psi_k(x,y)$ are mutually orthogonal with respect to the inner product $\langle \cdot, \cdot \rangle$. Moreover,

$$\langle \psi_n, \psi_n \rangle = \begin{cases} 1 & \text{for } n = 1, \\ 1/2 & \text{for } n = 2, 3, 4, 7, \\ 1/4 & \text{for } n = 5, 6, 8, 9. \end{cases} \quad (21)$$

Owing to the finite-rank nature of the resulting integral operator \mathcal{G} every solution of the self-consistency equation (19) can be written in the form

$$w(x,y) = \sum_{k=1}^9 \hat{w}_k \psi_k(x,y) \quad (22)$$

with complex coefficients \hat{w}_k . Inserting (22) into equation (19) and equating similar terms on the left and right sides, we obtain the finite-dimensional system

$$\hat{w}_j = \xi_j \left\langle H_{\gamma} \left(\sum_{k=1}^9 \hat{w}_k \psi_k \right), \psi_j \right\rangle, \quad j = 1, \dots, 9. \quad (23)$$

The system (23) inherits the three continuous symmetries of equation (19). Therefore a unique solution requires that we impose three *pinning conditions*, for example

$$\hat{w}_1 = |\hat{w}_1|, \quad \hat{w}_4 = i|\hat{w}_4|, \quad \hat{w}_7 = i|\hat{w}_7|. \quad (24)$$

Note that owing to the first pinning condition the value of \hat{w}_1 always coincides with the global order parameter R defined in equation (13).

It turns out that the vast majority of stable static solutions of equation (6) with the coupling function (10) and in particular almost all the patterns shown in figure 8 are represented by solutions of the system (23) and (24) on the invariant manifold determined by the identities

$$\begin{cases} \operatorname{Im} \hat{w}_k = 0 & \text{for } k = 1, 2, 3, 5, 9, \\ \operatorname{Re} \hat{w}_k = 0 & \text{for } k = 4, 6, 7, 8. \end{cases} \quad (25)$$

The invariance of this manifold follows from the fact that the basis functions ψ_k with $k = 1, 2, 3, 5, 9$ have the reflection symmetry

$$\psi_k(-x, -y) = \psi_k(x, y),$$

while the remaining four functions with $k = 4, 6, 7, 8$ satisfy the antisymmetric relation

$$\psi_k(-x, -y) = -\psi_k(x, y).$$

The restriction of the system (23), (24) to the manifold (25) almost halves the dimensionality of the system and allows a significant speed-up of its solution.

We may further reduce the dimensionality of the system (23), (24) by looking for Z_2 -symmetric solutions of equation (19). Such solutions satisfy the relation $w(-x, y) = w(x, y)$, so we must assume $\hat{w}_7 = \hat{w}_8 = \hat{w}_9 = 0$. The resulting six equations require only the first two pinning conditions in (24) in order to obtain a unique solution. A similar approach applies to \tilde{Z}_2 -symmetric solutions as well.

3.1.3. Initial conditions for system (23)

To apply a Newton solver to system (23) we need to have a good initial guess. In addition, it is desirable that this guess satisfies the pinning conditions (24). We perform this task as follows.

We run the numerical simulations for the oscillator system (3) with the coupling function (10) until it approaches a stationary state of interest. Using the last snapshot of the phases θ_{jk} , we calculate a discrete analog of formula (17),

$$W_{jk} = \left(\frac{2\pi}{N} \right)^2 \sum_{m,n=1}^N G \left(\frac{2\pi(j-m)}{N}, \frac{2\pi(k-n)}{N} \right) e^{i\theta_{mn}},$$

where the complex exponent $e^{i\theta_{mn}}$ appears instead of $z(-\pi + 2\pi m/N, -\pi + 2\pi n/N)$. Next, using the discrete Fourier transform, we calculate the necessary Fourier coefficients \hat{w}_k .

These coefficients do not, in general, satisfy the pinning conditions (24). To impose the pinning condition on \hat{w}_1 , we apply a transformation

$$\hat{w}_k \mapsto \hat{w}_k \frac{\overline{\hat{w}_1}}{|\hat{w}_1|}, \quad k = 1, 2, \dots, 9.$$

Next, we perform a transformation that ensures the pinning condition for \hat{w}_4

$$\begin{aligned} \hat{w}_3 &\mapsto \hat{w}_3 \cos y_0 - \hat{w}_4 \sin y_0, \\ \hat{w}_4 &\mapsto \hat{w}_3 \sin y_0 + \hat{w}_4 \cos y_0, \\ \hat{w}_5 &\mapsto \hat{w}_5 \cos y_0 - \hat{w}_6 \sin y_0, \\ \hat{w}_6 &\mapsto \hat{w}_5 \sin y_0 + \hat{w}_6 \cos y_0, \\ \hat{w}_8 &\mapsto \hat{w}_8 \cos y_0 - \hat{w}_9 \sin y_0, \\ \hat{w}_9 &\mapsto \hat{w}_8 \sin y_0 + \hat{w}_9 \cos y_0, \end{aligned}$$

where

$$e^{iy_0} = \pm \frac{\operatorname{Re}(\hat{w}_3) - i\operatorname{Re}(\hat{w}_4)}{\sqrt{[\operatorname{Re}(\hat{w}_3)]^2 + [\operatorname{Re}(\hat{w}_4)]^2}}$$

and from the two signs in the last formula, the one that makes the imaginary part of \hat{w}_4 positive is chosen. Finally, we perform a third transformation,

$$\begin{aligned}\hat{w}_2 &\mapsto \hat{w}_2 \cos x_0 - \hat{w}_7 \sin x_0, \\ \hat{w}_7 &\mapsto \hat{w}_2 \sin x_0 + \hat{w}_7 \cos x_0, \\ \hat{w}_5 &\mapsto \hat{w}_5 \cos x_0 - \hat{w}_8 \sin x_0, \\ \hat{w}_8 &\mapsto \hat{w}_5 \sin x_0 + \hat{w}_8 \cos x_0, \\ \hat{w}_6 &\mapsto \hat{w}_6 \cos x_0 - \hat{w}_9 \sin x_0, \\ \hat{w}_9 &\mapsto \hat{w}_6 \sin x_0 + \hat{w}_9 \cos x_0,\end{aligned}$$

where

$$e^{ix_0} = \pm \frac{\operatorname{Re}(\hat{w}_2) - i\operatorname{Im}(\hat{w}_7)}{\sqrt{[\operatorname{Re}(\hat{w}_2)]^2 + [\operatorname{Im}(\hat{w}_7)]^2}}.$$

The sign in this expression is chosen such that the imaginary part of \hat{w}_7 positive. The resulting coefficients \hat{w}_k satisfy all the pinning conditions (24) *exactly*.

3.1.4. Stability analysis

To analyze the linear stability of the equilibria of equation (6), we proceed as follows. We insert the ansatz

$$z(x, y, t) = a(x, y) + v(x, y, t)$$

into the equation and linearize it with respect to the infinitesimal perturbation v . Thus

$$\frac{dv}{dt} = -\eta_0(x, y)v + \frac{1}{2}\mathcal{G}v - \frac{1}{2}a^2(x, y)\mathcal{G}\bar{v}, \quad (26)$$

where

$$\eta_0(x, y) = \gamma + a(x, y)\mathcal{G}\bar{a},$$

the subscript 0 on $\eta_0(x, y)$ indicating that we are considering a static pattern. Owing to (17) and (18), we have

$$\eta_0(x, y) = \sqrt{\gamma^2 + |w(x, y)|^2}, \quad (27)$$

implying that $\eta_0(x, y)$ is real and satisfies $|\eta_0(x, y)| \geq \gamma$.

The structure of equation (26) implies that the spectrum consists of two parts: the essential spectrum

$$\sigma_{\text{ess}} = \left\{ -\eta_0(x, y) : (x, y) \in [-\pi, \pi]^2 \right\} \subset \mathbb{R}$$

and the point spectrum σ_{pt} consisting of isolated eigenvalues of finite multiplicity. To find the eigenvalues $\lambda \in \sigma_{\text{pt}}$ we employ the ansatz

$$v(x, y, t) = v_+(x, y)e^{\lambda t} + \bar{v}_-(x, y)e^{\bar{\lambda}t},$$

which yields a solution to equation (26) provided the eigenvalue λ and the components $(v_+, v_-)^T$ of the eigenmode satisfy

$$\lambda \begin{pmatrix} v_+ \\ v_- \end{pmatrix} = \begin{pmatrix} -\eta_0 v_+ + \frac{1}{2}\mathcal{G}v_+ - \frac{1}{2}a^2\mathcal{G}v_- \\ -\eta_0 v_- + \frac{1}{2}\mathcal{G}v_- - \frac{1}{2}\bar{a}^2\mathcal{G}v_+ \end{pmatrix},$$

or equivalently

$$\begin{pmatrix} v_+ \\ v_- \end{pmatrix} = \frac{1}{2}(\lambda + \eta_0)^{-1} \begin{pmatrix} \mathcal{G}v_+ - a^2\mathcal{G}v_- \\ \mathcal{G}v_- - \bar{a}^2\mathcal{G}v_+ \end{pmatrix}. \quad (28)$$

Applying the integral operator \mathcal{G} to both sides of equation (28), we obtain the nonlocal eigenvalue problem

$$\begin{pmatrix} V_+ \\ V_- \end{pmatrix} = \frac{1}{2} \begin{pmatrix} \mathcal{G}[(\lambda + \eta_0)^{-1}(V_+ - a^2V_-)] \\ \mathcal{G}[(\lambda + \eta_0)^{-1}(V_- - \bar{a}^2V_+)] \end{pmatrix} \quad (29)$$

for the components

$$V_+(x, y) = (\mathcal{G}v_+)(x, y), \quad V_-(x, y) = (\mathcal{G}v_-)(x, y)$$

of the eigenmode of the local mean field $V \equiv \mathcal{G}v$.

Recall that for the coupling function (10), the integral operator \mathcal{G} has a finite-dimensional range spanned by the functions $\psi_k(x, y)$, $k = 1, \dots, 9$. Therefore, every solution of equation (29) can be written in the form

$$V \equiv \begin{pmatrix} V_+ \\ V_- \end{pmatrix} = \sum_{k=1}^9 \hat{V}_k \psi_k(x, y)$$

with some $\hat{V}_k \in \mathbb{C}^2$. Inserting this ansatz into equation (29) yields a system of nonlinear equations for the nine pairs of complex coefficients \hat{V}_k . Collecting these coefficients into a single vector $\hat{V} \in \mathbb{C}^{18}$, we can rewrite these equations as an equivalent matrix equation,

$$\hat{V} = \frac{1}{2} B(\lambda) \hat{V},$$

where we solve for the eigenvalue λ and the corresponding vector $\hat{V} \in \mathbb{C}^{18}$. The matrix $B(\lambda)$ has the structure

$$B(\lambda) = \begin{pmatrix} B_{11}(\lambda) & B_{12}(\lambda) & \cdots & B_{19}(\lambda) \\ B_{21}(\lambda) & B_{22}(\lambda) & \cdots & B_{29}(\lambda) \\ \vdots & \vdots & \ddots & \vdots \\ B_{91}(\lambda) & B_{92}(\lambda) & \cdots & B_{99}(\lambda) \end{pmatrix}$$

and consists of 2×2 blocks:

$$B_{mn}(\lambda) = \xi_m \begin{pmatrix} \left\langle \frac{1}{\lambda + \eta_0} \psi_m, \psi_n \right\rangle & - \left\langle \frac{H_\gamma(w)^2}{\lambda + \eta_0} \psi_m, \psi_n \right\rangle \\ - \left\langle \frac{H_\gamma(w)^2}{\lambda + \eta_0} \psi_m, \psi_n \right\rangle & \left\langle \frac{1}{\lambda + \eta_0} \psi_m, \psi_n \right\rangle \end{pmatrix},$$

where the ξ_m are defined by (20) and we have replaced $a(x, y)$ by expression (18). Thus the matrix $B(\lambda)$ is completely determined by the solution $w(x, y)$ of the self-consistency equation (19).

The eigenvalues λ can be found as solutions of the characteristic equation

$$\det \left[I_{18} - \frac{1}{2} B(\lambda) \right] = 0, \quad (30)$$

where I_n denotes the $n \times n$ identity matrix. If all solutions $\lambda \neq 0$ of equation (30) lie in the left half-plane, $\operatorname{Re} \lambda < 0$, then the corresponding equilibrium $a(x, y)$ is linearly stable. In contrast, if equation (30) has at least one solution $\lambda = \lambda_*$ such that $\operatorname{Re} \lambda_* > 0$, then the equilibrium $a(x, y)$ is unstable.

3.1.5. Stability of the completely incoherent state

The completely incoherent state corresponds to the zero solution $w(x, y) = 0$ of equation (19) and hence to the zero solution $z(x, y, t) = 0$ of equation (6). It is present for all values $A, B \in \mathbb{R}$. In this case, $\eta_0(x, y) = \gamma$ from equation (27), and therefore

$$B_{mn}(\lambda) = c_m \langle \psi_m, \psi_n \rangle (\lambda + \gamma)^{-1} I_2.$$

Owing to the mutual orthogonality of the trigonometric functions ψ_m and the relations (21), we easily see that equation (30) factorizes into three equations

$$\begin{aligned} \det \left[I_2 - \frac{1}{2} (\lambda + \gamma)^{-1} I_2 \right] &= 0, \\ \det \left[I_2 - \frac{A}{4} (\lambda + \gamma)^{-1} I_2 \right] &= 0, \end{aligned}$$

and

$$\det \left[I_2 - \frac{B}{8} (\lambda + \gamma)^{-1} I_2 \right] = 0,$$

which determine three eigenvalues

$$\lambda = -\gamma + \frac{1}{2}, \quad \lambda = -\gamma + \frac{A}{4}, \quad \lambda = -\gamma + \frac{B}{8},$$

each of double multiplicity. Consequently, the completely incoherent state $z(x, y, t) = 0$ is linearly stable if $\gamma \geq \max(1/2, A/4, B/8)$ and is unstable otherwise.

3.1.6. Stability of the partially coherent uniform state

This state corresponds to nonzero constant solutions of equations (19) and (6) of the form

$$w(x, y) = p.$$

Inserting this ansatz into equation (19) we obtain

$$p = \frac{p}{\gamma + \sqrt{\gamma^2 + p^2}}$$

yielding

$$p = \sqrt{1 - 2\gamma} \quad \text{for } \gamma < 1/2,$$

and $\eta_0(x, y) = \sqrt{\gamma^2 + p^2} = 1 - \gamma$; see equation (27). Moreover,

$$B_{mn}(\lambda) = \frac{c_m \langle \psi_m, \psi_n \rangle}{\lambda + \eta_0} \begin{pmatrix} 1 & -p^2 \\ -p^2 & 1 \end{pmatrix} = \frac{c_m \langle \psi_m, \psi_n \rangle}{\lambda + 1 - \gamma} \begin{pmatrix} 1 & 2\gamma - 1 \\ 2\gamma - 1 & 1 \end{pmatrix}.$$

Due to the mutual orthogonality of the trigonometric functions ψ_m and the relations (21), we easily see that equation (30) factorizes into nine equations ($m = 1, \dots, 9$),

$$\det \left[I_2 - \frac{c_m \langle \psi_m, \psi_m \rangle}{2(\lambda + 1 - \gamma)} \begin{pmatrix} 1 & 2\gamma - 1 \\ 2\gamma - 1 & 1 \end{pmatrix} \right] = 0,$$

and that each factor determines two eigenvalues,

$$\lambda = -1 + \gamma + \frac{c_m \langle \psi_m, \psi_m \rangle}{2} (1 \pm (2\gamma - 1)).$$

For $\gamma < 1/2$ and $c_m \geq 0$, the largest eigenvalue is

$$\lambda = -1 + \gamma + \frac{c_m \langle \psi_m, \psi_m \rangle}{2} (1 - (2\gamma - 1)) = (1 - \gamma) (c_m \langle \psi_m, \psi_m \rangle - 1).$$

Thus the linear stability condition for partially coherent uniform states reads

$$\frac{A}{2} - 1 \leq 0 \quad \text{and} \quad \frac{B}{4} - 1 \leq 0.$$

If either of the above two inequalities is violated, then the corresponding partially coherent uniform state is unstable.

3.2. Moving spiral wave chimeras for equation (6) with $\alpha \neq 0$

In this section we describe the mathematical tools used to calculate moving spiral wave solutions of equation (6) and to determine their stability. We focus on Z_2 -symmetric solutions of the form

$$z(x, y, t) = a(x, y - st) e^{i\Omega t} \tag{31}$$

with speed s , collective frequency Ω and a reflection-symmetric profile $a(x, y) = a(-x, y)$.

3.2.1. Self-consistency equation

Inserting ansatz (31) into equation (6), reordering the terms and dividing the resulting equation by $s \neq 0$, we obtain

$$\frac{\partial a}{\partial y} = \frac{\gamma + i\Omega}{s} a - \frac{1}{2s} e^{-i\alpha} \mathcal{G}a + \frac{1}{2s} e^{i\alpha} a^2 \mathcal{G}\bar{a}. \tag{32}$$

We look for 2π -periodic solutions in both x and y satisfying the inequality $|a(x, y)| \leq 1$. Therefore, if we happen to know s , Ω and $\mathcal{G}a$, then for each fixed $x \in [-\pi, \pi]$ equation (32) can be read as a periodic boundary value problem for the complex Riccati equation

$$\frac{da}{dy} = w(x, y) + \zeta a - \bar{w}(x, y) a^2, \tag{33}$$

where $a(x, \cdot)$ is an unknown function, x is a parameter,

$$w = -\frac{1}{2s} e^{-i\alpha} \mathcal{G}a$$

and

$$\zeta = \frac{\gamma + i\Omega}{s}.$$

It is known [56] that, for every $\zeta \notin i\mathbb{R}$ and every $w(x, \cdot) \in C_{\text{per}}([-\pi, \pi]; \mathbb{C})$, equation (33) has a unique 2π -periodic solution $u(y)$ depending on x as a parameter such that $|u(y)| < 1$. The corresponding solution operator is denoted by $\mathcal{U}(w, \zeta)$. Then equation (32) with the additional condition $|a(x, y)| \leq 1$ can be recast into the equivalent form

$$-2se^{i\alpha} w(x, y) = \mathcal{G}\mathcal{U}\left(w(x, y), \frac{\gamma + i\Omega}{s}\right). \quad (34)$$

We interpret equation (34) as a self-consistency equation analogous to equation (19). It is to be solved for the function $w(x, y)$ and the two scalars s and Ω . This can be done if we equip equation (34) with two pinning conditions,

$$\text{Im} \left(\int_{-\pi}^{\pi} \int_{-\pi}^{\pi} w(x, y) dx dy \right) = 0, \quad (35)$$

$$\text{Im} \left(\int_{-\pi}^{\pi} \int_{-\pi}^{\pi} w(x, y) \sin y dx dy \right) = 0, \quad (36)$$

and recall that $w(x, y)$ must share the reflection symmetry of the function $a(x, y)$.

In the case of the trigonometric coupling function (10) we can assume

$$w(x, y) = \sum_{k=1}^6 \hat{w}_k \psi_k(x, y).$$

The basis function ψ_7 , ψ_8 and ψ_9 do not appear in the sum because they do not satisfy the symmetry relation $\psi(-x, y) = \psi(x, y)$. Equation (34) is thus equivalent to the six-dimensional complex system

$$-2se^{i\alpha} \hat{w}_j = \xi_j \left\langle \mathcal{U} \left(\sum_{k=1}^6 \hat{w}_k \psi_k, \frac{\gamma + i\Omega}{s} \right), \psi_j \right\rangle$$

for six complex unknowns \hat{w}_j and two real unknowns Ω and s . The balance between the number of equations and the number of unknowns is ensured by the two pinning conditions (35) and (36), which are equivalent to the two scalar constraints

$$\text{Im } \hat{w}_1 = 0 \quad \text{and} \quad \text{Im } \hat{w}_4 = 0.$$

3.2.2. Solution operator $\mathcal{U}(w, \zeta)$

There is no explicit expression for the operator $\mathcal{U}(w, \zeta)$. But, as shown in [56], its value can be determined by solving only four initial value problems for equation (33). This possibility follows from the fact that the Poincaré map of equation (33) coincides with the classical Möbius transformation.

3.2.3. Stability analysis

The linear stability analysis of a uniformly drifting state (31) can be performed by analogy with the static case, see section 3.1. For this, we insert the ansatz

$$z(x, y, t) = (a(x, y - st) + v(x, y - st, t)) e^{i\Omega t}$$

into equation (6) and linearize the resulting equation with respect to the infinitesimal perturbation v . We thereby obtain a linear partial integro-differential equation for v ,

$$-s \frac{\partial v}{\partial \xi} + \frac{\partial v}{\partial t} = -\eta(x, \xi) v + \frac{1}{2} e^{-i\alpha} \mathcal{G}v - \frac{1}{2} e^{i\alpha} a^2(x, \xi) \mathcal{G}\bar{v}, \quad (37)$$

where $\xi \equiv y - st$ is the comoving variable and

$$\eta(x, \xi) \equiv \gamma + i\Omega + e^{i\alpha} a(x, \xi) \mathcal{G}\bar{a}.$$

The spectral problem for the eigenvalues $\lambda \in \mathbb{C}$ and eigenmodes $(v_+, v_-)^T$ can be derived from equation (37) on using the ansatz

$$v(x, \xi, t) = v_+(x, \xi) e^{\lambda t} + \bar{v}_-(x, \xi) e^{\bar{\lambda}t}.$$

After substitution into equation (37), we obtain

$$\lambda \begin{pmatrix} v_+ \\ v_- \end{pmatrix} = \begin{pmatrix} s \frac{\partial v_+}{\partial \xi} - \eta v_+ + \frac{1}{2} e^{-i\alpha} \mathcal{G}v_+ - \frac{1}{2} e^{i\alpha} a^2 \mathcal{G}v_- \\ s \frac{\partial v_-}{\partial \xi} - \bar{\eta} v_- + \frac{1}{2} e^{i\alpha} \mathcal{G}v_- - \frac{1}{2} e^{-i\alpha} \bar{a}^2 \mathcal{G}v_+ \end{pmatrix}, \quad (38)$$

where it is assumed that v_+ and v_- are 2π -periodic with respect to x and ξ .

Rigorous analysis of the properties of the spectrum defined by equation (38) can be performed using the approach proposed in [24, section 4]. On the other hand, a naive way to calculate the spectrum numerically is to discretize equation (38) on a uniform grid, approximate the derivatives by finite differences and the integrals by the trapezoid rule. This procedure leads to a matrix eigenvalue problem, which can be solved by standard numerical routines. However, this method has a significant drawback. Since the eigenmodes $v_+(x, \xi)$ and $v_-(x, \xi)$ depend on two variables, each of these functions must be approximated by arrays of minimal size $100 \times 100 = 10^4$. The corresponding eigenvalue problem thus involves a huge, dense matrix of size $10^4 \times 10^4$. As a consequence, the computation of the eigenvalues is extremely time-consuming and we do not perform it in this paper. As an alternative stability analysis scheme, we use the following phenomenological approach. Given a solution (31) of equation (6), we calculate an initial condition of the corresponding system (3) using the formula

$$\theta_{jk}(0) = \arg a(-\pi + 2\pi j/N, -\pi + 2\pi k/N).$$

We then run simulations of the system (3) for 10^4 time units. If at the end we obtain a state resembling the expected solution (31), we consider it a stable solution of equation (6). Moreover, in this case, we use the last 5000 time units to calculate the mean drift speed of the corresponding pattern, which is plotted on top of the theoretically predicted curves in figure 11(b).

4. Discussion and conclusion

We have shown that both stationary and moving partially synchronized states of two-dimensional arrays of nonlocally coupled nonidentical phase oscillators are well described in the continuum limit by a self-consistency condition originally derived by Ott and Antonsen [44]. In particular, we have shown that we can correctly compute the speed s of these structures as a function of the phase-lag parameter α , with s solving a nonlinear nonlocal eigenvalue problem. We have also shown that the same procedure can be used to determine the stability of these states and confirmed the results using direct numerical simulations of the discrete oscillator system. Our results explain the multiplicity of the different stable states in systems of this type, as well as the various bifurcations responsible for transitions between them.

Although the work was motivated by simulations performed with a top-hat coupling function, much of our progress was based on a two-parameter truncation of the Fourier expansion of this function. The advantage of using coupling functions of this type is apparent from earlier work in [31, 35, 57]. It turns out, for reasons that we do not fully understand, that the values of the parameters A and B typical of different top-hat coupling functions in fact capture the most interesting regimes in the (A, B) plane, regimes where stable stationary and moving chimeras are present (figures 7 and 10).

Our approach enabled us to understand how stable two-core spiral chimeras are generated for different values of the parameters (A, B) as well as of α , albeit for a single value of the width of the Lorentzian frequency distribution, $\gamma = 0.01$. We have seen that when $\alpha = 0$ two-core symmetric spiral chimeras, either Z_2 -symmetric or \tilde{Z}_2 -symmetric, are found on tertiary branches, following three successive symmetry-breaking bifurcations, the first of which generates a π -periodic state $|a(x, y)|$ from the partially coherent state, while the second creates a 2π -periodic state $|a(x, y)|$, after which the incoherent cores localize in the transverse direction. For stability these two-core states require nonzero values of both coupling coefficients A and B ; the optimal conditions are such that the functions $1, A \cos x, A \cos y$ and $B \cos x \cos y$ have comparable L^2 -norms, i.e. for $A \approx 2$ and $B \approx 4$. Four-core states are created by a similar process. These states are all static.

When $\alpha > 0$, these states begin to drift, resulting in a quasiperiodic state. Such two-frequency states are associated with the appearance of curved filaments in the incoherent cores. The number of such filaments increases with α , and the addition of each new filament is associated with a fold in the bifurcation diagram, resulting in states with a great many filaments in the core such as state (viii) of figure 12. The filaments of moving symmetric chimera states are curved in the direction opposite to the direction of motion. Moreover, they typically appear in the front part of the moving structure, in contrast to the one-dimensional traveling chimera states, where similar spatial oscillations emerge in the wake of the moving structure. However, the speed s of such states is in general a highly nonmonotonic function of α and may vanish for nonzero α . It is remarkable that results of this complexity can be accessed semi-analytically and that their stability properties can likewise be established by similar techniques. Direct numerical simulations of the discrete system have confirmed these results with exquisite accuracy (figure 11(b)).

In this paper, we focused on the properties of symmetric moving spiral wave chimeras with a trigonometric coupling function. We expect that with some modifications, the computational scheme described in section 3.2 can also be applied to study asymmetric spiral wave chimeras. Our results for the variational case $\alpha = 0$ show how such states are related to each other. Moreover, our methods readily extend to three-dimensional arrays of phase oscillators with trigonometric coupling functions [36] as well as to spatially-coupled arrays of phase oscillators with finite response times [58].

Although most of our results are for the trigonometric coupling function, the results qualitatively reproduce many of the direct numerical simulation results obtained for the top-hat coupling function. The trigonometric coupling approximation to this and related coupling functions has the advantage that both stable and unstable spiral chimera states can be readily computed. The latter are of inestimable value for establishing the sequence of bifurcations that are required to generate the observed stable states. We expect that the scenarios we have identified for the trigonometric coupling function carry over to other, more realistic coupling functions, where their presence can be established only with the greatest difficulty.

At a practical level, our findings can be used to explain the appearance of traveling spiral wave chimera-like patterns in phase oscillator models related to the dynamics of hydrodynamically coupled cilia carpets [6, 7]. On the other hand, they can potentially suggest new experimental designs for experiments on Belousov-Zhabotinsky chemical oscillators [8, 9]. In a broader context, we may expect that qualitatively similar spiral waves and corresponding bifurcation scenarios can be found in neural field models [59, 60] or models of cardiac tissue electrophysiology [61], where moving spiral waves are common. Potential systems that also support spiral wave chimeras include excitable optical systems, such as semiconductors lasers with [62, 63] or without absorber-saturable medium [64] or with two distinct time delays [65]. We mention, finally, two recent papers describing novel realizations of chimera states, an experimental system of degenerate optical parametric oscillators mimicking neuronal dynamics in biological systems [66] and a two-component Bose–Einstein condensate of ultracold atoms, a Hamiltonian system exhibiting spiral chimera states that may also be realizable in experiments [67].

Data availability statement

No new data were created or analyzed in this study.

Acknowledgment

M B G and M G C thank the ANID-Millenium Science Initiative Program-ICN17_012 and FONDECYT Project No. 1210353 for financial support. The work of E K was supported in part by the National Science Foundation under Grant DMS-1908891. The work of O.E.O. was supported by the Deutsche Forschungsgemeinschaft under Grant No. OM 99/2-2.

ORCID iDs

M G Clerc  <https://orcid.org/0000-0002-8006-0729>

O E Omel'chenko  <https://orcid.org/0000-0003-0526-1878>

References

- [1] Huygens C 1986 *Christiaan Huygens' The Pendulum Clock, or, Geometrical Demonstrations Concerning the Motion of Pendula as Applied to Clocks* (Iowa State University Press) Translated by R Blackwell
- [2] Bennett M, Schatz M F, Rockwood H and Wiesenfeld K 2002 *Proc. R. Soc. A* **458** 563–79
- [3] Sakaguchi H 2006 *Phys. Rev. E* **73** 031907
- [4] Luke T B, Barreto E and So P 2013 *Neural Comput.* **25** 3207–34

- [5] Omel'chenko O and Laing C R 2022 *Proc. R. Soc. A* **478** 20210817
- [6] Uchida N and Golestanian R 2010 *Phys. Rev. Lett.* **104** 178103
- [7] Golestanian R, Yeomans J M and Uchida N 2011 *Soft Matter* **7** 3074–82
- [8] Nkomo S, Tinsley M R and Showalter K 2013 *Phys. Rev. Lett.* **110** 244102
- [9] Totz J F, Rode J, Tinsley M R, Showalter K and Engel H 2017 *Nat. Phys.* **14** 282–5
- [10] Guo S, Dai Q, Cheng H, Li H, Xie F and Yang J 2018 *Chaos Solitons Fractals* **114** 394–9
- [11] Rode J, Totz J F, Fengler E and Engel H 2019 *Front. Appl. Math. Stat.* **5** 31
- [12] Adler R 1946 *Proc. IRE* **34** 351–7
- [13] Wang S S and Winful H G 1988 *Appl. Phys. Lett.* **52** 1774–6
- [14] Nishikawa T and Motter A E 2015 *New J. Phys.* **17** 015012
- [15] Kuramoto Y and Battogtokh D 2002 *Nonlinear Phenom. Complex Syst.* **5** 380–5
- [16] Abrams D M and Strogatz S H 2004 *Phys. Rev. Lett.* **93** 174102
- [17] Panaggio M J and Abrams D M 2015 *Nonlinearity* **28** R67–R87
- [18] Schöll E 2016 *Eur. Phys. J. Spec. Top.* **225** 891–919
- [19] Omel'chenko O E 2018 *Nonlinearity* **31** R121–64
- [20] Majhi S, Bera B K, Ghosh D and Perc M 2019 *Phys. Life Rev.* **28** 100–21
- [21] Haugland S W 2021 *J. Phys. Complex.* **2** 032001
- [22] Parastesh F, Jafari S, Azarnoush H, Shahriari S, Wang Z, Boccaletti S and Perc M 2021 *Phys. Rep.* **898** 1–114
- [23] Xie J, Knobloch E and Kao H C 2014 *Phys. Rev. E* **90** 022919
- [24] Omel'chenko O E 2020 *Nonlinearity* **33** 611–42
- [25] Kuramoto Y and Shima S-I 2003 *Prog. Theor. Phys. Suppl.* **150** 115–25
- [26] Shima S-I and Kuramoto Y 2004 *Phys. Rev. E* **69** 036213
- [27] Nicolaou Z G, Riecke H and Motter A E 2017 *Phys. Rev. Lett.* **119** 244101
- [28] Aranson I S and Kramer L 2002 *Rev. Mod. Phys.* **74** 99–143
- [29] Barkley D 1992 *Phys. Rev. Lett.* **68** 2090–3
- [30] Chaté H and Manneville P 1996 *Physica A* **224** 348–68
- [31] Omel'chenko O E, Wolfrum M and Knobloch E 2018 *SIAM J. Appl. Dyn. Syst.* **17** 97–127
- [32] Omel'chenko O E, Wolfrum M, Yanchuk S, Maistrenko Y L and Sudakov O 2012 *Phys. Rev. E* **85** 036210
- [33] Silber M and Knobloch E 1991 *Nonlinearity* **4** 1063–107
- [34] Maistrenko Y, Sudakov O, Osiv O and Maistrenko V 2015 *New J. Phys.* **17** 073037
- [35] Xie J, Knobloch E and Kao H C 2015 *Phys. Rev. E* **92** 042921
- [36] Omel'chenko O E and Knobloch E 2019 *New J. Phys.* **21** 093034
- [37] Bi H and Fukai T 2022 *Chaos* **32** 083125
- [38] Ulonska S, Omelchenko I, Zakharova A and Schöll E 2016 *Chaos* **26** 094825
- [39] Hagerstrom A M, Murphy T E, Roy R, Hövel P, Omelchenko I and Schöll E 2012 *Nature Phys.* **8** 658–61
- [40] Wickramasinghe M and Kiss I Z 2013 *PLoS One* **8** e80586
- [41] Kapitaniak T, Kuzma P, Wojewoda J, Czolczynski K and Maistrenko Y 2014 *Sci. Rep.* **4** 6379
- [42] Rosin D P, Rontani D, Haynes N D, Schöll E and Gauthier D J 2014 *Phys. Rev. E* **90** 030902(R)
- [43] Omel'chenko O E, Wolfrum M and Maistrenko Y L 2010 *Phys. Rev. E* **81** 065201(R)
- [44] Ott E and Antonsen T M 2008 *Chaos* **18** 037113
- [45] Omel'chenko O E 2013 *Nonlinearity* **26** 2469–98
- [46] Omel'chenko O E 2019 *J. Phys. A: Math. Theor.* **52** 104001
- [47] Bataille-Gonzalez M, Clerc M G and Omel'chenko O E 2021 *Phys. Rev. E* **104** L022203
- [48] Firth W J, Columbo L and Scroggins A J 2007 *Phys. Rev. Lett.* **99** 104503
- [49] Firth W J, Columbo L and Maggiolini T 2007 *Chaos* **17** 037115
- [50] Barbay S, Hachair X, Elsass T, Sagnes I and Kuszelewicz R 2008 *Phys. Rev. Lett.* **101** 253902
- [51] Thiele U, Archer A J, Robbins M J, Gomez H and Knobloch E 2013 *Phys. Rev. E* **87** 042915
- [52] Pradenas B, Araya I, Clerc M G, Falcón C, Gandhi P and Knobloch E 2017 *Phys. Rev. Fluids* **2** 064401
- [53] See supplementary material for animations of a moving spiral wave chimera and the solution snapshots along the bifurcation diagram in figure 3
- [54] Laing C R 2009 *Physica D* **238** 1569–88
- [55] Laing C R 2017 *SIAM J. Appl. Dyn. Syst.* **16** 974–1014
- [56] Omel'chenko O E 2023 *Nonlinearity* **36** 845–61
- [57] Omel'chenko O E, Wolfrum M and Laing C R 2014 *Chaos* **24** 023102
- [58] Lee W S, Restrepo J G, Ott E and Antonsen T M 2011 *Chaos* **21** 023122
- [59] Huang X, Troy W C, Yang Q, Ma H, Laing C R, Schiff S J and Wu J Y 2004 *J. Neurosci.* **24** 9897–902
- [60] Huang X, Xu W, Liang J, Takagaki K, Gao X and Wu J Y 2010 *Neuron* **68** 978–90
- [61] Clayton R H, Bernus O, Cherry E M, Dierckx H, Fenton F H, Mirabella L, Panfilov A V, Sachse F B, Seemann G and Zhang H 2011 *Prog. Biophys. Mol. Biol.* **104** 22–48
- [62] Barbay S, Kuszelewicz R and Yamamoto A M 2011 *Opt. Lett.* **36** 4476–8
- [63] Selmi F, Braive R, Beaudoin G, Sagnes I, Kuszelewicz R and Barbay S 2014 *Phys. Rev. Lett.* **112** 183902
- [64] Marino F and Balle S 2005 *Phys. Rev. Lett.* **94** 094101
- [65] Marino F and Giacomelli G 2019 *Phys. Rev. Lett.* **122** 174102
- [66] Makinwa T et al 2023 *Commun. Phys.* **6** 121
- [67] Lau H W H, Davidsen J and Simon C 2023 *Sci. Rep.* **13** 8590

Chapter 7

Conclusions

Mauris ac ipsum. Duis ultrices erat ac felis. Donec dignissim luctus orci. Fusce pede odio, feugiat sit amet, aliquam eu, viverra eleifend, ipsum. Fusce arcu massa, posuere id, nonummy eu, pulvinar ut, wisi. Sed dui. Vestibulum nunc nisl, rutrum quis, pharetra eget, congue sed, dui. Donec justo neque, euismod eget, nonummy adipiscing, iaculis eu, leo. Duis lectus. Morbi pellentesque nonummy dui.

Aenean sem dolor, fermentum nec, gravida hendrerit, mattis eget, felis. Nullam non diam vitae mi lacinia consectetur. Fusce non massa eget quam luctus posuere. Aenean vulputate velit. Quisque et dolor. Donec ipsum tortor, rutrum quis, mollis eu, mollis a, pede. Donec nulla. Duis molestie. Duis lobortis commodo purus. Pellentesque vel quam. Ut congue congue risus. Sed ligula. Aenean dictum pede vitae felis. Donec sit amet nibh. Maecenas eu orci. Quisque gravida quam sed massa.

Nunc euismod, mauris luctus adipiscing pellentesque, augue ligula pellentesque lectus, vitae posuere purus velit a pede. Phasellus leo mi, egestas imperdiet, blandit non, sollicitudin pharetra, enim. Nullam faucibus tellus non enim. Sed egestas nunc eu eros. Nunc euismod venenatis urna. Phasellus ullamcorper. Vivamus varius est ac lorem. In id pede eleifend nibh consectetur faucibus. Phasellus accumsan euismod elit. Etiam vitae elit. Integer imperdiet nibh. Morbi imperdiet orci euismod mi.

Donec tincidunt tempor metus. Aenean egestas cursus nulla. Fusce ac metus at enim viverra lacinia. Vestibulum in magna non eros varius suscipit. Nullam cursus nibh. Mauris neque. In nunc quam, convallis vitae, posuere in, consequat sed, wisi. Phasellus bibendum consectetur massa. Curabitur quis urna. Pellentesque a justo.



Figure 7.1: Logo de la Facultad

Table 7.1: Tabla 1

Campo 1	Campo 2	Num
Valor 1a	Valor 2a	3
Valor 1b	Valor 2b	3

In sit amet dui eget lacus rutrum accumsan. Phasellus ac metus sed massa varius auctor. Curabitur velit elit, pellentesque eget, molestie nec, congue at, pede. Maecenas quis tellus non lorem vulputate ornare. Vestibulum ante ipsum primis in faucibus orci luctus et ultrices posuere cubilia Curae; Etiam magna arcu, vulputate egestas, aliquet ut, facilisis ut, nisl. Donec vulputate wisi ac dolor. Aliquam feugiat nibh id tellus. Morbi eget massa sit amet purus accumsan dictum. Aenean a lorem. Fusce semper porta sapien.

Curabitur sit amet libero eget enim eleifend lacinia. Vivamus sagittis volutpat dui. Suspendisse potenti. Morbi a nibh eu augue fermentum posuere. Curabitur elit augue, porta quis, congue aliquam, rutrum non, massa. Integer mattis mollis ipsum. Sed tellus enim, mattis id, feugiat sed, eleifend in, elit. Phasellus non purus sed elit viverra rhoncus. Vestibulum id tellus vel sem imperdiet congue. Aenean in arcu. Nullam urna justo, imperdiet eget, volutpat vitae, semper eu, quam. Sed turpis dui, porttitor ut, egestas ac, condimentum non, wisi. Fusce iaculis turpis eget dui. Quisque pulvinar est pellentesque leo. Ut nulla elit, mattis vel, scelerisque vel, blandit ut, justo. Nulla feugiat risus in erat.

Bibliography

- [1] Eusebius J Doedel. Auto: A program for the automatic bifurcation analysis of autonomous systems. *Congr. Numer.*, 30(265-284):25–93, 1981.
- [2] Eusebius J Doedel. Lecture notes on numerical analysis of nonlinear equations. *Numerical Continuation Methods for Dynamical Systems: Path following and boundary value problems*, pages 1–49, 2007.
- [3] H.B. Keller. *Numerical Methods for Two-point Boundary-value Problems*. Blaisdell book in numerical analysis and computer science. Blaisdell, 1968.
- [4] Herbert B Keller. Numerical solution of bifurcation and nonlinear eigenvalue problem. *Application of bifurcation theory*, 1977.
- [5] Luigi A Lugiato and René Lefever. Spatial dissipative structures in passive optical systems. *Physical review letters*, 58(21):2209, 1987.
- [6] Hannes Uecker. Hopf bifurcation and time periodic orbits with pde2path – algorithms and applications. *Communications in Computational Physics*, 25, 08 2017.